Progress in Particle and Nuclear Physics 69 (2013) 131–181

Contents lists available at SciVerse ScienceDirect

Progress in Particle and Nuclear Physics

journal homepage: www.elsevier.com/locate/ppnp

Review

Ab initio no core shell model

Bruce R. Barrett [a], Petr Navrátil [b], James P. Vary [c,*]

[a] *Department of Physics, University of Arizona, Tucson, AZ 85721, USA*
[b] *Theory Group, TRIUMF, Vancouver, BC V6T 2A3, Canada*
[c] *Department of Physics and Astronomy, Iowa State University, Ames, IA 50011, USA*

ARTICLE INFO

Keywords:
Nuclei
Potentials
Theory
Predictions
Structure
Reactions

ABSTRACT

Motivated by limitations of the Bloch–Horowitz–Brandow perturbative approach to nuclear structure we have developed the non-perturbative *ab initio* no core shell model (NCSM) capable of solving the properties of nuclei exactly for arbitrary nucleon–nucleon (*NN*) and *NN* + three-nucleon (*NNN*) interactions with exact preservation of all symmetries. We present the complete *ab initio* NCSM formalism and review highlights obtained with it since its inception. These highlights include the first *ab initio* nuclear-structure calculations utilizing chiral *NNN* interactions, which predict the correct low-lying spectrum for ^{10}B and explain the anomalous long ^{14}C β-decay lifetime. We also obtain the small quadrupole moment of ^{6}Li. In addition to explaining long-standing nuclear structure anomalies, the *ab initio* NCSM provides a predictive framework for observables that are not yet measured or are not directly measurable. For example, reactions between short-lived systems and reaction rates near zero energy are relevant to fusion research but may not be known from experiment with sufficient precision. We, therefore, discuss, in detail, the extension of the *ab initio* NCSM to nuclear reactions and sketch a number of promising future directions for research emerging from the NCSM foundation, including a microscopic non-perturbative framework for the theory with a core. Having a parameter-free approach, we can construct systems with a core, which will provide an *ab initio* pathway to heavier nuclei.

© 2012 Elsevier B.V. All rights reserved.

Contents

* Corresponding author.
E-mail address: jvary@iastate.edu (J.P. Vary).

0146-6410/$ – see front matter © 2012 Elsevier B.V. All rights reserved.
doi:10.1016/j.ppnp.2012.10.003

1. Introduction

A long-standing goal of nuclear theory is to determine the properties of atomic nuclei based on the fundamental interactions among the protons and neutrons (*i.e.,* nucleons). By adopting nucleon–nucleon (*NN*), three-nucleon (*NNN*) and higher-nucleon interactions determined from either meson-exchange theory or QCD, with couplings fixed by few-body systems, we preserve the predictive power of nuclear theory. This foundation enables tests of nature's fundamental symmetries and offers new vistas for the full range of complex nuclear phenomena.

Basic questions that drive our quest for a microscopic predictive theory of nuclear phenomena include:

1. What controls nuclear saturation?
2. How do the nuclear shell and collective models emerge from the underlying theory?
3. What are the properties of nuclei with extreme neutron/proton ratios?
4. Can we predict useful cross sections that cannot be measured?
5. Can nuclei provide precision tests of the fundamental laws of nature?
6. Under what conditions do we need QCD to describe nuclear structure and reactions?

among others.

Along with other *ab initio* nuclear-theory efforts, *e.g.,* the Green's Function Monte Carlo (GFMC) approach [1–4], the Coupled-Cluster (CC) method [5,6], a lattice-simulation approach with nucleons, using effective field theory [7], *etc.,* we have pursued these questions [8,9] with meson-theoretical *NN* interactions, such as CD-Bonn [10,11] and Argonne V18 [12], that were tuned to provide high-quality descriptions of the *NN* scattering phase shifts and deuteron properties. We then added meson-theoretic *NNN* interactions, such as the Tucson–Melbourne [13,14] or Urbana IX [15] interactions.

More recently, we have adopted realistic *NN* and *NNN* interactions with ties to QCD. Chiral perturbation theory within effective field theory (χEFT) [16–18] provides us with a promising bridge between QCD and hadronic systems [19]. In this approach one works consistently with systems of increasing nucleon number [20–24] and makes use of the explicit and spontaneous breaking of chiral symmetry to expand the strong interaction in terms of a dimensionless constant, the ratio of a generic small momentum divided by the chiral symmetry breaking scale taken to be about 1 GeV/c. The resulting *NN* and *NNN* interactions, characterized by the order of the expansion retained (*e.g.*, "next-to-next-to leading order" is NNLO) [25–28], provide a high-quality fit to the NN data and the A = 3 ground-state (g.s.) properties. On the other hand, there are still outstanding questions regarding the power counting, renormalization group invariance and higher-body forces to be worked out.

Although the derivations of *NN*, *NNN*, *etc.*, interactions within meson-exchange and χEFT are well-established, they are not subjects of this review. Our focus is solution of the non-relativistic quantum many-body Hamiltonian that includes these interactions using our no core shell model (NCSM) formalism. In the next section we will briefly outline the NCSM formalism [8,9,29] and then present applications, results and extensions in later sections.

2. Historical development of the NCSM

From the very beginning of the single-particle shell-model approach to explain the structure of atomic nuclei [30–32], it has been necessary to use effective *NN* interactions among the nucleons in a truncated model space in order to simulate various experimental phenomena. At first these effective *NN* interactions were purely empirical, either in terms of parameterized *NN* potentials, *e.g.*, [33,34] or sets of *NN* matrix elements for a given model space, which were determined by fitting to a subset of the experimental data in that space [35,36]. In the following years, progress was made toward determining these effective *NN* interactions microscopically from models for the free *NN* interactions [37].

The most promising of the microscopic approaches to effective *NN* interactions was the Kuo–Brown method [38,39] based on the Bloch–Horowitz–Brandow (BHB) perturbation-theory (PT) approach [40,41]. From about 1965 to 1975 this approach achieved a considerable amount of success but then encountered a number of difficulties. Among others, these included problems related to:

1. the use of *NN* matrix elements of the nuclear reaction matrix (also known as the G-matrix) [42,43], which depended upon a not-well-defined *starting energy* parameter
2. spurious center-of-mass (COM) motion contributions
3. treatment of only the *NN* effective interactions and the neglect of many-body forces
4. poor convergence of the intermediate-state summations for each individual term in the PT expansion, due to the tensor component of the *NN* force (known as the Vary–Sauer–Wong (VSW) effect) [44]
5. lack of order-by-order convergence (in powers of G) of the PT series, as shown in the calculations of Barrett and Kirson [45,46].

This latter problem was generalized by Schucan and Weidenmüller [47,48], who demonstrated that the PT expansion for the effective two-body interaction will diverge due to the overlap in energy of states in the shell-model space, defined by projection operator P, with states *outside* the shell-model space, defined by the projection operator Q, where $P + Q = 1$. States in the Q space, which have energies in the same energy range as shell-model states, are referred to as *intruder states*. Intruder states are produced in nuclei by highly-collective states, whose energy decreases significantly from their unperturbed energies because of their collectivity. When intruder states are present, as they usually are in nuclear spectra, the order-by-order perturbation series will ultimately diverge, because the perturbation series tries to reproduce the energies of the lowest-lying states, some of which are *intruders* and, consequently, are outside of the P space.

After the Tucson Conference on Effective Interactions and Operators in Nuclei in June 1975 [49], it became evident that a new non-perturbative approach for calculating nuclear structure microscopically would be needed. However, progress was slow in developing new formalisms that were practical for numerical calculations until the early 1990s, when significant advances in computing power made new approaches, such as the No Core Shell Model (NCSM), possible.

The basic idea of the NCSM is simply to treat all A nucleons in a nucleus as active, *i.e.,* to write down the Schrödinger equation for A nucleons and then to solve it numerically. This approach avoids essentially all of the difficulties of the BHB PT approach. For example, it avoids problems related to excitations of nucleons from the core, such as the VSW effect [44] and other so-called *core-polarization effects* [39,46], because there is no core. Being a non-perturbative approach, there are no difficulties related to convergence of such an expansion. It may also be formulated in terms of an intrinsic Hamiltonian, so as to avoid spurious COM motion.

However, the physics issues raised by the earlier PT investigations are still with us in the form of requirements for the non-perturbative approach: (1) need for larger basis spaces and (2) need for effective many-body forces, in order to treat all of the complexity of the excited-states. Fortunately, these difficulties can be systematically addressed in the no-core framework, in which natural hierarchies emerge though a complete approach, retaining all the required symmetries.

Early approaches to solving the nuclear quantum many-body problem in a no-core basis used the coupled-cluster method [50] or approximated the matrix diagonalization with spectral moment-methods [51–53]. Both approaches produced the total g.s. energies of light nuclei, and the coupled-cluster method produced low-lying spectra of nuclei adjacent to closed shell systems. These works introduced a no-core effective Hamiltonian constructed from the relative kinetic energy operator, the Coulomb interaction and an effective *NN* interaction, *i.e.,* a G-matrix based on the Reid Soft Core *NN* interaction [54]. The results for the total binding energy of ^{16}O with spectral moments were shown [51,52] to be comparable to those of the coupled-cluster method with the same *NN* interaction [50].

These early no-core efforts with realistic *NN* interactions used a basis of HO states with a truncation in the single-particle spectrum and retained all Slater determinants that can be constructed within that truncation. The resulting many-body basis dimensions exceeded 10^{16} but the coupled-cluster and spectral moment methods were already capable of achieving useful (but approximate) results with the available computer power of that time. However, these early efforts were deficient in the treatment of spurious COM contributions that enter in the calculation of the G-matrix and in the use of a Slater determinant basis. This led to a series of efforts to remove the COM contributions from the G-matrix [55,56] and to demonstrate

the quantitative role of those COM effects on the properties of light nuclei [57]. It should be noted that the treatment of spurious COM motion effects within the coupled-cluster method has advanced greatly with recent developments [5].

Along with the long-term goal of eliminating spurious COM motion effects, our research focused on increasing the no-core basis spaces, so as to more completely address the physics of long-range behavior and collective effects. With reliance on increasing computing resources, numerous advances in achieving larger basis space dimensions and improving both the underlying *NN* interactions and the effective *NN* interactions propelled the field forward [57–60].

However, contrary to the BHB approach, the NCSM two-body effective interaction is physically equivalent to the earlier G-matrix calculated *on the energy shell*, hence, eliminating the *starting energy* parameter. One method for doing such a calculation is known as the Okubo–Lee–Suzuki transformation [61–66]. We investigated several approaches to applying this transformation. We first performed a straightforward application of the approach of Lee and Suzuki [67], and then a numerical approximation for determining the on-shell starting energy [68]. Along the way we also studied the importance of including the effect of the spectator nucleons on G-matrices used in nuclear-structure calculations [69]. Finally, in 1996, we arrived at our current approach for evaluating the effective *NN* interaction [70], namely the use of a unitarity transformation for calculating the two-body effective-interaction matrix elements in a model space of a given size. Considering only the two-body effective interactions in a given truncated model space is known as the two-body cluster approximation, because all correlations between two-nucleons are taken into account in calculating the two-body matrix elements. These are *not* clusters in the sense of so-called cluster models of the nucleus.

Calculations of light nuclei up to and including $A = 4$ with realistic *NN* interactions have a long history in nuclear physics. Direct solution of the wave equation in relative *NN* coordinates became feasible for $A = 3$ in the 1980's and for $A = 4$ in the early 1990's. Working in relative coordinates, we demonstrated that Hamiltonian diagonalization with realistic effective *NN* interactions provided a convergent approach to the microscopic structure of $A = 3$ and $A = 4$ [71–73]. This served as a valuable starting point for the formalism we named the "*ab initio* NCSM" in 2000, where we introduced all the elements essential to solving the problem exactly in a single-particle basis, while preserving all the underlying Hamiltonian symmetries [8,9]. We successfully applied this *ab initio* NCSM to evaluate the properties of ^{12}C with the CD-Bonn *NN* interaction [10] and the Argonne V8' *NN* interaction [74–76].

Ref. [9] contains the complete NCSM formalism for the two-body cluster approximation, as it is currently used. The first inclusion of *real NNN* interactions in the NCSM was carried out in 2002 [77]. The inclusion of *NNN* interactions is now common in *ab initio* nuclear-structure calculations.

After formulating the NCSM for calculating binding energies and excitation spectra, we then investigated the determination of other physical observables for nuclei, such as, the electric quadrupole moment, the magnetic dipole moment, transition strengths, *etc.*, within the NCSM formalism [78–81]. This work conclusively demonstrated the need to renormalize all operators relevant for describing a physical system in a truncated model space, and *not* just the Hamiltonian (or the interaction among the particles) [78,80]. It was also shown for the first time that how a physical operator renormalizes under truncation is strongly dependent upon its range [81]. In particular, short-range operators renormalize strongly, while long-range operators renormalize weakly, within the OLS scheme. It is obvious why this must be true, namely, the longer the range of an operator, the more particles with which it can interact. For example, operators, which depend upon the radius, such as, the mean-squared radius and the quadrupole moment, will be sensitive to long-range features of the nuclear wave function. Evaluating effective operators associated with finite basis expansions of the wave function will necessarily involve assessing the relative contributions of higher clusters (2-body, 3-body, *etc.*) within the effective interaction expansion. To date, only the first couple of terms of these expansions have been examined. Hopefully, the longer-range contributions of the higher-body clusters fall off in such a fashion, so as to leave these leading terms as a good approximation to the final result. Further work in this direction will be helpful and the interested reader should consult the review article by Stetcu and Rotureau in this same issue [82].

There were a number of key developments that merit inclusion here, since they demonstrated potential additional avenues for improving the no-core approach. In addition, several of these lines of investigation represent even today possible future paths for expanded applications, such as inclusion of baryon excitations explicitly in the many-body formalism.

There has been a long-standing interest in the question of whether it is necessary to include baryon excited states (baryon resonances) along with the neutron and proton, in order to achieve a successful non-relativistic description of the low-energy properties of nuclei. Most investigations centered on the inclusion of the $\Delta_{3,3}$ resonance as the leading candidate for the important channel to add. Such a "coupled-channels" approach involves a greatly expanded basis space as well as sophisticated coupled *NN*, $N - \Delta$ and $\Delta - \Delta$ interactions fit to elastic and inelastic 2-body scattering data. Refs. [83–90] examined this question in a series of coupled-channels no-core mean-field efforts that included external constraints to compress the nucleus. Without external "pressure" the Δ excitation was found to be minimally excited in these investigations, except for heavier nuclei. However, under sufficient pressure, as may be expected, all nuclei examined appear to begin to populate the Δ excited states of the nucleon. This has consequences for pion production in medium energy heavy-ion collisions and for the nuclear equation of state at moderate to high density. It will be interesting to re-examine the no-core coupled-channels approach to low-energy properties of nuclei, when coupled chiral *NN*, $N - \Delta$ and $\Delta - \Delta$ interactions become available.

Properties of finite nuclei within thermal mean-field approaches have provided valuable information related to the nuclear equation of state at finite temperatures and to statistical properties of medium-energy heavy-ion collisions. No-core

methods with realistic effective *NN* interactions have provided insights into, for example, specific heats and temperature-dependent compressibility [91–94]. In a similar vein to the previous discussion of baryon excitations, it will be important to re-evaluate these thermal properties with the more realistic chiral *NN* + *NNN* interactions now available.

There had been a long-standing concern over the neglect of effective many-body forces even within the BHB approach using perturbation theory. In valence-core applications, effective *NNN* interactions arise at the same order as core-polarization corrections to effective *NN* interactions but were typically omitted. One suspected that the choice of single-particle basis could play a significant role in governing the relative contributions of higher-body effective interactions. Indeed, this intuition was conclusively supported in a demonstration problem in Ref. [95], which presented results including effective 4-body forces for the first time.

As mentioned above, early NCSM investigations centered around finding the correct form of the effective operators to use in the no-core model space and the appropriate set of basis configurations to use for performing the NCSM calculations. Ref. [55] reports on the importance of using the relative kinetic-energy operator, while Refs. [96,97] investigate the significance of using a self-consistent set of basis configurations, such as a Hartree–Fock basis, instead of a simple single-particle HO basis.

Additional tests were carried out to determine how large the NCSM basis should be, especially whether the many-body model space should be larger than the two-body model space, as reported in Ref. [98] (see also Ref. [69]). These investigations consistently found improved convergence, when the many-body model space is larger than the two-body model space.

After the encouraging developments achieved with these early NCSM calculations, new studies were carried out using results of these early NCSM calculations as a "theoretical experiment" against which the results of other many-body approaches could be tested. In particular, in Refs. [99,100], the NCSM results were compared with the BHB PT results, so as to determine at what order PT was breaking down or becoming a reasonable approximation to the "exact" results.

The *ab initio* NCSM formalism will be presented in the following section. Later sections will highlight the major results obtained with the NCSM and its later application to nuclear reactions in the form of the NCSM/RGM method. As we conclude this section, it is worth noting that in the last several years the progress of the NCSM has been rapid, and we foresee the applications to reactions and to nuclear structure with a core as part of the promising frontiers, which lie ahead.

3. *Ab initio* NCSM formalism

In the *ab initio* no core shell model [8,9], we consider a system of *A* point-like non-relativistic nucleons that interact by realistic two- or two- plus three-nucleon interactions. By the term "realistic two-nucleon interactions", we mean *NN* potentials that fit nucleon–nucleon phase shifts with high precision up to a certain energy, typically up to 350 MeV. A realistic *NNN* interaction includes terms related to two-pion exchanges with an intermediate Delta excitation. In the NCSM, all the nucleons are considered active; there is no inert core like in standard shell model calculations. Hence, the "no core" in the name of the approach.

There are two other major features in addition to the employment of realistic *NN* or *NN* + *NNN* interactions. The first one is the use of the harmonic-oscillator (HO) basis, truncated by a chosen maximal total HO energy of the *A*-nucleon system. The reason behind the choice of the HO basis is the fact that this is the only basis that allows for the use of single-nucleon coordinates and, consequently, the second-quantization representation, without violating the translational invariance of the system. The powerful techniques based on the second quantization and developed for standard shell-model calculations can then be utilized. Therefore, the "shell model" in the name of the approach. As a downside, one has to face the consequences of the incorrect asymptotic behavior of the HO basis.

The second feature comes as a result of the basis truncation. Standard, accurate *NN* potentials, such as the Argonne V18 (AV18) [12], CD-Bonn 2000 [11], INOY (inside non-local, outside Yukawa) [101] and, to some extent, also the chiral N^3LO[27,28], generate strong short-range correlations that cannot be accommodated in many-nucleon HO bases accessible at present computers. In order to account for these short-range correlations and to speed up convergence with the basis enlargement, we adopt a renormalization procedure specified by a similarity transformation that softens the interactions and generates effective operators for all observables, while preserving all experimental quantities in the low-energy domain. The derived "effective" interactions still act among all *A* nucleons and preserve all the symmetries of the initial or "bare" *NN* + *NNN* interactions. There are two such renormalization procedures that we currently employ, one called the Lee–Suzuki (LS), or more accurately Okubo–Lee–Suzuki (OLS) scheme [61–66] and the other called the Similarity Renormalization Group (SRG) [102].

Recently, a new class of soft potentials has been developed, mostly by means of unitary transformations of the standard, accurate *NN* potentials mentioned above. These include the $V_{low k}$ [103,104], the SRG *NN* [102] and the UCOM [105,106] *NN* potentials. A different class of soft phenomenological *NN* potential are the JISP potentials based on inverse scattering [107–109]. These soft potentials are to some extent already renormalized for the purpose of simplifying many-body calculations. Therefore, we can perform convergent NCSM calculations with these potentials unmodified, or "bare". In fact, the chiral N^3LO *NN* potential [27,28] can also be used bare with some success. NCSM calculations with bare potentials are variational with the HO frequency and the basis truncation parameter as variational parameters. If a complete convergence is not achieved, one can employ an extrapolation procedure, typically using an exponential dependence on the basis truncation, to arrive at the exact result.

3.1. Hamiltonian

The starting Hamiltonian of the *ab initio* NCSM is

$$H_A = T_{\rm rel} + \mathcal{V} = \frac{1}{A}\sum_{i<j}\frac{(\vec{p}_i - \vec{p}_j)^2}{2m} + \sum_{i<j}^{A} V_{{\rm NN},ij} + \sum_{i<j<k}^{A} V_{{\rm NNN},ijk}, \tag{1}$$

where m is the nucleon mass, $V_{{\rm NN},ij}$ is the *NN* interaction, and $V_{{\rm NNN},ijk}$ is the three-nucleon interaction. In the NCSM, we employ a large but finite HO basis.

When soft *NN* potentials are used, it is often feasible to employ a sufficiently large basis to reach convergence with the Hamiltonian (1), as discussed above.

On the other hand, if realistic nuclear interactions that generate strong short-range correlations are used in Eq. (1), we perform similarity transformation(s) of the Hamiltonian, as will be discussed the following subsections.

We note that if the Slater determinant basis is to be used, we add the Lawson projection term [110] $\beta(H_{\rm CM} - \frac{3}{2}\hbar\Omega)$ to the Hamiltonian (1) to shift the spurious CM excitations. The center-of-mass Hamiltonian can be written as $H_{CM} = T_{\rm CM} + U_{\rm CM}$, where $U_{\rm CM} = \frac{1}{2}\,Am\Omega^2\vec{R}^2$, $\vec{R} = \frac{1}{A}\sum_{i=1}^{A}\vec{r}_i$, and Ω the HO frequency. Eigenenergies of physical states are independent of the parameter β.

3.2. Basis

In the *ab initio* NCSM, we use a HO basis that allows preservation of translational symmetry of the nuclear self-bound system, even if single-nucleon coordinates are utilized. This is possible as long as the basis is truncated by a maximal total HO energy of the A-nucleon system. A further advantage is that the HO wave functions have important transformation properties [111] that facilitate and simplify calculations. A single-nucleon HO wave function can be written as

$$\varphi_{nlm}(\vec{r}; b) = R_{nl}(r; b)Y_{lm}(\hat{r}), \tag{2}$$

with $R_{nl}(r, b)$, the radial HO wave function, and b, the HO length parameter related to the HO frequency Ω as $b = \sqrt{\frac{\hbar}{m\Omega}}$, with m the nucleon mass.

Because the *NN* and *NNN* interactions depend on relative coordinates and/or momenta, the natural coordinates in the nuclear problem are the relative, or Jacobi, coordinates. For the present purposes we consider just a single set of Jacobi coordinates (a more general discussion can be found in Ref. [73]):

$$\vec{\xi}_0 = \sqrt{\frac{1}{A}}\left[\vec{r}_1 + \vec{r}_2 + \cdots + \vec{r}_A\right], \tag{3}$$

$$\vec{\xi}_1 = \sqrt{\frac{1}{2}}\left[\vec{r}_1 - \vec{r}_2\right], \tag{4}$$

$$\vec{\xi}_2 = \sqrt{\frac{2}{3}}\left[\frac{1}{2}\left(\vec{r}_1 + \vec{r}_2\right) - \vec{r}_3\right], \tag{5}$$

$$\cdots$$

$$\vec{\xi}_{A-1} = \sqrt{\frac{A-1}{A}}\left[\frac{1}{A-1}\left(\vec{r}_1 + \vec{r}_2 + \cdots + \vec{r}_{A-1}\right) - \vec{r}_A\right]. \tag{6}$$

Here, $\vec{\xi}_0$ is proportional to the center of mass of the A-nucleon system. On the other hand, $\vec{\xi}_\rho$ is proportional to the relative position of the $(\rho+1)$-st nucleon and the center of mass of the ρ nucleons.

3.2.1. Antisymmetrization of Jacobi-coordinate HO basis

As nucleons are fermions, we need to construct an antisymmetrized basis. The way to do this, when the Jacobi-coordinate HO basis is used, is extensively discussed in Refs. [71–73]. Here we briefly illustrate how to do this for the simplest case of three nucleons.

One starts by introducing an HO basis that depends on the Jacobi coordinates $\vec{\xi}_1$ and $\vec{\xi}_2$, defined in Eqs. (5) and (6), *e.g.*,

$$|(nlsjt; \mathcal{N}\mathcal{L}\mathcal{J})JT\rangle. \tag{7}$$

Here n, l and $\mathcal{N}$, $\mathcal{L}$ are the HO quantum numbers corresponding to the harmonic oscillators associated with the coordinates (and the corresponding momenta) $\vec{\xi}_1$ and $\vec{\xi}_2$, respectively. The quantum numbers s, t, j describe the spin, isospin and angular momentum of the relative-coordinate two-nucleon channel of nucleons 1 and 2, while $\mathcal{J}$ is the angular momentum of the third nucleon relative to the center of mass of nucleons 1 and 2. The J and T are the total angular momentum and the total isospin, respectively. Note that the basis (7) is antisymmetrized with respect to the exchanges of nucleons 1 and 2, as the

two-nucleon channel quantum numbers are restricted by the condition $(-1)^{l+s+t} = -1$. It is not, however, antisymmetrized with respect to the exchanges of nucleons $1 \leftrightarrow 3$ and $2 \leftrightarrow 3$. In order to construct a completely antisymmetrized basis, one needs to obtain eigenvectors of the antisymmetrizer

$$\mathcal{X} = \frac{1}{3}(1 + \mathcal{T}^{(-)} + \mathcal{T}^{(+)}), \tag{8}$$

where $\mathcal{T}^{(+)}$ and $\mathcal{T}^{(-)}$ are the cyclic and the anti-cyclic permutation operators, respectively. The antisymmetrizer $\mathcal{X}$ is a projector satisfying $\mathcal{X}\mathcal{X} = \mathcal{X}$. When diagonalized in the basis (7), its eigenvectors span two eigenspaces. One, corresponding to the eigenvalue 1, is formed by physical, completely antisymmetrized states and the other, corresponding to the eigenvalue 0, is formed by spurious states. There are about twice as many spurious states as the physical ones [112].

Due to the antisymmetry with respect to the exchanges $1 \leftrightarrow 2$, the matrix elements in the basis (7) of the antisymmetrizer $\mathcal{X}$ can be evaluated simply as $\langle \mathcal{X} \rangle = \frac{1}{3}\langle 1 - 2P_{2,3} \rangle$, where $P_{2,3}$ is the transposition operator corresponding to the exchange of nucleons 2 and 3. Its matrix element can be evaluated in a straightforward way (see *e.g.*, Ref. [71])

$$\langle (n_1 l_1 s_1 j_1 t_1;\, \mathcal{N}_1 \mathcal{L}_1 \mathcal{J}_1) JT | P_{2,3} | (n_2 l_2 s_2 j_2 t_2;\, \mathcal{N}_2 \mathcal{L}_2 \mathcal{J}_2) JT \rangle = \delta_{N_1,N_2} \hat{t}_1 \hat{t}_2 \begin{Bmatrix} \frac{1}{2} & \frac{1}{2} & t_1 \\ \frac{1}{2} & T & t_2 \end{Bmatrix}$$

$$\times \sum_{LS} \hat{L}^2 \hat{S}^2 \hat{j}_1 \hat{j}_2 \hat{\mathcal{J}}_1 \hat{\mathcal{J}}_2 \hat{s}_1 \hat{s}_2 (-1)^L \begin{Bmatrix} l_1 & s_1 & j_1 \\ \mathcal{L}_1 & \frac{1}{2} & \mathcal{J}_1 \\ L & S & J \end{Bmatrix} \begin{Bmatrix} l_2 & s_2 & j_2 \\ \mathcal{L}_2 & \frac{1}{2} & \mathcal{J}_2 \\ L & S & J \end{Bmatrix} \begin{Bmatrix} \frac{1}{2} & \frac{1}{2} & s_1 \\ \frac{1}{2} & S & s_2 \end{Bmatrix} \langle n_1 l_1 \mathcal{N}_1 \mathcal{L}_1 L | \mathcal{N}_2 \mathcal{L}_2 n_2 l_2 L \rangle_3, \tag{9}$$

where $N_i = 2n_i + l_i + 2\mathcal{N}_i + \mathcal{L}_i$, $i = 1, 2$; $\hat{j} = \sqrt{2j+1}$; and $\langle n_1 l_1 \mathcal{N}_1 \mathcal{L}_1 L | \mathcal{N}_2 \mathcal{L}_2 n_2 l_2 L \rangle_3$ is the general HO bracket for two particles with mass ratio 3, as defined, e.g., in Ref. [113]. The expression (9) can be derived by examining the action of $P_{2,3}$ on the basis states (7). That operator changes the state $|nl(\vec{\xi}_1), \mathcal{N}\mathcal{L}(\vec{\xi}_2), L\rangle$ to $|nl(\vec{\xi}'_1), \mathcal{N}\mathcal{L}(\vec{\xi}'_2), L\rangle$, where $\vec{\xi}'_i$, $i = 1, 2$ are defined as $\vec{\xi}_i$, $i = 1, 2$ but with the single-nucleon indexes 2 and 3 exchanged. The primed Jacobi coordinates can be expressed as an orthogonal transformation of the unprimed ones, see *e.g.*, Ref. [71]. Consequently, the HO wave functions depending on the primed Jacobi coordinates can be expressed as an orthogonal transformation of the original HO wave functions. Elements of the transformation are the generalized HO brackets for two particles with the mass ratio d, with d determined from the orthogonal transformation of the coordinates, see *e.g.*, Ref. [113].

The resulting antisymmetrized states can be classified and expanded in terms of the original basis (7) as follows:

$$|NiJT\rangle = \sum \langle nlsjt;\, \mathcal{N}\mathcal{L}\mathcal{J} || NiJT \rangle | (nlsjt;\, \mathcal{N}\mathcal{L}\mathcal{J}) JT \rangle, \tag{10}$$

where $N = 2n + l + 2\mathcal{N} + \mathcal{L}$ and we have introduced an additional quantum number i that distinguishes states with the same set of quantum numbers N, J, T, *e.g.*, $i = 1, 2, \ldots, r$ with r the total number of antisymmetrized states for a given N, J, T. The symbol $\langle nlsjt;\, \mathcal{N}\mathcal{L}\mathcal{J} || NiJT \rangle$ is a coefficient of fractional parentage.

3.2.2. Slater determinant basis

A generalization to systems of more than three nucleons can be done as shown, *e.g.*, in Ref. [73]. It is obvious, however, that as we increase the number of nucleons, the antisymmetrization becomes more and more involved. Consequently, in standard shell-model calculations one utilizes antisymmetrized wave functions constructed in a straightforward way as Slater determinants of single-nucleon wave functions depending on single-nucleon coordinates $\varphi_i(\vec{r}_i)$. It follows from the transformations of HO wave functions that the use of a Slater determinant basis constructed from single-nucleon HO wave functions, such as,

$$\varphi_{nljmm_t}(\vec{r}, \sigma, \tau; b) = R_{nl}(r; b)(Y_l(\hat{r})\chi(\sigma))^{(j)}_m \chi(\tau)_{m_t}, \tag{11}$$

results in eigenstates of a translationally invariant Hamiltonian that factorize as products of a wave function depending on relative coordinates and a wave function depending on the CM coordinates. This is true as long as the basis truncation is done by a chosen maximum of the sum of all HO excitations, *i.e.*, $\sum_{i=1}^{A}(2n_i + l_i) \leq N_{totmax}$. In Eq. (11), σ and τ are spin and isospin coordinates of the nucleon, respectively. The physical eigenstates of a translationally invariant Hamiltonian can then be selected as eigenstates with the CM in the $0\hbar\Omega$ state:

$$\langle \vec{r}_1 \ldots \vec{r}_A \sigma_1 \ldots \sigma_A \tau_1 \ldots \tau_A | A\lambda JMTM_T \rangle_{\mathrm{SD}} = \langle \vec{\xi}_1 \ldots \vec{\xi}_{A-1} \sigma_1 \ldots \sigma_A \tau_1 \ldots \tau_A | A\lambda JMTM_T \rangle \varphi_{000}(\vec{\xi}_0; b). \tag{12}$$

For a general single-nucleon wave function this factorization is not possible. The use of any other single-nucleon wave function than the HO wave function will result in the mixing of CM and internal motion.

In the *ab initio* NCSM calculations, we use both the Jacobi-coordinate HO basis and the single-nucleon Slater determinant HO basis. One can choose whichever is more convenient for the problem to be solved. One can also mix the two types of bases. In general, for systems of $A \leq 4$, the Jacobi coordinate basis is more efficient, as one can perform the antisymmetrization

easily. The CM degrees of freedom can be explicitly removed and a coupled $J^\pi T$ basis can be utilized with matrix dimensions of the order of thousands. For systems with $A > 4$, it is, in general, more efficient to use the Slater determinant HO basis. In fact, we use the so-called m-scheme basis with conserved quantum numbers $M = \sum_{i=1}^{A} m_i$, parity π and $M_T = \sum_{i=1}^{A} m_{ti}$. The antisymmetrization is trivial, but the dimensions can be huge, as the CM degrees of freedom are present, and no JT coupling is considered. The advantage is the possibility to utilize the powerful second-quantization technique, shell-model codes, transition density codes and so on.

As mentioned above, the model space truncation is always done using the condition $\sum_{i=1}^{A}(2n_i + l_i) \leq N_{totmax}$. Often, instead of N_{totmax}, we introduce the parameter $N_{\max}$ that measures the maximal allowed HO excitation energy above the unperturbed ground state. For $A = 3, 4$ systems $N_{\max} = N_{totmax}$. For the p-shell nuclei they differ, *e.g.*, for ^{6}Li, $N_{\max} = N_{totmax} - 2$, for ^{12}C, $N_{\max} = N_{totmax} - 8$, *etc.*

3.3. Effective interaction

In the *ab initio* NCSM calculations we use a truncated HO basis, as discussed in previous sections. The inter-nucleon interactions act, however, in the full space. As long as one uses soft potentials, such as the $V_{low k}$, SRG *NN*, UCOM or JISP, convergent NCSM results can be obtained. Such NCSM calculations are variational with the HO frequency and the basis truncation parameter $N_{\max}$, acting as variational parameters.

However, the situation is different when standard *NN* potentials that generate strong short-range correlations, such as AV18, CD-Bonn 2000, and INOY, are used, or when a not-large-enough $N_{\max}$ truncation can be reached with the chiral N^{3}LO *NN* potential (in particular, when it is used in combination with the chiral *NNN* interaction). To facilitate the convergence of the calculations, we adopt a renormalization procedure specified by a similarity transformation that softens the interactions and generates effective operators for all observables, while preserving all experimental quantities in the low-energy domain. The derived "effective" interactions still act among all A nucleons and preserve all the symmetries of the initial or "bare" *NN*+*NNN* interactions. There are two such renormalization procedures that we currently employ, one called the Lee–Suzuki (LS) or Okubo–Lee–Suzuki (OLS) scheme [61,62,66] and the other called the Similarity Renormalization Group (SRG) [102].

3.3.1. Okubo–Lee–Suzuki (OLS) similarity transformation method

Let us consider an *arbitrary* Hamiltonian H with the eigensystem E_k, $|k\rangle$, i.e.,

$$H|k\rangle = E_k|k\rangle. \tag{13}$$

Let us further divide the full space into the model space defined by a projector P and the complementary space defined by a projector Q, $P + Q = 1$. A similarity transformation of the Hamiltonian $e^{-\omega}He^{\omega}$ can be introduced with a transformation operator ω satisfying the condition $\omega = Q\omega P$. The transformation operator is then determined from the requirement of decoupling of the Q-space and the model space as follows

$$Qe^{-\omega}He^{\omega}P = 0. \tag{14}$$

Using a Feshbach construction, one can show that the particular choice of the decoupling condition (14) ensures that the effective Hamiltonian is energy independent [114]. If we denote the model space basis states as $|\alpha_P\rangle$, and those which belong to the Q-space, as $|\alpha_Q\rangle$, then the relation $Qe^{-\omega}He^{\omega}P|k\rangle = 0$, following from Eq. (14), will be satisfied for a particular eigenvector $|k\rangle$ of the Hamiltonian (13), if its Q-space components can be expressed as a combination of its P-space components with the help of the transformation operator ω, *i.e.*,

$$\langle\alpha_Q|k\rangle = \sum_{\alpha_P}\langle\alpha_Q|\omega|\alpha_P\rangle\langle\alpha_P|k\rangle. \tag{15}$$

If the dimension of the model space is d_P, we may choose a set $\mathcal{K}$ of d_P eigenvectors, for which the relation (15) will be satisfied. Under the condition that the $d_P \times d_P$ matrix defined by the matrix elements $\langle\alpha_P|k\rangle$ for $|k\rangle \in \mathcal{K}$ is invertible, the operator ω can be determined from (15) as

$$\langle\alpha_Q|\omega|\alpha_P\rangle = \sum_{k\in\mathcal{K}}\langle\alpha_Q|k\rangle\langle\tilde{k}|\alpha_P\rangle, \tag{16}$$

where we denote by tilde the inverted matrix of $\langle\alpha_P|k\rangle$, e.g., $\sum_{\alpha_P}\langle\tilde{k}|\alpha_P\rangle\langle\alpha_P|k'\rangle = \delta_{k,k'}$, for $k, k' \in \mathcal{K}$.

The Hermitian effective Hamiltonian defined on the model space P is then given by [63,64]

$$\bar{H}_{\rm eff} = \left[P(1+\omega^\dagger\omega)P\right]^{1/2} PH(P+Q\omega P)\left[P(1+\omega^\dagger\omega)P\right]^{-1/2}. \tag{17}$$

By making use of the properties of the operator ω, the effective Hamiltonian $\bar{H}_{\rm eff}$ can be rewritten in an explicitly Hermitian form as

$$\bar{H}_{\rm eff} = \left[P(1+\omega^\dagger\omega)P\right]^{-1/2}(P+P\omega^\dagger Q)H(Q\omega P+P)\left[P(1+\omega^\dagger\omega)P\right]^{-1/2}. \tag{18}$$

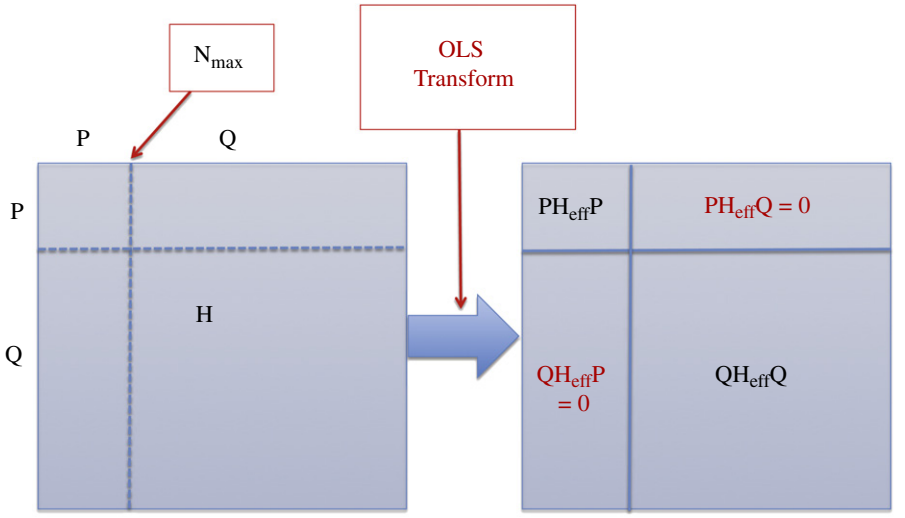

Fig. 1. Schematic illustration on how Okubo–Lee–Suzuki (OLS) similarity transformation yields an $\bar{H}_{\rm eff}$ in a finite model space P decoupled from the infinite complementary Q space.

With the help of the solution for ω (16) we obtain a simple expression for the matrix elements of the effective Hamiltonian

$$\langle\alpha_P|\bar{H}_{\rm eff}|\alpha_{P'}\rangle = \sum_{\alpha_{P''}}\sum_{\alpha_{P'''}}\sum_{kk'k''\in\mathcal{K}} \langle\alpha_P|\tilde{k}''\rangle\langle\tilde{k}''|\alpha_{P''}\rangle\langle\alpha_{P''}|\tilde{k}\rangle E_k\langle\tilde{k}|\alpha_{P'''}\rangle\langle\alpha_{P'''}|\tilde{k}'\rangle\langle\tilde{k}'|\alpha_{P'}\rangle \tag{19}$$

with all the summations over the Q-space basis states removed. The effective Hamiltonian (19) reproduces the eigenenergies E_k, $k\in\mathcal{K}$ in the model space.

There are a number of formal mathematical issues concerning effective operator approaches, in general. Some of these issues for the OLS approach have been identified and investigated in Ref. [115]. For example, one may question which subset of the eigenvalues of the full space are obtained in the OLS approach and under what conditions are the solutions well-behaved.

It has been shown [65,66] that the Hermitian effective Hamiltonian (18) can be obtained directly by a unitary transformation of the original Hamiltonian:

$$\bar{H}_{\rm eff} = Pe^{-S}He^{S}P, \tag{20}$$

with an anti-Hermitian operator $S = \operatorname{arctanh}(\omega-\omega^{\dagger})$. The transformed Hamiltonian then satisfies decoupling conditions $Qe^{-S}He^{S}P = Pe^{-S}He^{S}Q = 0$, as shown schematically in Fig. 1.

We can see from Eq. (19) that in order to construct the effective Hamiltonian we need to know a subset of exact eigenvalues and model space projections of a subset of exact eigenvectors. This may suggest that the method is rather impractical. Also, it follows from Eq. (19) that the effective Hamiltonian contains many-body terms, in fact for an A-nucleon system, all terms up to A-body will, in general, appear in the effective Hamiltonian, even if the original Hamiltonian consisted of just two-body or two- plus three-body terms.

In the *ab initio* NCSM we use the above OLS effective interaction theory as follows. First, we modify the Hamiltonian (1) by adding to it the center-of-mass (CM) HO Hamiltonian $H_{\rm CM} = T_{\rm CM} + U_{\rm CM}$, where $U_{\rm CM} = \frac{1}{2}Am\Omega^2\vec{R}^2$, $\vec{R} = \frac{1}{A}\sum_{i=1}^{A}\vec{r}_i$. The effect of the HO CM Hamiltonian will later be subtracted out in the final many-body calculation. Due to the translational invariance of the Hamiltonian (1), the HO CM Hamiltonian has in fact no effect on the intrinsic properties of the system. The modified Hamiltonian can be cast into the form

$$\begin{aligned} H_A^{\Omega} &= H_A + H_{\rm CM} = \sum_{i=1}^{A} h_i + \sum_{i<j}^{A} V_{ij}^{\Omega,A} + \sum_{i<j<k}^{A} V_{{\rm NNN},ijk} \\ &= \sum_{i=1}^{A}\left[\frac{\vec{p}_i^{\,2}}{2m} + \frac{1}{2}m\Omega^2\vec{r}_i^{\,2}\right] + \sum_{i<j}^{A}\left[V_{{\rm NN},ij} - \frac{m\Omega^2}{2A}(\vec{r}_i-\vec{r}_j)^2\right] + \sum_{i<j<k}^{A} V_{{\rm NNN},ijk}. \end{aligned} \tag{21}$$

3.3.2. Two-body OLS effective interaction

Since the two-body part dominates the A-nucleon Hamiltonian (21), it is reasonable to expect that a two-body effective interaction that takes into account full space two-nucleon correlations would be the most important part of the exact effective interaction. If the *NNN* interaction is taken into account, a three-body effective interaction that takes into account

full space three-nucleon correlations would be a good approximation to the exact A-body effective interaction. We construct the two-body or three-body effective interaction by application of the above described Okubo–Lee–Suzuki procedure to a two-nucleon or three-nucleon system. The resulting effective interaction is then exact for the two- or three-nucleon system. It is an approximation of the *exact* A-nucleon effective interaction.

Using the notation of Eq. (21), the two-nucleon effective interaction is obtained as

$$V_{2\text{eff},12} = P_2[e^{-S_{12}}(h_1 + h_2 + V_{12}^{\Omega,A})e^{S_{12}} - (h_1 + h_2)]P_2, \tag{22}$$

with $S_{12} = \text{arctanh}(\omega_{12} - \omega_{12}^{\dagger})$ and P_2 is a two-nucleon model space projector. The two-nucleon model space is defined by a truncation $N_{12\text{max}}$ corresponding to the A-nucleon N_{max}. For example, for $A = 3, 4$, $N_{12\text{max}} = N_{\text{max}}$, for p-shell nuclei with $A > 5$ $N_{12\text{max}} = N_{\text{max}} + 2$. The operator ω_{12} is obtained with the help of Eq. (16) from exact solutions of the Hamiltonian $h_1 + h_2 + V_{12}^{\Omega,A}$, which are straightforward to find. In practice, we actually do not need to calculate ω_{12}, rather we apply Eq. (19) with the two-nucleon solutions to directly calculate $P_2 e^{-S_{12}}(h_1 + h_2 + V_{12}^{\Omega,A})e^{S_{12}}P_2$. To be explicit, the two-nucleon calculation is done with

$$H_2^{\Omega} = H_{02} + V_{12}^{\Omega,A} = \frac{\vec{p}^2}{2m} + \frac{1}{2}m\Omega^2\vec{r}^2 + V_{NN}(\sqrt{2}\vec{r}) - \frac{m\Omega^2}{A}\vec{r}^2, \tag{23}$$

where $\vec{r} = \sqrt{\frac{1}{2}}(\vec{r}_1 - \vec{r}_2)$ and $\vec{p} = \sqrt{\frac{1}{2}}(\vec{p}_1 - \vec{p}_2)$ and where H_{02} differs from $h_1 + h_2$ by the omission of the center-of-mass HO term of nucleons 1 and 2. Since $V_{12}^{\Omega,A}$ acts on relative coordinate, the S_{12} is independent of the two-nucleon center of mass and the two-nucleon center-of-mass Hamiltonian cancels out in Eq. (22). We can see that for $A > 2$ the solutions of (23) are bound. The relative-coordinate two-nucleon HO states used in the calculation are characterized by quantum numbers $|nlsjt\rangle$ with the radial and orbital HO quantum numbers corresponding to coordinate $\vec{r}$ and momentum $\vec{p}$. Typically, we solve the two-nucleon Hamiltonian (23) for all two-nucleon channels up to $j = 8$. For the channels with higher j only the kinetic-energy term is used in the many-nucleon calculation. The model space P_2 is defined by the maximal number of allowed HO excitations $N_{12\text{max}}$ from the condition $2n + l \leq N_{12\text{max}}$. In order to construct the operator ω (16) we need to select the set of eigenvectors $\mathcal{K}$. We select the lowest states obtained in each channel. It turns out that these states also have the largest overlap with the P_2 model space. Their number is given by the number of basis states satisfying $2n + l \leq N_{12\text{max}}$.

The two-body effective Hamiltonian used in the A-nucleon calculation is then

$$H_{A,\text{eff}}^{\Omega} = \sum_{i=1}^{A} h_i + \sum_{i<j}^{A} V_{2\text{eff},ij}. \tag{24}$$

At this point we also subtract the H_{CM}.

3.3.3. Three-body OLS effective interaction

An improvement over the two-body effective interaction approximation is the use of the three-body effective interaction that takes into account the full space three-nucleon correlations. If the *NNN* interaction is included, the three-body effective interaction approximation is rather essential for $A > 3$ systems. First, let us consider the case with no *NNN* interaction. The three-body effective interaction can be calculated as

$$V_{3\text{eff},123}^{\text{NN}} = P_3\left[e^{-S_{123}^{\text{NN}}}(h_1 + h_2 + h_3 + V_{12}^{\Omega,A} + V_{13}^{\Omega,A} + V_{23}^{\Omega,A})e^{S_{123}^{\text{NN}}} - (h_1 + h_2 + h_3)\right]P_3. \tag{25}$$

Here, $S_{123}^{\text{NN}} = \text{arctanh}(\omega_{123} - \omega_{123}^{\dagger})$ and P_3 is a three-nucleon model space projector. The P_3 space contains all three-nucleon states up to the highest possible three-nucleon excitation, which can be found in the P space of the A-nucleon system. For example, for $A = 6$ and $N_{\text{max}} = 6$ ($6\hbar\Omega$) space we have P_3 defined by $N_{123\text{max}} = 8$. Similarly, for the p-shell nuclei with $A \geq 7$ and $N_{\text{max}} = 6$ ($6\hbar\Omega$) space we have $N_{123\text{max}} = 9$. The operator ω_{123} is obtained with the help of Eq. (16) from exact solutions of the Hamiltonian $h_1 + h_2 + h_3 + V_{12}^{\Omega,A} + V_{13}^{\Omega,A} + V_{23}^{\Omega,A}$, which are found using the antisymmetrized three-nucleon Jacobi coordinate HO basis. In practice, we again do not need to calculate ω_{123}, rather we apply Eq. (19) with the three-nucleon solutions. The three-body effective interaction is then used in A-nucleon calculations using the effective Hamiltonian

$$H_{A,\text{eff}}^{\Omega} = \sum_{i=1}^{A} h_i + \frac{1}{A-2}\sum_{i<j<k}^{A} V_{3\text{eff},ijk}^{\text{NN}}, \tag{26}$$

where the $\frac{1}{A-2}$ factor takes care of over-counting the contribution from the two-nucleon interaction.

If the *NNN* interaction is included, we need to calculate in addition to (25) the following effective interaction

$$V_{3\text{eff},123}^{\text{NN+NNN}} = P_3\left[e^{-S_{123}^{\text{NN+NNN}}}(h_1 + h_2 + h_3 + V_{12}^{\Omega,A} + V_{13}^{\Omega,A} + V_{23}^{\Omega,A} + V_{\text{NNN},123})e^{S_{123}^{\text{NN+NNN}}} - (h_1 + h_2 + h_3)\right]P_3. \tag{27}$$

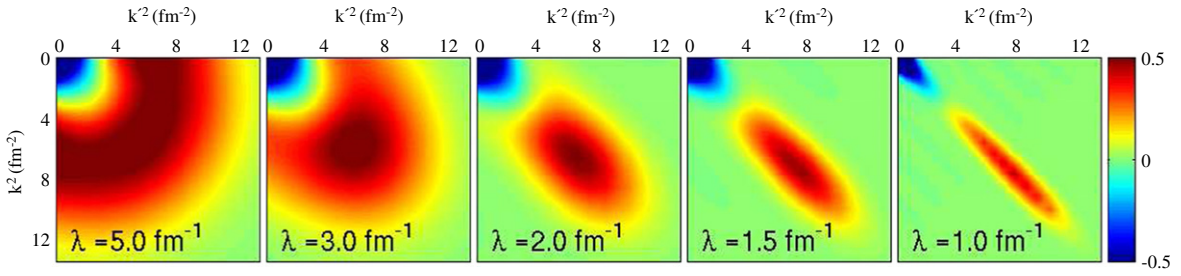

Fig. 2. Illustration of how the SRG procedure [118–120,106] weakens the strong off-diagonal couplings of the $^1S_0$ chiral N^{3}LO *NN* potential [27,28] in momentum space as the flow proceeds to smaller values of λ (left to right panels).

This three-body effective interaction is obtained using full space solutions of the Hamiltonian $h_1 + h_2 + h_3 + V_{12}^{\Omega,A} + V_{13}^{\Omega,A} + V_{23}^{\Omega,A} + V_{\mathrm{NNN},123}$. We then define the three-body effective-interaction contribution from the *NNN* interaction as

$$V_{3\mathrm{eff},123}^{\mathrm{NNN}} \equiv V_{3\mathrm{eff},123}^{\mathrm{NN+NNN}} - V_{3\mathrm{eff},123}^{\mathrm{NN}}. \tag{28}$$

The three-body effective Hamiltonian used in the A-nucleon calculation is then

$$H_{A,\mathrm{eff}}^{\Omega} = \sum_{i=1}^{A} h_i + \frac{1}{A-2}\sum_{i<j<k}^{A} V_{3\mathrm{eff},ijk}^{\mathrm{NN}} + \sum_{i<j<k}^{A} V_{3\mathrm{eff},ijk}^{\mathrm{NNN}}. \tag{29}$$

As in the case of the two-body effective Hamiltonian (24), we subtract the H_{CM}.

It should be noted that all the effective interaction calculations are performed in the Jacobi coordinate HO basis. As discussed above, the two-body effective interaction is performed in the $|nlsjt\rangle$ basis and the three-body effective interaction in the $|NiJT\rangle$ basis (10). In order to perform the A-nucleon calculation in the Slater determinant HO basis, as is typically done for $A > 4$, the effective interaction needs to be transformed to the single-nucleon HO basis. This is done with help of the HO wave function transformations. The details for the three-body case, in particular, are given in Refs. [116,117].

It should also be noted that one may think of separating the two-body and the three-body parts of the $V_{3\mathrm{eff}}^{\mathrm{NN}}$ (25). This has not been done in the NCSM calculations with the OLS effective interaction, as the current implementation (26) proved robust, and attempts of the separation were plagued by spurious model-space effects. However, such a separation is straightforward and of critical importance for successful applications of the SRG effective interactions, as discussed below.

3.4. SRG effective interaction

The SRG offers an approach to consistently evolve two-, three- (and even higher-) body forces to soften the short-range repulsion and tensor components of available initial interactions, so convergence of nuclear structure calculations is greatly accelerated. Irrespective of the chosen initial Hamiltonian, the evolution produces a variational Hamiltonian and enables smooth extrapolation of results, in contrast to Okubo–Lee–Suzuki type transformations, which produce results that are model-space dependent (in both N_{max} and A). While the SRG induces many-body forces as a product of renormalization, these terms typically come in a hierarchy of decreasing strength, if a hierarchy is initially present.

The SRG is a continuous unitary transformation of the free-space Hamiltonian H (1) ($H \equiv H_{\lambda=\infty}$),

$$H_\lambda = U_\lambda H_{\lambda=\infty} U_\lambda^\dagger, \tag{30}$$

labeled by a momentum parameter λ that runs from ∞ toward zero, which keeps track of the sequence of Hamiltonians ($s = 1/\lambda^4$ has been used elsewhere [102,118,120]). These transformations are implemented as a flow equation in λ (in units where $\hbar^2/M = 1$),

$$\frac{dH_\lambda}{d\lambda} = -\frac{4}{\lambda^5}[[T_{\mathrm{rel}}, H_\lambda], H_\lambda], \tag{31}$$

whose form guarantees that the H_λ's are unitarily equivalent [102,119,121,122].

The appearance of the nucleon relative kinetic energy T_{rel} in Eq. (31) leads to high- and low-momentum parts of H_λ being decoupled, which means softer and more convergent potentials [123]. This is evident in a partial-wave momentum basis, where matrix elements $\langle k|H_\lambda|k'\rangle$ connecting states with (kinetic) energies differing by more than λ^2 are suppressed by $e^{-(k^2-k'^2)^2/\lambda^4}$ factors and, therefore, the states decouple as λ decreases. (Decoupling also results from replacing T_{rel} in Eq. (31) with other generators [102,122,124,125].) The decoupling between the high-momentum and low-momentum parts of the *NN* interaction is illustrated in Fig. 2.

To see how the two-, three-, and higher-body potentials are identified, it is useful to decompose H_λ in second-quantized form. Schematically (suppressing indices and sums),

$$H_\lambda = \langle T\rangle a^\dagger a + \langle V_\lambda^{(2)}\rangle a^\dagger a^\dagger aa + \langle V_\lambda^{(3)}\rangle a^\dagger a^\dagger a^\dagger aaa + \cdots, \tag{32}$$

where $a^\dagger$, a are creation and destruction operators with respect to the vacuum in some (coupled) single-particle basis. This *defines* $\langle T\rangle$, $\langle V_\lambda^{(2)}\rangle$, $\langle V_\lambda^{(3)}\rangle$, ... as the one-body, two-body, three-body, ...matrix elements at each λ. Upon evaluating the commutators in Eq. (31) using H_λ from Eq. (32), we see that even if initially there are only two-body potentials, higher-body potentials are generated with each step in λ. Thus, when applied in an A-body subspace, the SRG will "induce" A-body forces. But we also see that $\langle T\rangle$ is fixed, $\langle V_\lambda^{(2)}\rangle$ is determined only in the $A = 2$ subspace with no dependence on $\langle V_\lambda^{(3)}\rangle$, $\langle V_\lambda^{(3)}\rangle$ is determined in $A = 3$ given $\langle V_\lambda^{(2)}\rangle$, and so on.

Since only the Hamiltonian enters the SRG evolution equations, there are no difficulties from having, in addition, to calculate $T_{\rm rel}$ matrices in all channels for different A-body systems. However, in a momentum basis the presence of spectator nucleons requires solving separate equations for each set of $\langle V_\lambda^{(n)}\rangle$ matrix elements. In Refs. [126,127], a diagrammatic approach is introduced to handle this decomposition. But while it is natural to solve Eq. (31), in momentum representation, it is an operator equation, so we can use any convenient basis. In the NCSM applications, we evolve in a *discrete* HO basis, where spectators are handled without a decomposition and induced many-body forces can be directly identified. Having chosen such a basis, we obtain coupled first-order differential equations for the matrix elements of the flowing Hamiltonian H_λ, where the right side of Eq. (31) is evaluated using simple matrix multiplications.

Our calculations are performed in the Jacobi coordinate HO basis described in Section 3.2.1. We start by evolving H_λ in the $A = 2$ subsystem, which completely fixes the two-body matrix elements $\langle V_\lambda^{(2)}\rangle$. Next, by evolving H_λ in the $A = 3$ subsystem we determine the combined two-plus-three-body matrix elements. We can isolate the three-body matrix elements by subtracting the evolved $\langle V_\lambda^{(2)}\rangle$ elements in the $A = 3$ basis [127]. Having obtained the separate *NN* and *NNN* matrix elements, *we can apply them unchanged to any nucleus*. We are also free to include any initial three-nucleon force in the initial Hamiltonian without changing the procedure. If applied to $A \geq 4$, four-body (and higher) forces will not be included and so the transformations will be only approximately unitary.

The evolution in the $A = 2$ basis can be performed in the momentum space directly or, equivalently, in a large HO basis ($\sim 300\hbar\Omega$). The evolution in the $A = 3$ basis for the NCSM application has up to now been performed only in the HO Jacobi basis [128–130], although the first evolution in the momentum space has now also been achieved [131]. The intermediate sums in the $A = 3$ HO Jacobi basis were typically truncated at $N_{\rm max} = 40$ for channels with lowest J [129,130].

Once the evolved interactions are determined in the Jacobi HO basis, transformations to the SD basis are performed, in particular, when nuclei with $A > 4$ are studied. The transformations of two-body interactions are standard. The correspondent three-body interaction transformations were derived and implemented in Refs. [116,117] with the latest advancement presented in Ref. [130], where a JT-coupled representation was developed with a highly efficient storage scheme, which allows us to handle *NNN* matrix-element sets up to $N_{\rm max} = 12$ model spaces for p-shell nuclei.

3.5. Convergence tests

In this subsection, we give examples of convergence of *ab initio* NCSM calculations.

First, we discuss calculations for s-shell nuclei. In Fig. 3, we show the convergence of the ^{3}H and ^{4}He g.s. energies with the size of the basis. Thin lines correspond to results obtained with the *NN* interaction only. Thick lines correspond to calculations that also include the *NNN* interaction. Here, we use the chiral effective field theory (EFT) *NN* interaction of Ref. [27,28] and the local chiral *NNN* interaction that will be discussed in detail in the next section. The solid lines correspond to ^{3}H (^{4}He) calculations with two-body (three-body) effective interaction derived from the chiral EFT potentials. The dashed lines correspond to calculations with the bare, that is the original, unrenormalized chiral EFT interactions. In ^{3}H calculations, the bare *NNN* interaction is added to either the bare *NN* (dashed thick line) or to the effective *NN* interaction (solid thick line). We observe that the convergence is faster when the effective interactions are used. However, starting at about $N_{\rm max} = 24(18)$ the convergence is reached in ^{3}H(^{4}He) calculations also with the bare *NN* interaction. It should be noted, however, that p-shell calculations with the *NNN* interactions are presently feasible in model spaces up to (depending on A) about $N_{\rm max} = 10$ or $N_{\rm max} = 12$ with the importance truncation (discussed later in this review). The use of the three-body effective interaction is then essential in the p-shell calculations with *NN* + *NNN* interactions. It should be noted that in calculations with the effective interaction, the effective Hamiltonian is different at each point, as the effective interaction depends on the size of the model space given by $N_{\rm max}$. The calculation with the bare interaction is a variational calculation converging from above with $N_{\rm max}$ and HO frequency Ω as variational parameters. The calculation with the effective interaction is not variational. The convergence can be from above, from below or oscillatory. This is because a part of the exact effective Hamiltonian is omitted. The calculation without *NNN* interaction converges to the ^{3}H ground-state energy $-7.852(5)$ MeV, well above the experimental -8.482 MeV. Once the *NNN* interaction is added, we obtain $-8.473(5)$ MeV, close to experiment. As discussed in the next section, the *NNN* parameters were tuned to reproduce the average of the ^{3}H and ^{3}He binding energies.

The rate of convergence also depends on the choice of the HO frequency. The ^{4}He calculations without *NNN* interaction were done for two different HO frequencies. It is apparent that convergence to the same result occurs in both cases.

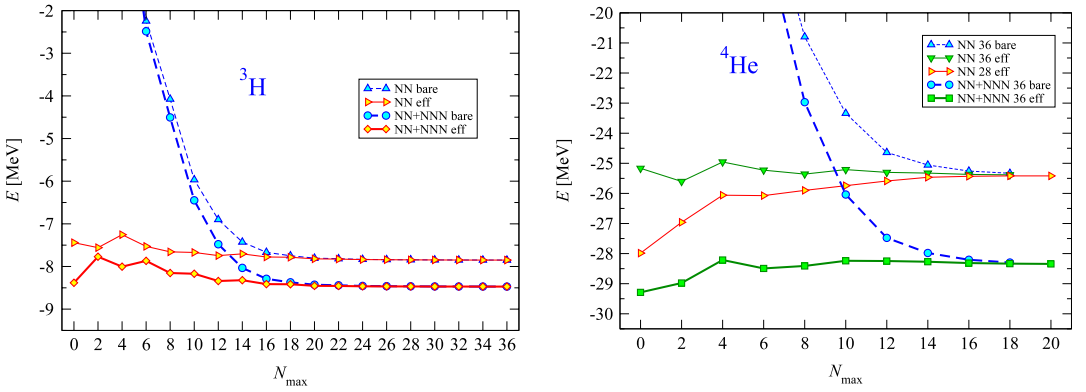

Fig. 3. ^{3}H (left) and ^{4}He (right) g.s. energy dependence on the size of the basis. The HO frequencies of $\hbar\Omega = 28$ MeV (^{3}H) and 28 or 36 MeV (^{4}He) were employed. Results with (thick lines) and without (thin lines) the *NNN* interaction are shown for the EFT interactions [27,28]. The solid lines correspond to calculations with two-body (^{3}H) or three-body (^{4}He) effective interactions, and the dashed lines to calculations with the bare interactions.

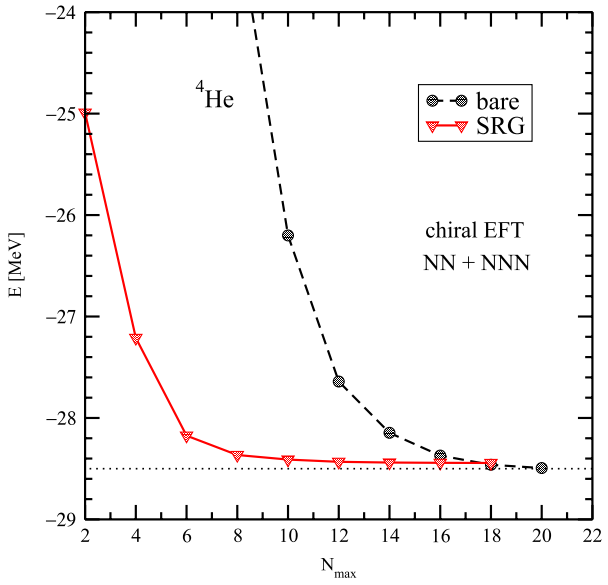

Fig. 4. Convergence of the ^{4}He g.s. energy with the size of the HO basis. Calculations with the bare (dashed line) and the SRG evolved (solid line) χEFT*NN* + *NNN* interactions are compared. The SRG evolution parameter $\lambda = 2$ fm^{-1} was used (see Fig. 2). The dotted line denotes the extrapolated g.s. energy (−28.5 MeV), which is close to the experiment (−28.3 MeV). Further details are given in Ref. [128].

We note that in the case of no *NNN* interaction, we may use just the two-body effective interaction (two-body cluster approximation), which is much simpler. The convergence is slower, however, see discussion in Ref. [132]. We also note that ^{4}He properties with the chiral EFT *NN* interaction that we employ here were calculated using the two-body cluster approximation in Ref. [133], and the present results are in agreement with results found there. Our ^{4}He ground-state energy results are −25.39(1) MeV in the *NN* case and −28.34(2) MeV in the *NN* + *NNN* case. The experimental value is −28.296 MeV. We note that the present *ab initio* NCSM ^{3}H and ^{4}He results, obtained with the chiral EFT *NN* interaction, are in a perfect agreement with results obtained using the variational calculations in the hyperspherical harmonics basis as well as with the Faddeev–Yakubovsky calculations published in Ref. [134]. A satisfying feature of the present NCSM calculation is the fact that the rate of convergence is not affected in any significant way by inclusion of the *NNN* interaction.

Fig. 4 shows such results for ^{4}He, now with SRG-evolved interactions, as a function of the *P*-space size given in terms of $N_{max}\hbar\Omega$, the maximum HO energy of configurations included above the unperturbed g.s. configuration. The figure clearly shows the accelerated rate of convergence for the *softer* SRG interactions over the *bare NN* (or *NN* + *NNN*) interaction. More details are given in Ref. [128].

As an example of convergence of *ab initio* NCSM calculations for p-shell nuclei, we present ^{6}Li results obtained using the INOY and the chiral EFT *NN* potential. The dependence of the NCSM absolute and excitation energies on the basis size

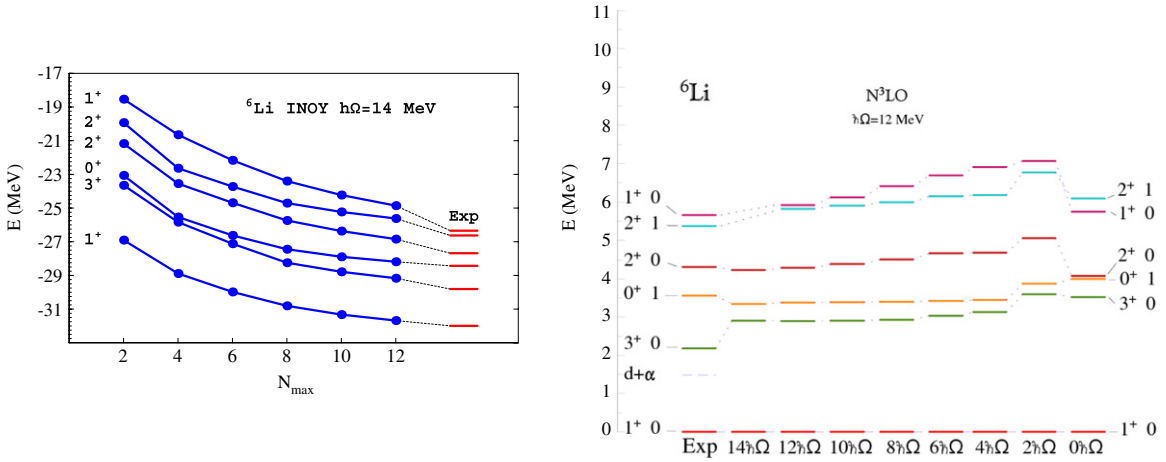

Fig. 5. Calculated absolute (left) and excitation (right) energies of ^{6}Li obtained in $0\hbar\Omega$–$12\hbar\Omega$ ($0\hbar\Omega$–$14\hbar\Omega$) basis spaces using two-body effective interactions derived from the INOY (chiral EFT) *NN* potential compared to the experiment. The HO frequencies of $\hbar\Omega = 14$ MeV (left) and 12 MeV (right) were used.

is presented in Fig. 5. The calculations were performed using the two-body effective interaction in the Slater determinant HO basis with the shell-model code Antoine [135]. Results for other HO frequencies were published in Refs. [133,136]. As discussed in Ref. [133], the convergence rate with $N_{\max}$ is different for different states. In particular, the 3^+0 state and the 0^+1 state converge faster in the higher frequency calculations ($\hbar\Omega = 12$, 13 MeV with the chiral EFT *NN* potential), while the higher-lying states converge faster in the lower frequency calculations ($\hbar\Omega = 8$, 10 MeV with the chiral EFT NN potential). The results on the right of Fig. 5 demonstrate a good convergence of the excitation energies, in particular, for the 3^+0 and 0^+1 states. An interesting result is the overestimation of the 3^+0 excitation energy compared to experiment, in particular with the chiral EFT *NN* potential. It turns out that this problem is resolved once the *NNN* interaction is included in the Hamiltonian. More discussion on eigenenergy convergence in p-shell nuclei NCSM calculations can be found, *e.g.*, in Refs. [137–139].

3.6. Computational issues for sparse Hamiltonian matrix diagonalization

Following the lines of discussion presented in Ref. [140], we outline the main factors underlying our need for substantial computational resources and collaborations with computational scientists and applied mathematicians. Basically, we are addressing a well-known "computationally hard" problem — to solve the nuclear quantum many-body problem as a large sparse matrix eigenvalue problem. Because the interactions are strong, multi-body and complicated; because there is no fixed central field; and because collective phenomena, such as clustering, appear in the low-lying spectra, we face multiple challenges very distinct from those in, for example, quantum chemistry. Our physics goals require results as close to being converged as possible, in order to minimize our extrapolation uncertainties. According to current experience, this requires the evaluation of the effective Hamiltonian in as large a basis as possible, preferably with $N_{\max} = 8 - 10$, in order to converge the low-energy nuclear properties.

The dimensions of the Hamiltonian matrix grow combinatorially with increasing $N_{\max}$ and with increasing atomic number *A*. To gain a feeling for that explosive growth, we plot in Fig. 6 the matrix dimension (D) for a wide range of Oxygen isotopes. In each case, we select the "natural parity" basis space, the parity that coincides with the lowest HO configuration for that nucleus. The heavier of these nuclei have been the subject of intense experimental investigation and it is now believed that ^{28}O is not a particle-stable nucleus, even though it is expected to have a doubly-closed shell structure, according to the phenomenological shell model. It would be very valuable to have converged *ab initio* results for ^{28}O to probe whether realistic potentials are capable of predicting its particle-unstable character.

We also include in Fig. 6 the estimated range that computer facilities of a given scale can solve with our current algorithms. As a result of these curves, we anticipate that well-converged results for the ^{12,14,16}O isotopes of Oxygen will be achieved with Petascale facilities, because their curves fall near or below the upper limit of Petascale at $N_{\max} = 10$.

Dimensions of the natural parity basis spaces for another set of nuclei ranging up to $A = 40$ are shown in Fig. 7. In addition, we include estimates of the upper limits reachable with Petascale facilities depending on the rank of the potential. It is important to note that theoretically derived four-nucleon (*NNNN*) interactions are expected to be available in the near future. Though relatively less important than *NN* and *NNN* potentials, their contributions are expected to grow dramatically with increasing *A*.

A significant measure of the computational burden is presented in Figs. 8 and 9, where we display the number of non-zero many-body matrix elements as a function of the matrix dimension (D). These results are for representative cases and show

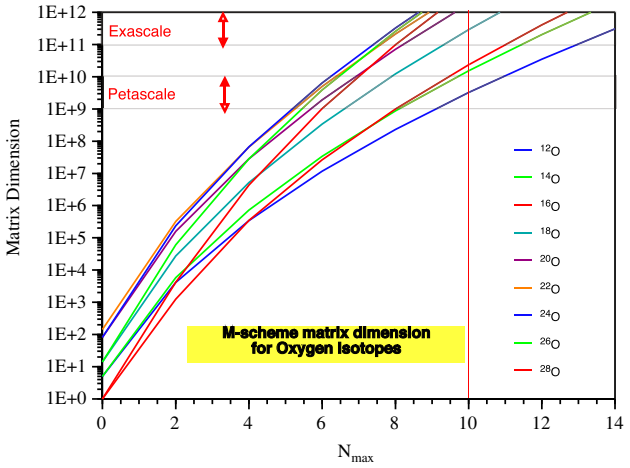

Fig. 6. Matrix dimension versus $N_{\max}$ for stable and unstable Oxygen isotopes. The vertical red line signals the boundary, beyond which we expect to achieve reasonable convergence. (For interpretation of the references to colour in this figure legend, the reader is referred to the web version of this article.)

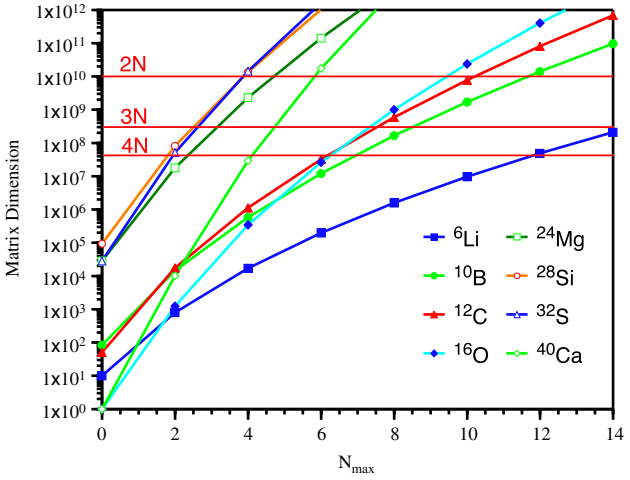

Fig. 7. Matrix dimension versus $N_{\max}$ for a sample set of stable $N = Z$ nuclei up to $A = 40$. Horizontal lines show expected limits of Petascale machines for the specified ranks of the potentials ("2*N*" = *NN*, "3*N*" = *NNN*, etc).

a useful scaling property. For Hamiltonians with *NN* potentials, we find a useful fit $F(D)$ for the non-zero matrix elements with the function

$$F(D) = D + D^{1+\frac{12}{14+\ln D}}. \tag{33}$$

The heavier systems represented tend to be slightly below the fit, while the lighter systems are slightly above the fit. The horizontal red line indicates the limit of the Jaguar facility (150,000 cores) running one of these applications assuming all matrix elements and indices are stored in core. By way of contrast, we portray the more memory-intensive situation with *NNN* potentials in Fig. 9, where we retain the fitted curve of Fig. 8 for reference. The horizontal red line indicates the same limit shown in Fig. 8.

Looking forward to the advent of exascale facilities and the development of *NNNN* potentials, we present in Table 1 the matrix dimensions and storage requirements for a set of light nuclei for potentials ranging from *NN* through *NNNN*. The storage requirements are given only for the non-zero matrix elements of the many-body matrix. These requirements dominate our memory storage requirements for the fastest calculations that store the full Hamiltonian. Less memory but more computation time is required for algorithms that regenerate the many-body Hamiltonian for each iteration.

Recent efforts have made dramatic progress in solving the nuclear sparse matrix eigenvalue problem on leadership class facilities with greater efficiency. The goal is to obtain the low-lying eigenvalues and eigenvectors using a Lanczos iteration scheme and working in the m-scheme (good total angular momentum projection) of the HO basis. We provide a brief overview of these advances in the Appendix.

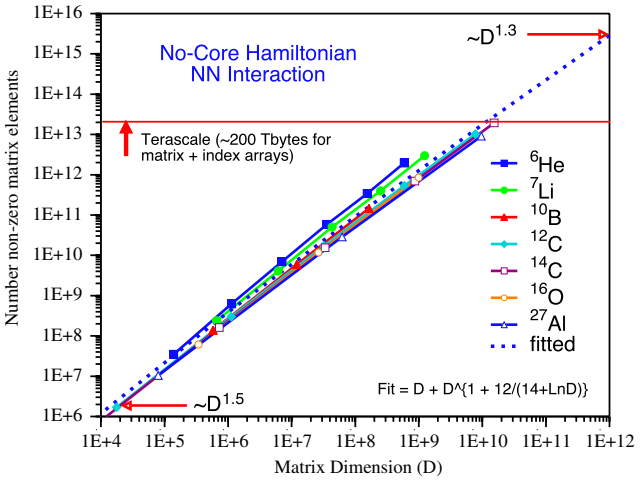

Fig. 8. Number of nonzero matrix elements versus matrix dimension (D) for an *NN* potential and for a selection of light nuclei. The dotted line depicts a function describing the calculated points.

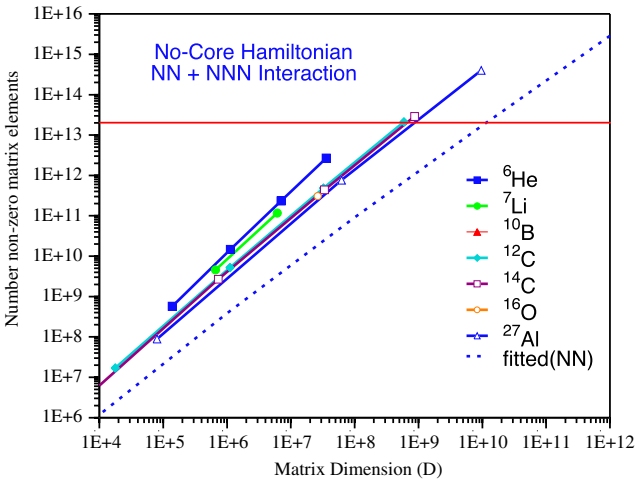

Fig. 9. Same as Fig. 8 but for an *NNN* potential. The *NN* dotted line of Fig. 8 is repeated as a reference. The *NNN* slope and magnitude are larger than the *NN* case by a factor of 10–100.

Table 1
Table of storage requirements for the nonzero matrix elements of the many-body Hamiltonian for a range of applications. The notation TB, PB and EB represent Terabytes (10^{12} bytes), Petabytes (10^{15} bytes) and Exabytes (10^{18} bytes), respectively. Roughly speaking, entries up to 400 TB imply Petascale computational facilities, while entries above 1PB imply Exascale computational facilities will likely be required.

Nucleus	N_{max}	Dimension	2-body	3-body	4-body
^{6}Li	12	$4.9 \cdot 10^{6}$	0.6 GB	33 TB	590 TB
^{12}C	8	$6.0 \cdot 10^{8}$	4 TB	180 TB	4 PB
^{12}C	10	$7.8 \cdot 10^{9}$	80 TB	5 PB	140 PB
^{16}O	8	$9.9 \cdot 10^{8}$	5 TB	300 TB	5 PB
^{16}O	10	$2.4 \cdot 10^{10}$	230 TB	12 PB	350 PB
^{8}He	12	$4.3 \cdot 10^{8}$	7 TB	300 TB	7 PB
^{11}Li	10	$9.3 \cdot 10^{8}$	11 TB	390 TB	10 PB
^{14}Be	8	$2.8 \cdot 10^{9}$	32 TB	1100 TB	28 PB
^{20}C	8	$2 \cdot 10^{11}$	2 PB	150 PB	6 EB
^{28}O	8	$1 \cdot 10^{11}$	1 PB	56 PB	2 EB

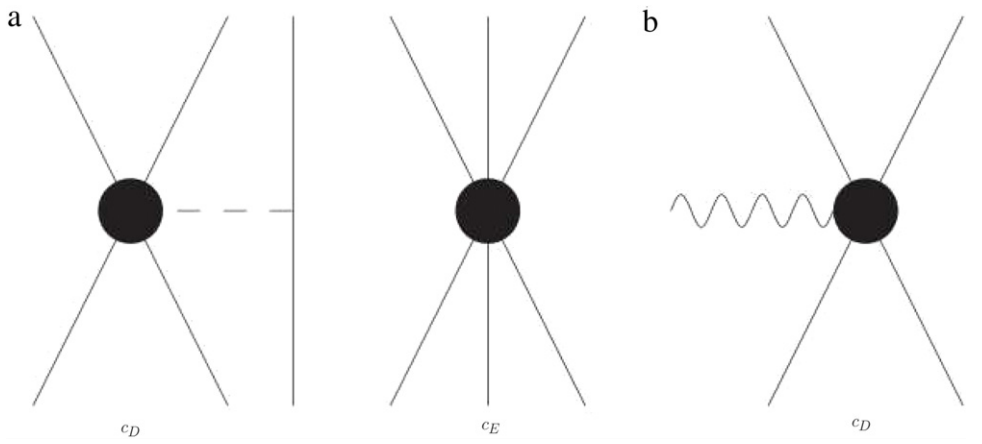

Fig. 10. Contact and one-pion exchange plus contact interaction (a), and contact MEC (b) terms of χPT.

As mentioned above, the challenge of solving for the eigenvalues and eigenvectors of a sparse matrix on parallel architectures is recognized as computationally hard and merits continued joint efforts of physicists, computational scientists and applied mathematicians. Continued developments will be needed to take advantage of major hardware advances, such as, the recent introduction of facilities built around specially developed Graphics Processing Units (GPUs). Another line of investigation is needed to fully capitalize on energy management capabilities of new architectures. Yet another area, promising potential large gains, is the advent of large-capacity solid-state memory units at the local processor level. It seems highly plausible that multiple implementations of MFDn will be needed, each of which is tailored to a specific line of architecture advances. That is one will need to continually exploit the potential gains from tradeoffs between storing/retrieving computationally-intensive intermediate results and regenerating them on-the-fly, taking into account the energy, memory and communications burdens of each.

4. NCSM applications and results

The NCSM calculations have been applied to study s-shell, p-shell and light sd-shell nuclei. In this section, rather than overview most of the published calculations, we highlight several interesting results obtained within the NCSM.

4.1. Determination of the chiral NNN low-energy constants from the triton half life and $A = 3$ binding energy

The strength of χPT is that the chiral expansion is used to derive both nuclear potentials and currents from the same Lagrangian. Therefore, the electroweak currents in nuclei (which determine reaction rates in processes involving external probes) and the strong interaction dynamics (πN scattering, the *NN* interaction, the *NNN* interaction, *etc.*,) are all based on the same theoretical grounds and rooted in the low-energy limits of QCD. In particular, χPT predicts, along with the *NN* interaction at the leading order (LO), a three-nucleon (*NNN*) interaction at the next-to-next-to-leading order or N^{2}LO [141,142], and even a four-nucleon force at the fourth order (N^{3}LO) [143]. At the same time, the LO nuclear current consists of (the standard) single-nucleon terms, while two-body currents, also known as meson-exchange currents (MEC), make their first appearance at N^{2}LO [144]. Up to N^{3}LO both the potential and the current are fully constrained by the parameters defining the *NN* interaction, with the exception of two "new" LECs, c_D and c_E. The latter, c_E, appears only in the potential as the strength of the *NNN* contact term (see Fig. 10(a)). On the other hand, c_D manifests itself both in the contact term part of the *NN*-π-*N* three-nucleon interaction of Fig. 10(a) and in the two-nucleon contact vertex with an external probe of the exchange currents (see Fig. 10(b)).

In Ref. [145] we utilized the chiral-symmetry mandated relation between the electroweak processes and the *NNN* force effects to determine the c_D and c_E LECs by calculating the $A = 3$ binding energy and the triton half life. Using the *ab initio* NCSM calculations with the chiral *NN* interaction at N^{3}LO [27,28] and the *NNN* interaction at N^{2}LO in the local form of Ref. [146], we first constrained the c_D and c_E parameters by fitting the average of the experimental ^{3}H and ^{3}He binding energy. Then we calculated the triton half life using the leading order Gamow–Teller operator and the N^{2}LO current corrections in the form of MEC and relativistic terms. In particular, the MEC have a substantial influence on the ^{3}H β-decay rate. Moreover, the strength of the MEC contact term, usually denoted by $\hat{d}_R$, is related to c_D through:

$$\hat{d}_R \equiv \frac{M_N}{\Lambda_\chi g_A} c_D + \frac{1}{3} M_N (c_3 + 2c_4) + \frac{1}{6}. \tag{34}$$

Here, M_N is the nucleon mass, and c_3 and c_4 are LECs of the dimension-two πN Lagrangian, already part of the chiral *NN* potential at NLO. Therefore, one can use ^{3}H β-decay rate as a second constraint for the determination of c_D and c_E. Results of

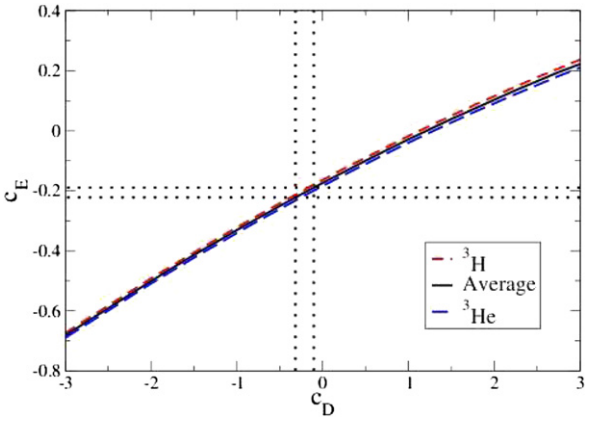

Fig. 11. $c_D - c_E$ trajectories fitted to reproduce ^{3}H and ^{3}He experimental binding energy. See Ref. [145] for further details.

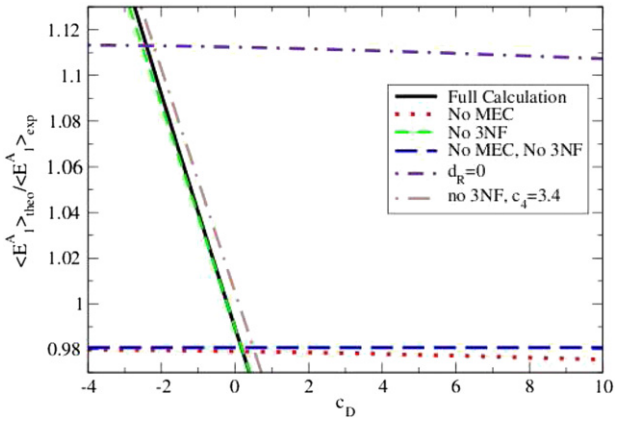

Fig. 12. The ratio of calculated and experimental ^{3}H beta decay matrix element using the *NN* potential with and without the *NNN* interaction, and the axial current with and without MEC.

Table 2
Calculated ^{3}H, ^{3}He and ^{4}He g.s. energies (in MeV) and point-proton radii (in fm), obtained using the N^{3}LO *NN* potential [27,28] with and without the local N^{2}LO *NNN* interaction [146] with $c_D = -0.2$ and $c_E = -0.205$, compared to the experiment.

	^{3}H		^{3}He		^{4}He	
	$E_{\text{g.s.}}$	$\langle r_p^2\rangle^{1/2}$	$E_{\text{g.s.}}$	$\langle r_p^2\rangle^{1/2}$	$E_{\text{g.s.}}$	$\langle r_p^2\rangle^{1/2}$
NN	−7.852(4)	1.651(5)	−7.124(4)	1.847(5)	−25.39(1)	1.515(2)
NN + *NNN*	−8.473(4)	1.605(5)	−7.727(4)	1.786(5)	−28.50(2)	1.461(2)
Expt.	−8.482	1.60	−7.718	1.77	−28.296	1.467(13) [147]

the determination are summarized in Figs. 11 and 12. We note the fundamental importance of the axial two-body currents in reaching agreement with experiment. By suppressing the MEC, in the whole investigated $c_D - c_E$ range, the calculations under-predict $\langle E_1^A\rangle|_{emp}$ matrix element by about 2%. The same, almost constant, behavior is found, when adding to the single-nucleon current only the long-range one-pion-exchange term of the MEC, which corresponds to setting $\hat{d}_R = 0$. In this case, the theoretical results over-predict $\langle E_1^A\rangle|_{emp}$ by ∼11%. Only when adding the contact part of the MEC, which is related to the short-range weak correlations of axial character, can the half-life reach its experimental value. In particular, we find that agreement within ±0.54% of the empirical value is obtained for $-0.3 \leq c_D \leq -0.1$. The corresponding c_E values lie in the range $[-0.220, -0.189]$. These results are summarized by the dotted lines in Fig. 11.

With this calibration of c_D and c_E, for this potential, in principle, any other calculation is a prediction of χPT. In Table 2 we present a collection of $A = 3$ and 4 data, obtained with and without inclusion of the *NNN* force for $c_D = -0.2$ ($c_E = -0.205$), a choice in the middle of the constrained interval. Besides triton and ^{3}He g.s. energies, which are by construction within few keV from experiment, the *NN* + *NNN* results for the ^{4}He are in good agreement with measurement.

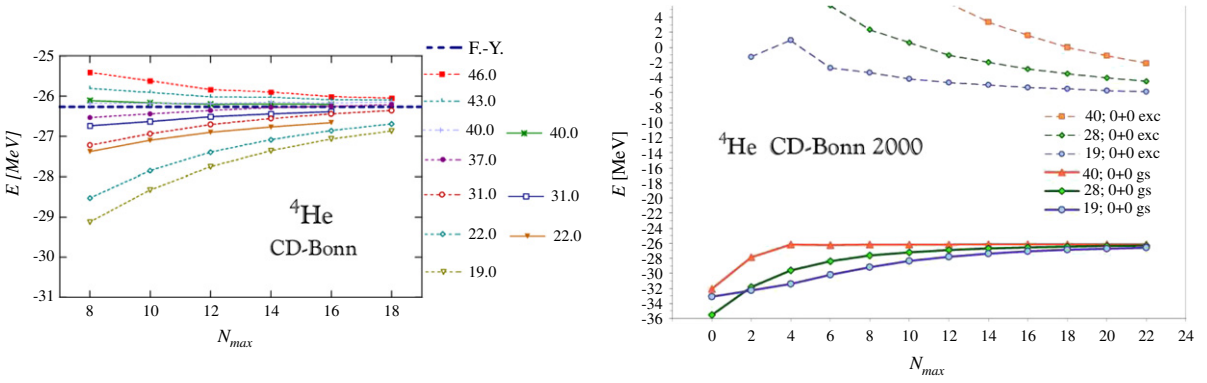

Fig. 13. Ground state (in the right panel also the first 0^+0 excited state) energy of ^{4}He calculated using the CD-Bonn (left panel) and CD-Bonn 2000 (right panel) *NN* potentials. Dependence on the NCSM model-space size $N_{\max}$ for different HO frequencies is presented. The OLS renormalization was used. Further details are in the text.

4.2. ^{4}He *with the CD-Bonn NN potential*

The CD-Bonn *NN* potential [10] provides a very accurate fit to the *NN* scattering data and the deuteron properties. In Ref. [73], we applied this potential to calculations of ground states of ^{3}H, ^{3}He and ^{4}He. We used the Jacobi-coordinate HO basis and the OLS renormalization procedure. For ^{4}He, this was the first microscopic calculation with this potential. The calculations were done up to $N_{\max} = 16$, which allowed to determined the g.s. energy as $-26.4(2)$ MeV. The experimental value is -28.296 MeV. In the left panel of Fig. 13, we present the calculations of Ref. [73] extended to $N_{\max} = 18$ and compared to the later Faddeev–Yakubovsky result of -26.26 MeV [148]. The dotted lines connect NCSM calculations with the two-body OLS effective interactions, while the full lines connect calculations with the three-body OLS effective interaction.

Later, we performed more ^{4}He calculations with the updated version of this *NN* potential, the CD-Bonn 2000 [11]. In the right panel of Fig. 13, we present a dependence of the ^{4}He ground state and the first 0^+0 excited-state energy on the model-space size up to $N_{\max} = 22$ for three different HO frequencies. The calculation was performed with the no-core version of the shell-model code Antoine [135]. The two-body OLS effective-interaction renormalization was used. We observe a fast convergence for the ground state for all three frequencies with the final result $-26.16(6)$ MeV in a good agreement with Faddeev–Yakubovsky and HH calculation [149]. The excited-state convergence is slower with a stronger frequency dependence, due to the more complex structure of this state. Still, we are able to extrapolate the excitation energy to -6.0(3) MeV. Although the CD-Bonn 2000 *NN* potential underbinds ^{4}He by about 2 MeV, the $0^+_2 0$ excitation energy is described rather well. It is interesting to point out that the convergence rate for the ground state is the fastest for the highest HO frequency, while the convergence rate for the excited state is the fastest for the lowest HO frequency, employed in our presented calculations. Clearly, the optimal frequency for a convergence is state dependent and correlated with the radius of the state, the smaller the radius the higher optimal frequency. These calculations for the ground state were discussed in Ref. [138], where the point-proton radius was determined to be 1.45(1) fm in a good agreement with experiment.

We note that the alternative SRG renormalization procedure does not work with sufficient accuracy for the CD-Bonn with the currently achievable limits on the three-nucleon model space ($N_{\max} \sim 40$, used to calculate the induced *NNN* interaction). This is seen in results presented in Ref. [129]. The CD-Bonn generates stronger short-range repulsive correlations than the chiral potentials, for which the SRG renormalization is applied successfully.

4.3. *Quadrupole moment of* ^{6}Li

The ground state of ^{6}Li has a very small quadrupole moment $Q = -0.0818(17)\, e\,\mathrm{fm}^2$ [150]. This tiny value can be compared to, *e.g.*, the quadrupole moment of ^{7}Li $Q = -4.06(8)\, e\,\mathrm{fm}^2$ [150]. It is a challenge for nuclear models to explain this small value or even its negative sign. This is exemplified in the evaluation [150] with a list of approaches that failed to reproduce this observable.

The NCSM calculations with different *NN* potentials, on the other hand, find consistently a very small value of the ^{6}Li quadrupole moment close to experiment. As an example, in Fig. 14 we present the ^{6}Li ground-state quadrupole moment calculation with the chiral N^{3}LO *NN* potential. In particular, we show the HO frequency dependence of Q for different basis sizes. With the basis size increase the frequency dependence decreases. For the smallest basis sizes, $N_{\max} = 0$ and 2, we get a large negative value with a strong frequency dependence. As the $N_{\max}$ increases, the HO dependence becomes flat and changes with the steps of $N_{\max}$ are reduced significantly. We conclude that the quadrupole moment of ^{6}Li with the N^{3}LO *NN* interaction is $-0.08(2)\, e\,\mathrm{fm}^2$ in excellent agreement with experiment. A similar result was obtained with the chiral Hamiltonian that included the *NNN* interaction. In particular, using the *NNN* LEC $c_D = -0.2$, determined from the ^{3}H lifetime, we get the ^{6}Li Q moment in a good agreement with experiment, as seen in Fig. 2 of Ref. [151].

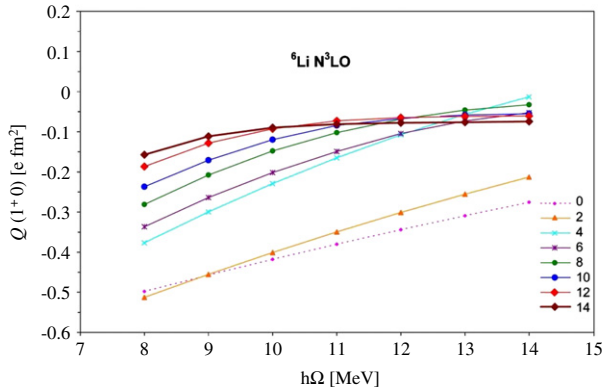

Fig. 14. Harmonic-oscillator frequency dependence of the ^{6}Li quadrupole moment, obtained in $0\hbar\Omega$–$14\hbar\Omega$ ($N_{\max} = 0 - 14$) basis spaces, using two-body effective interactions, derived from the N^{3}LO *NN* potential. For further details on the calculations, see Ref. [133].

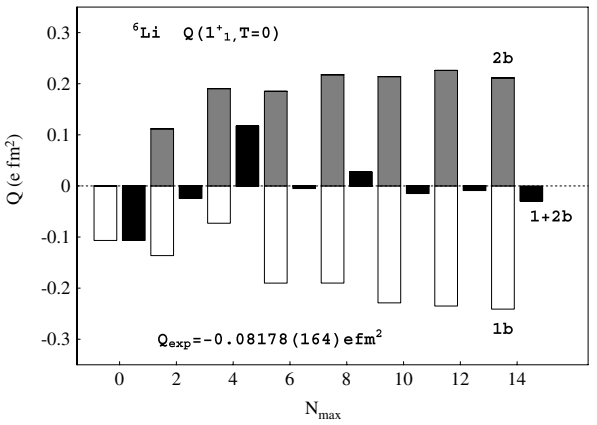

Fig. 15. The quadrupole moment (Q) of the g.s. for ^{6}Li ($J^\pi T = 1^+0$) is shown in terms of one- and two-body contributions, as a function of increasing model-space size of the NCSM calculation used to generate the valence-shell effective Hamiltonian and $E2$ operator. The one- and two-body contributions and total Q are depicted as white, gray and black histograms, respectively [152]. The experimentally measured Q is listed on the figure for comparison.

An interesting insight into the mechanisms of the ^{6}Li Q moment suppression was given in the *ab initio* SM calculations with the core [152], described in a subsequent section. It was shown that the tiny value arises due to a strong cancellation between the one- and two-body contributions to Q [152], as illustrated in Fig. 15. The two-body contribution is induced by the basis-space truncation from a multi-major-shell basis to a valence space, comprised of a single major shell (0p-shell). Any standard shell-model calculation restricted to a valence shell and a one-body $E2$ operator will inevitably generate a Q moment of the ^{6}Li g.s. that is too large, see the white histograms in Fig. 15.

4.4. NCSM applications to $A = 7$ and $A = 8$ nuclei

The $A = 7$ and $A = 8$ nuclei present a number of scientific and technical challenges. First, there is a significant amount of spectroscopic, reaction and decay data already available with the promise of more data with high precision in the near future. Second, these systems present a reasonable range of complexity from expected single-particle behavior through clustering effects. Third, the sizes of the calculations needed to approach convergence with *NN* + *NNN* interactions represent major technical challenges.

We recently solved the *ab initio* NCSM in the complete $8\hbar\Omega$ ($N_{\max} = 8$) basis for $A = 7$ and $A = 8$ nuclei with *NN* + *NNN* interactions, derived within chiral EFT [153]. We find that including the chiral EFT *NNN* interaction in the Hamiltonian improves overall agreement with experimental binding energies, excitation spectra, transitions and electromagnetic moments. We predict states that exhibit sensitivity to including the chiral EFT *NNN* interaction but are not yet known experimentally.

We show the low-lying spectra of ^{7}Li in Fig. 16 at $\hbar\Omega = 13$ MeV and at a sequence of $N_{\max}$ truncations. The HO energy is chosen, where the g.s. energy of ^{7}Li is a minimum in the $8\hbar\Omega$ basis space. Note that our *NN* + *NNN* ordering is in agreement with experiment for the 9 lowest states in ^{7}Li and the excitation spectra is rather stable with increasing $N_{\max}$. We also obtain theoretical excitation spectra showing comparable agreement with experiment for ^{7}Be.

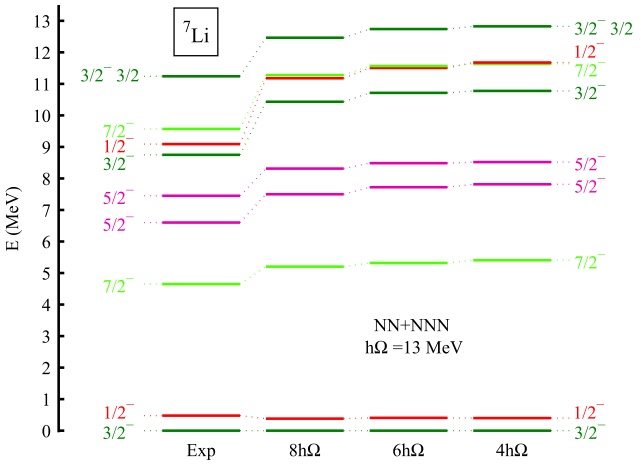

Fig. 16. (Color online) Calculated and experimental excitation energies of ^{7}Li from Ref. [153]. Dependence on the size of the basis is presented. The chiral EFT *NN* and *NNN* interaction was used and $\hbar\Omega = 13$ MeV. The isospin of the states is $T = 1/2$ unless shown otherwise.

Table 3
The NCSM results in the $8\hbar\Omega$ basis space for the g.s. energies, in MeV, of ^{8}He, ^{8}Li, ^{8}Be, ^{8}B and ^{8}C using the chiral *NN* and the chiral *NN*+*NNN* interactions. Experimental energies are from Ref [154]. The basis space dependencies, explained in the text, are in parenthesis.

	Exp	*NN*	*NN* + *NNN*
^{8}He	−31.408	−24.61	−29.23 (41)
^{8}Li	−41.277	−34.86	−39.95 (69)
^{8}Be	−56.499	−49.70	−55.33 (84)
^{8}B	−37.737	−31.38	−36.35 (67)
^{8}C	−24.782	−17.86	−22.22 (33)

Calculated g.s. energies of $A = 8$ nuclei from Ref. [153] are summarized in Table 3. We define the basis-space dependence of our total g.s. energy as the difference in total energy at $\hbar\Omega = 13$ MeV for the basis space increment from $N_{\max} = 6$ to 8. With both the *NN* interaction alone and the *NN* + *NNN* interaction, the results appear reasonably stable in going from $N_{\max} = 6$ to $N_{\max} = 8$. The role of the chiral EFT *NNN* interaction is to shift all calculated g.s. energies significantly closer to the experimental results. There appears to be a tendency to underbind these nuclei as one moves away from the minimum in the valley of stability.

In addition to g.s. energies and excitation spectra, we evaluated a set of electromagnetic moments as well as transition matrix elements in $A = 7$ and $A = 8$ nuclei and compared with experiment, where possible. In almost all cases, the inclusion of chiral *NNN* interactions improved agreement between theory and experiment over results obtained with chiral *NN* interactions alone.

It is worth pausing here to assess where we stand with the results presented in this subsection alone. The conclusions we draw here pertain equally well to results in other subsections, showing highlights of our NCSM results with chiral Hamiltonians.

Taking into account our estimates of the basis-space dependence of our g.s. energies and spectra for the $A = 7$ and $A = 8$ nuclei summarized here, we find that there are residual differences between theory and experiment that can now be attributed to the need for further improvements to our approach. Those improvements could originate from improved chiral *NNN* interactions, adding chiral *NNNN* interactions and/or including effective *NNNN* interactions. We also recall that there is imperfect knowledge of the nonperturbative coupling constants in the currently-employed chiral *NN* + *NNN* interactions that could, if exploited, remove differences between the current theoretical results and experiment.

Before progressing to heavier systems, we adopt the ^{7}Li and ^{8}Li cases for detailed comparisons among different *ab initio* methods and among different realistic Hamiltonians. We make these comparisons in Tables 4 and 5. The g.s. energies are seen to be in reasonable agreement with experiment with the exception of the CD-Bonn results. Since JISP16 and INOY have been adjusted to fit some properties of light nuclei, it is not surprising to see their results are comparable to the Chiral interaction results and the AV18/IL2 results that include an *NNN* interaction. Uncertainties in the theoretical results are quoted, where they are available from the cited literature. In some cases, there are theoretical predictions, where no experimental data is available.

Table 4
Comparison of ^{7}Li observables between experiment [155–157] and theory. The OLS results with Chiral $NN + NNN$ are calculated at $\hbar\Omega = 13$ MeV in the NCSM up through $N_{max} = 8$ [153]. The SRG results ($\alpha = 0.08$) with Chiral $NN + NNN$ for $N_{max} = 8$; 10 calculated at $\hbar\Omega = 16$MeV in the IT-NCSM are reported in Ref. [158]. Results up through $N_{max} = 14$ with JISP16 [107–109] obtained in the NCFC approach are reported in Ref. [159]. AV18/IL2 results are obtained in the GFMC approach as reported in Refs. [1–4]. The energies are in MeV; the g.s. RMS point-proton radius ($\langle r_{pp}^2\rangle^{1/2}$) is in fm; the quadrupole moments (Q) are in e fm^2; the magnetic moments (μ) are in μ_N; the reduced B(E2) transition probabilities are in e^{2}fm^4; and the reduced B(M1) transition probabilities are in μ_N^2. All listed transitions are to the ground state. The energies with JISP16 are obtained from extrapolations to the infinite basis space, and the magnetic dipole observables are nearly converged, with error estimates as discussed in Ref. [159] (two errors are quoted based on separate methods of estimating the error for excitation energies); the RMS point-proton radius and electric quadrupole observables are evaluated at $\hbar\Omega = 12.5$ MeV with JISP16. The AV18/IL2 results include meson-exchange corrections for the dipole observables (e.g. these corrections change the g.s. magnetic moment from $\approx 2.9\ \mu_N$ to $\approx 3.2\ \mu_N$); CD-Bonn ("CD-B") and INOY results are NCSM results from Refs. [136,163] calculated at $N_{max} = 12$ and $\hbar\Omega = 11$, 12 and 16 MeV respectively, with the INOY gs energy extrapolated to the infinite basis space.

^{7}Li	Expt.	Chiral $NN + NNN$ Okubo–Lee–Suzuki	Chiral $NN + NNN$ SRG(0.08) $N_{max} = 8$; 10	AV18/IL2	JISP16	INOY	CD-B
$E_b(\frac{3}{2}^-_1\ \frac{1}{2})$	39.244	38.60(44)	38.14(1) ; 38.90(2)	38.9(1)	38.57(4)	39.6(4)	35.56
$\langle r_{pp}^2\rangle^{1/2}$	2.30(5)	2.11		2.25(1)	2.2	2.05	2.22
$E_x(\frac{1}{2}^-_1\ \frac{1}{2})$	0.477	0.382(69;24)	0.332(3) ; 0.312(2)	0.2(1)	0.52(6)	0.51	0.29
$E_x(\frac{7}{2}^-_1\ \frac{1}{2})$	4.630(1)	5.20(22;12)	4.983(2) ; 4.980(9)	4.9(1)	5.25(5)	5.35	5.49
$E_x(\frac{5}{2}^-_1\ \frac{1}{2})$	6.680(50)	7.50(16;23)	7.135(9) ; 6.992(10)	6.6(1)	7.1(2)	7.66	7.00
$E_x(\frac{5}{2}^-_2\ \frac{1}{2})$	7.460(10)	8.31(01;17)	8.063(5) ; 7.981(15)	7.2(1)	8.1(1)	8.65	8.25
$E_x(\frac{3}{2}^-_2\ \frac{1}{2})$	8.75	10.43(44;28)	10.080(5) ; 9.800(17)			11.27	9.85
$E_x(\frac{1}{2}^-_2\ \frac{1}{2})$	9.09	11.18(47;33)				11.93	10.46
$E_x(\frac{7}{2}^-_2\ \frac{1}{2})$	9.57	11.28(24;29)				11.69	11.03
$E_x(\frac{3}{2}^-_1\ \frac{3}{2})$	11.24	12.46(18;28)				12.83	11.97
$Q(\frac{3}{2}^-)$	−4.06(8)	−2.75	−2.79(4) ; −3.15(8)	−3.6(1)	−3.2	−2.79	−3.20
$Q(\frac{7}{2}^-)$	–	−4.10	−4.19(2) ; −4.46(3)		−5.0		
$Q(\frac{5}{2}^-_1)$	–	−4.28	−4.36(3) ; −4.75(5)		−6.0		
$Q(\frac{5}{2}^-_2)$	–	1.76	1.88(1) ; 1.89(2)		2.3		
$\mu(\frac{3}{2}^-)$	3.256	2.993	2.95(6) ; 3.22(11)	3.168(13)	2.954(5)	3.02	3.01
$\mu(\frac{1}{2}^-)$	–	−0.79	−0.78(2) ; −0.87(4)		−0.76(1)		
$\mu(\frac{7}{2}^-)$	–	3.30	3.33(2) ; 3.41(7)		3.3(1)		
$\mu(\frac{5}{2}^-_1)$	–	−0.98	−0.99(2) ; −1.01(4)		−0.90(2)		
$\mu(\frac{5}{2}^-_2)$	–	−0.38	−0.37(1) ; −0.38(2)		−0.39(5)		
$B(E2;\frac{1}{2}^-)$	15.7(10)	7.30	7.81(9) ; 8.49(12)	16.2(5)	10.2		
$B(E2;\frac{7}{2}^-)$	3.4	3.4	3.67(4) ; 4.14(5)	9.92(14)	5.1		
$B(E2;\frac{5}{2}^-_1)$	–	0.91	0.98(5) ; 1.46(9)		1.5		
$B(E2;\frac{5}{2}^-_2)$	–	0.05	0.05(1) ; 0.04(1)		<0.1		
$B(M1;\frac{1}{2}^-)$	4.92(25)	4.07	4.15(2) ; 4.01(5)	4.92(7)	3.89(2)	4.10	4.13
$B(M1;\frac{5}{2}^-_1)$	–	0.004	0.004(1); 0.004(1)		0.002(1)		
$B(M1;\frac{5}{2}^-_2)$	–	0.043	0.037(1); 0.032(1)		0.02(1)		

4.5. Ground state of ^{10}B

Structure of nuclei around mass $A = 10$ and of ^{10}B, in particular, is sensitive to the details of the interactions among nucleons. This was not concluded from phenomenological studies, where the $A = 10$ and heavier p-shell nuclei are fitted quite well with interactions, such as Cohen–Kurath (CK) [162]. One may notice, however, a poor description of light p-shell nuclei, such as ^{6,7}Li, with the CK interaction adjusted to heavier p-shell nuclei. Microscopic calculations using accurate NN potentials provide, on the contrary, a very reasonable description of the spectra of light p-shell nuclei. For example, using the CD-Bonn NN potential, one obtains the lowest 9 states of ^{7}Li in the correct order [163], see the left panel of Fig. 17. The same potential, however, predicts the ground state of ^{10}B to be 1^+ [164], although experimentally it is 3^+ (right panel of Fig. 17). This is remarkable, because for all other bound p-shell nuclei, this potential predicts the correct g.s. spin (although for ^{11}B the $3/2^-_1$ ground state and the $1/2^-_1$ excited state are almost degenerate). We noticed the incorrect description of the ^{10}B

Table 5

Comparison of ^{8}Li observables between experiment [155,160,161] and theory. The OLS results with Chiral *NN* + *NNN* are calculated in the NCSM at $\hbar\Omega = 13$ MeV up through $N_{max} = 8$ as reported in Ref. [153]. The SRG results ($\alpha = 0.08$) with Chiral *NN* + *NNN* for $N_{max} = 8$; 10 are calculated at $\hbar\Omega = 16$ MeV in the IT-NCSM as reported in Ref. [158]. Results up through $N_{max} = 12$ with JISP16 [107–109] are obtained in the NCFC approach as reported in Ref. [159]. The table uses the same units as in Table 4. AV18/IL2 results are obtained in the GFMC approach as reported in Refs. [1,2] and do not include meson-exchange corrections for the magnetic moment; CD-Bonn ("CD-B") and INOY results are from Refs. [136,163], and were calculated at $N_{max} = 12$ and $\hbar\Omega = 12$ and 16 MeV respectively for CD-Bonn and INOY, with the INOY g.s. energy extrapolated to the infinite basis space. See caption to Table 4. For the JISP16 results, the energies are obtained from extrapolations to the infinite basis space, the magnetic dipole observables are nearly converged and the RMS point-proton radius and electric quadrupole observables are evaluated at $\hbar\Omega = 12.5$ MeV.

^{8}Li	Expt.	Chiral *NN* + *NNN* Okubo–Lee–Suzuki	Chiral *NN* + *NNN* SRG(0.08) $N_{max} = 8$; 10	AV18/IL2	JISP16	INOY	CD-B
$E_b(2^+)$	41.277	39.95(69)	39.90(1) ; 40.79(10)	41.9(2)	40.3(2)	41.3(5)	35.82
$\langle r^2_{pp}\rangle^{1/2}$	2.21(6)	2.09		2.09(1)	2.1	2.01	2.17
$E_x(1^+_1 1)$	0.981	1.00 (16;03)	1.027(2) ; 0.985(6)	1.4(3)	1.5(2)	1.26	0.86
$E_x(3^+_1 1)$	2.255(3)	2.75 (16;09)	2.608(3) ; 2.599(7)	2.5(3)	2.8(1)	2.87	3.02
$E_x(0^+_1 1)$	–	4.01 (84;20)	3.842(15) ; 3.537(40)			4.22	2.48
$E_x(1^+_2 1)$	3.210	4.73 (84;21)	4.632(16) ; 4.283(44)			4.90	3.25
$E_x(2^+_2 1)$	–	4.78 (44;12)	4.603(7) ; 4.443(23)			5.11	3.98
$E_x(2^+_3 1)$	–	5.94 (37;20)				6.07	5.29
$E_x(1^+_3 1)$	5.400	6.09 (70;22)				6.76	5.02
$E_x(4^+_1 1)$	6.53(20)	7.45 (36;15)		7.2(3)	7.0(3)	7.40	6.69
$E_x(3^+_2 1)$	–	8.24 (50;22)				8.92	7.57
$E_x(0^+_2 2)$	10.822	11.77 (27;29)				12.05	10.90
$Q(2^+)$	3.27(6)	2.65	2.73(1) ; 2.79(1)	3.2(1)	2.6	2.55	2.78
$Q(1^+)$	–	1.08	1.12(1) ; 1.12(1)		1.2		
$Q(3^+)$	–	−1.97	−1.92(1); −1.94(2)		−2.0		
$Q(4^+)$	–	−3.01			−3.4		
$\mu(2^+)$	1.654	1.49	–	1.65(1)	1.3(1)	1.42	1.24
$\mu(1^+)$	–	−2.27			−2.2(2)		
$\mu(3^+)$	–	2.13			2.0(1)		
$\mu(4^+)$	–	1.86			1.84(1)		
B(E2;1^+)	–	1.19			1.9		
B(E2;3^+)	–	3.70			4.6		
B(E2;4^+)	–	1.21			1.9		
B(M1;1^+)	5.0(16)	4.13	4.15(1) ; 4.14(1)		3.7(2)	4.56	4.39
B(M1;3^+)	0.52(23)	0.33	0.31(1) ; 0.30(1)		0.25(5)		

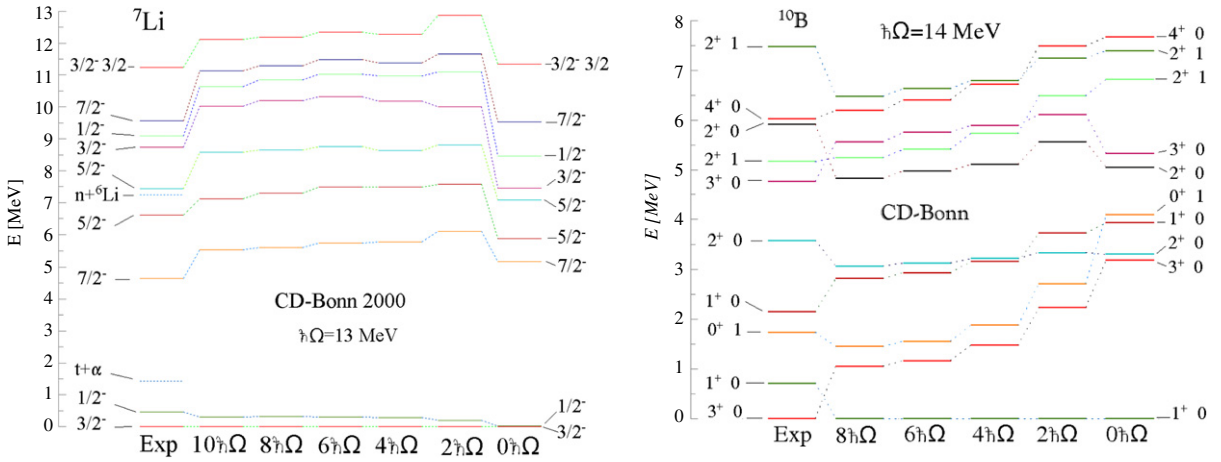

Fig. 17. Basis size dependence of the ^{7}Li (left) and ^{10}B (right) excitation energies in the range from $N_{max} = 0$ to $N_{max} = 10$ (^{7}Li) and $N_{max} = 8$ (^{10}B) calculated with the CD-Bonn 2000 *NN* potential compared to the experiment. The HO frequency of $\hbar\Omega = 13$ MeV (^{7}Li) and $\hbar\Omega = 14$ MeV (^{10}B) was used. For further details on the calculations, see Refs. [163,164].

ground state in the NCSM calculations also with the AV8′*NN* potential [132] and with the chiral N^{3}LO *NN* potential [133,151] (see the *NN* spectrum in the ^{10}B column of Fig. 18). The same was found in the GFMC calculations with the Argonne V18 (and V8′) potential [165].

Remarkably, including the *NNN* interaction, such as the TM′, to the *NN* potential, *e.g.*, AV8′, fixes the ^{10}B g.s. problem without spoiling the correct level ordering in lighter nuclei [116]. Similarly, augmenting the chiral N^{3}LO *NN* potential by the chiral N^{2}LO *NNN* interaction results in a correct description of ^{10}B and overall improvement for other p-shell nuclei [151]. This is demonstrated in Fig. 18, where we display the natural-parity excitation spectra of four nuclei in the middle of the

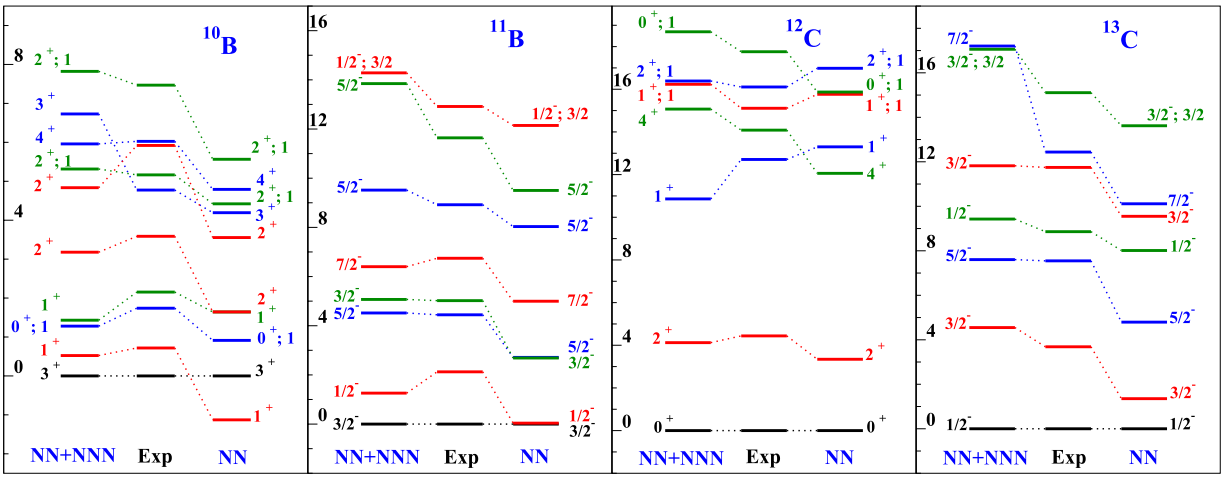

Fig. 18. States dominated by 0p-shell configurations for ^{10}B, ^{11}B, ^{12}C, and ^{13}C calculated at $N_{\max} = 6$ using $\hbar\Omega = 15$ MeV (14 MeV for ^{10}B). Most of the eigenstates are isospin $T = 0$ or $1/2$, the isospin label is explicitly shown only for states with $T = 1$ or $3/2$. The excitation energy scales are in MeV. *Source:* Adopted from Ref. [151].

Table 6
B(E2) transition rates, in e^2fm^4, from low-lying 2^+ states to the ground states of ^{10}Be and ^{10}C. Experimental values from Refs. [166,167] are compared to the NCSM calculations [168, 169] with the CD-Bonn *NN* potential and the GFMC calculations [167] with the AV18 + IL7 *NN* + *NNN* potential.

	NCSM: CD-Bonn 2000	GFMC: AV18 + IL7	Experiment
^{10}Be B(E2;$2_1^+ \to 0_1^+$)	9.8(4)	8.8(4)	9.2(3)
^{10}Be B(E2;$2_2^+ \to 0_1^+$)	0.2(2)	1.8(1)	0.11(2)
^{10}C B(E2;$2_1^+ \to 0_1^+$)	10(2)	15.3(1.4)	8.8(3)

0p-shell with both the *NN* and the *NN* + *NNN* effective interactions from χEFT. Overall, the *NNN* interaction contributes significantly to improve theory in comparison with experiment. This is especially well-demonstrated in the odd mass nuclei for the lowest, few excited states. The case of the g.s. spin of ^{10}B and its sensitivity to the presence of the *NNN* interaction is clearly evident. We note that, remarkably, the Urbana IX *NNN* interaction added to the AV18 *NN* potential does not help to revert the incorrect AV18 level ordering to produce the correct ^{10}B g.s. spin [165]. This fact demonstrates that the fine details of the *NNN* interaction are important.

4.6. E2 properties of A = 10 nuclei

The lifetimes of the low-lying 2^+ states in ^{10}Be and ^{10}C were recently measured [166,167] with the goal to test the *ab initio* nuclear-structure calculations. With the same motivation, the ^{10}Be 2_1^+ quadrupole moment measurement was recently performed using the Coulomb excitation [168]. As noted in the previous subsection, the $A = 10$ nuclei and ^{10}B, in particular, pose a challenge to *ab initio* calculations, as they manifest a substantial sensitivity to the details of the nuclear Hamiltonian. Features found in the ^{10}Be experimental studies include a two-orders of magnitude suppression of the $2_2^+ \to 0_1^+$ transition compared to the $2_1^+ \to 0_1^+$ transition [166]. Further, the $Q_{2_1^+}$ moment was found to be negative in the Coulomb excitation experiment [168]. Finally, the new lifetime measurement of the ^{10}C 2_1^+ state gives the B(E2) rate slightly weaker than that in ^{10}Be. All the above properties turned out to be challenging to explain in the GFMC calculations that showed a significant sensitivity to the presence of a *NNN* interaction in the Hamiltonian with the AV18 *NN* potential. The best results overall were obtained with the AV18 + IL7 interaction (Table 6). A reversal of the two 2^+ states in ^{10}Be states (with the ordering determined by the sign of the Q moments) was observed in calculations with the AV18 only.

We have performed extensive calculations for ^{10}C and ^{10}Be within the NCSM using the CD-Bonn 2000 *NN* potential with basis sizes up to $N_{\max} = 10$ [164,168,169] enabled by the SM code Antoine [135]. Overall, our calculations describe the $E2$ rates quite well, as seen in Table 6, even though the weaker transition in ^{10}C poses some challenge. We also find a negative Q moment of the ^{10}Be 2_1^+ state in agreement with the measurement [168] and predict a positive Q moment for the 2_2^+ state, as shown in the left panel of Fig. 19. The same prediction is found by the GFMC calculations with the AV18 + IL7 Hamiltonian.

Our ongoing calculations with the SRG-evolved chiral *NN* + *NNN* interactions show so far consistent results with our CD-Bonn 2000 results for the $E2$ properties in ^{10}Be and ^{10}C. It appears that ^{10}B is more sensitive to the *NNN* interaction, even when considering $E2$ transitions. In Ref. [151], we noticed a mixing and even reversal of the ^{10}B 1_1^+ and 1_2^+ states depending on the value of the chiral *NNN* LEC c_D. In particular, the ratio of the ^{10}B B(E2;$3_1^+0 \to 1_1^+0$) and B(E2;$3_1^+0 \to 1_2^+0$) transition

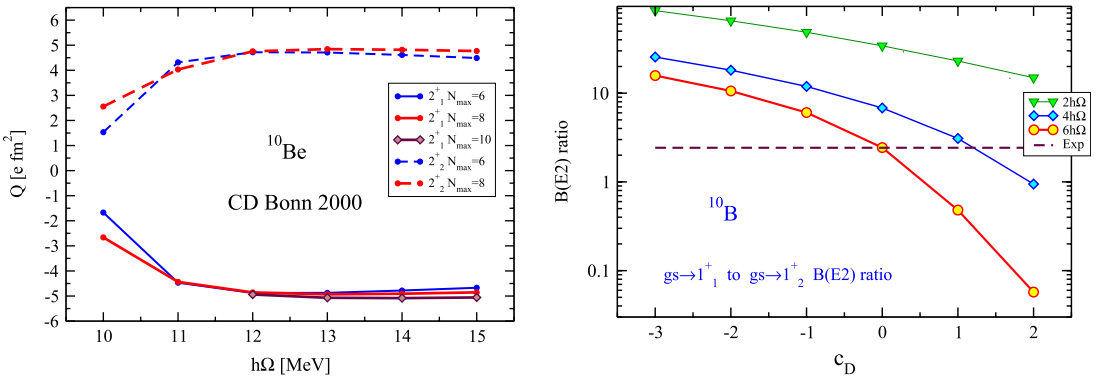

Fig. 19. Left panel: Dependence of quadrupole moments of the 2^+_1 and the 2^+_2 states of ^{10}Be on the HO frequency and the size of the basis $N_{\max}$ with the CD-Bonn 2000 *NN* potential. Right panel: Dependence of the ^{10}B B(E2;$3^+_1 0 \rightarrow 1^+_1 0$)/B(E2;$3^+_1 0 \rightarrow 1^+_2 0$) ratio on the *NNN* interaction LEC c_D with the c_E constrained by the $A = 3$ binding energy fit for different basis sizes. The chiral $NN + NNN$ interaction and the HO frequency of $\hbar\Omega = 14$ MeV were employed. The experimental value is given by the dashed line. Further details are given in Refs. [168,151], respectively.

rates changes dramatically with the c_D, as demonstrated in the right panel of Fig. 19. Interestingly, the calculations with the $c_D \sim -0.2$ fitted to the ^{3}H lifetime gives the ratio close to the experimental value of ∼2.

4.7. *Isospin-mixing correction for the* ^{10}C → ^{10}B *Fermi transition*

Superallowed Fermi β transitions in nuclei, $(J^\pi = 0^+, T = 1) \rightarrow (J^\pi = 0^+, T = 1)$, provide an excellent laboratory for precise tests of the properties of the electroweak interaction, and have been the subject of intense study for several decades (cf. Refs. [170–177]). According to the conserved-vector-current (CVC) hypothesis, for pure Fermi transitions the product of the partial half-life, t, and the statistical phase-space factor, f, should be nucleus independent and given by

$$ft = \frac{K}{G_V^2 |M_F|^2}, \tag{35}$$

with the G_V, the vector coupling constant for nuclear β decay, and $M_F = \langle \psi_f \mid T_\pm \mid \psi_i \rangle$, the Fermi matrix element. By comparing the decay rates for muon and nuclear Fermi β decay, the Cabibbo–Kobayashi–Maskawa (CKM) mixing matrix element [173] between u and d quarks (v_{ud}) can be determined and a precise test of the unitarity condition of the CKM matrix is possible under the assumption of the three-generation standard model [173].

For tests of the standard model, two nucleus-dependent corrections must be applied to experimental ft values. The first is a series of radiative corrections to the statistical phase-space factor embodied in the factors δ_R and Δ_R, giving [174]

$$f_R = f(1 + \delta_R + \Delta_R), \tag{36}$$

where δ_R is due to standard, electromagnetic ("outer") radiative correction and Δ_R is what has been referred to as the "inner" radiative correction and includes axial-vector interference terms [174,175]. The second correction modifies the nuclear matrix element M_F and is due to the presence of isospin-nonconserving (INC) forces (predominantly Coulomb). This correction is denoted by δ_C [170] and modifies the Fermi matrix element by $\mid M_F \mid^2 = \mid M_{F0} \mid^2 (1 - \delta_C)$, where $M_{F0} = [T(T+1) - T_{Z_i} T_{Z_f}]^{1/2}$ is the value of the matrix element under the assumption of pure isospin symmetry.

With the corrections δ_R, Δ_R, and δ_C, a "nucleus-independent" $\mathcal{F}t$ can be defined by

$$\mathcal{F}t = ft(1 + \delta_R + \Delta_R)(1 - \delta_C), \tag{37}$$

and the CKM matrix element v_{ud} is given by [175]

$$\mid v_{ud} \mid^2 = \frac{\pi^3 \ln 2}{\mathcal{F}t} \frac{\hbar^7}{G_F^2 m_e^5 c^4} = \frac{2984.38(6)\ \text{s}}{\mathcal{F}t}, \tag{38}$$

where the Fermi coupling constant, G_F, is obtained from muon β-decay and includes radiative corrections. Currently, ft values for thirteen superallowed transitions have been measured with an experimental precision of 0.3% or better [177]. With these precise measurements and reliable estimates for the corrections, the CVC hypothesis can be confirmed by checking the constancy of the $\mathcal{F}t$ values for each nucleus, while the unitarity condition of the CKM matrix is tested.

For the thirteen accurately measured cases, the isospin-mixing correction δ_C has been evaluated within the framework of the shell-model. For the lightest nuclei, these estimates can be confronted and validated by large-scale *ab initio* calculations. We applied the no core shell model wave functions to compute the isospin-mixing correction of the ^{10}C → ^{10}B Fermi transition in two studies [178,164]. In the latter, we used the CD-Bonn 2000 *NN* potential that included both the electromagnetic and strong interaction isospin and charge-symmetry breaking terms. The calculations were performed up to $N_{\max} = 8$ basis space and examined the HO frequency dependence of the results.

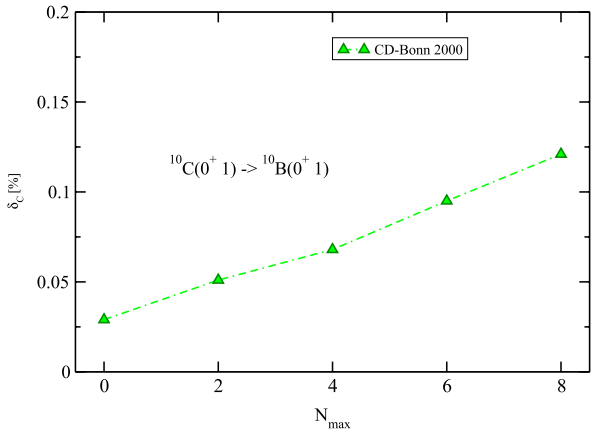

Fig. 20. Isospin-mixing correction δ_C, in %, dependence on the basis-space size for the $^{10}C(0^+1) \rightarrow {}^{10}B(0^+1)$ Fermi transition. The values correspond to calculations with the g.s. energies at the HO frequency minima at each basis space. The CD-Bonn 2000 *NN* potential was used. Further details are given in Ref. [164].

Our goal is to evaluate the Fermi matrix element

$$M_F = \langle {}^{10}B, 0^+1|T_-|{}^{10}C, 0^+1\rangle, \tag{39}$$

which is equal to $\sqrt{2}$ for an isospin-invariant system. The calculated correction δ_C is displayed in Fig. 20 for the basis space up to $N_{max} = 8$. While the δ_C correction depends only weakly on the HO frequency [164], it increases almost linearly with N_{max}. The size of the correction also depends on the position of the 1p–1h, $2\hbar\Omega$ states that influence the ground-state isospin mixing. The lower these states appear, the larger the correction. Unfortunately, the excitation energy of these states is not known experimentally. The reason for the strong N_{max} dependence is the overall decrease in the excitation energy of the 1p–1h states with increasing basis size. Our best result obtained in the $8\hbar\Omega$ space is $\delta_C = 0.12\%$. This result is compatible with the previously published value of $\delta_C \approx 0.15(9)\%$ by Ormand and Brown [176] obtained in a phenomenological treatment. In Ref. [164], we performed a rough estimate of the full δ_C via PT using an extrapolation of the position of the 1p–1h states that lead to $\delta_C \approx 0.19\%$. This is in an excellent agreement with the newest shell-model calculation of Ref. [177] that found $\delta_C = 0.18(2)\%$. The conclusion of this study was that the standard shell model estimates applied for the wide range of the super-allowed Fermi transitions [176,177] are consistent with the *ab initio* calculations of the ^{10}C decay. We note that the current value of the V_{ud} matrix element extracted from the superallowed beta decays is 0.97425 ± 0.00022. The unitarity test on the top row of the CKM matrix is $|V_{ud}|^2 + |V_{us}|^2 + |V_{ub}|^2 = 0.99995 \pm 0.00061$ [177]. Still, it will be worthwhile to revisit the ^{10}C decay calculation with the newly developed SRG evolved chiral *NN* + *NNN* Hamiltonians that might lead to a faster convergence of the relevant 1p–1h states. A more accurate determination of the ^{10}C decay will put stricter limits on the fundamental scalar current.

4.8. Neutrino-^{12}C exclusive cross sections and B(M1) transitions

The Gamow–Teller (GT) transition from the g.s. of ^{12}C to the 1^+ T = 1 isobar triplet ($^{12}B_{g.s.}$, $^{12}C(15.11\ MeV)$, $^{12}N_{g.s.}$) is a very sensitive test of nuclear-structure models for mass 12 and, particularly, of the strength of the spin–orbit interaction. The two most common p-shell approximations for the structure of the g.s. of ^{12}C ((a) the p-shell equivalent of a L = 0 S = 0 three alpha-cluster structure and (b) the closed $p_{3/2}$ shell structure) give very different (indeed opposite) predictions for the B(GT) strength to T = 11^+ triplet. In the p-shell alpha-cluster limit the g.s. of carbon has good SU(4) symmetry [444] and the Gamow–Teller transition is forbidden, because there does not exist a 1^+T = 1 state with [444] symmetry and $\sigma\tau$ operator cannot change SU(4) symmetry. This translates into an exact cancellation between the different $p_{1/2}$ and $p_{3/2}$ transition amplitudes. The observed transition strength requires the inclusion of higher SU(4) components in the wave functions and the breaking of the cancellation is quite sensitive to the assumed spin–orbit interaction. In the *jj*-coupling limit, where one assumes that the ground state of ^{12}C is described by a closed $p_{3/2}$ shell, the transition to the T = 11^+ state is pure $p_{3/2} \rightarrow p_{1/2}$. No cancellations between different transition amplitudes are allowed and the transition strength is over estimated by almost a factor of 6. When RPA correlations are included in the initial and final states the situation improves somewhat, but the transition remains over-estimated by about a factor of 4 [183,184]. The strong contrast between the predictions of the pure *jj*-coupling and the pure SU(4) limits makes this Gamow–Teller transition an ideal test case for the strength of the spin–orbit interaction and for model wave functions of mass 12.

In Ref. [182], we examined inelastic electron scattering to the 15.11 MeV state of ^{12}C, muon capture to the g.s. of ^{12}B, and neutrino scattering to the g.s. of ^{12}N using wave functions obtained with the NCSM. These different electroweak reactions probe different momentum transfers and comparisons between theory and experiment allow us to test the convergence of

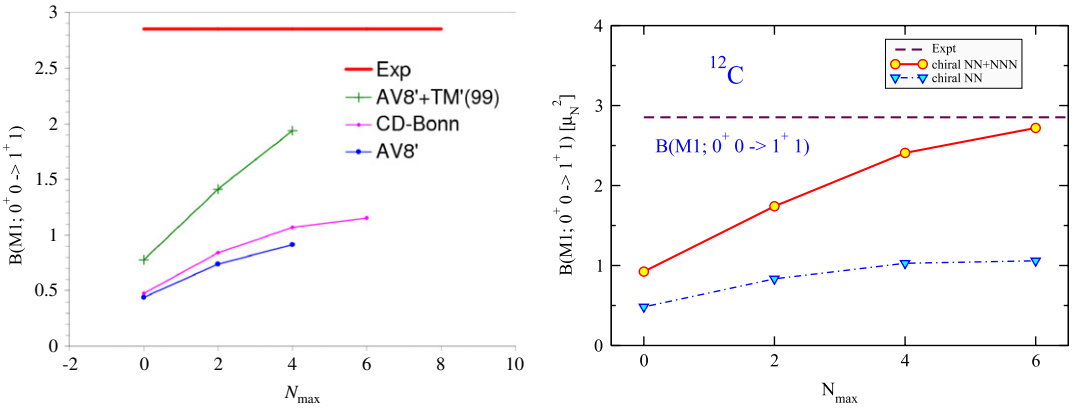

Fig. 21. Experimental and calculated B(M1;$0^+0 \rightarrow 1^+1$) values, in μ_N^2, for the 15.11 MeV $T = 11^+$ state in ^{12}C. Results obtained in basis spaces up to $6\hbar\Omega$ using OLS three-body effective interactions derived from the AV8′ + TM′(99) and AV8′ (left panel), OLS two-body effective interactions derived from the CD-Bonn *NN* potential (left panel), OLS three-body effective interactions derived from the chiral *NN* and chiral *NN* + *NNN* interactions (right panel) are compared. The HO frequency of $\hbar\Omega = 15$ MeV was used.

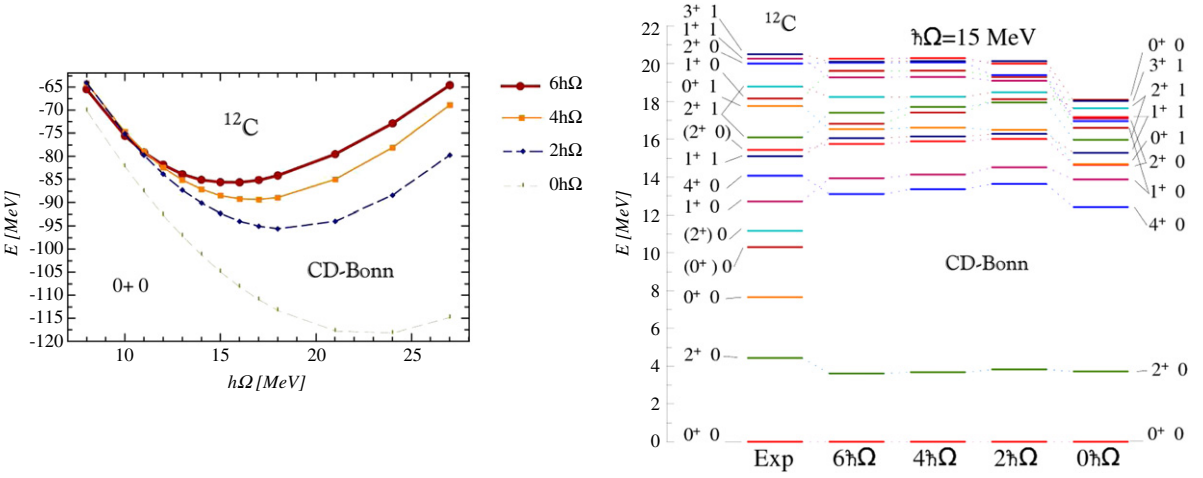

Fig. 22. Basis-size dependence of the ^{12}C (right) excitation energies in the range from $N_{max} = 0$ to $N_{max} = 6$ calculated with the CD-Bonn 2000 *NN* potential compared to the experiment. The HO frequency of $\hbar\Omega = 15$ MeV (^{12}C) was used. For further details on the calculations, see Refs. [163,164].

the NCSM with increasing basis size. Further, we investigated the contributions of a three-nucleon force, in particular, the chiral-symmetry-based Tucson–Melbourne TM′(99) interaction [14].

Our B(M1; $0^+0 \rightarrow 1^+1$) results are presented in Fig. 21. The calculations with 2-body forces, *e.g.*, with the CD-Bonn *NN* potential that describes the ^{12}C p-shell dominated states quite well, as seen in Fig. 22, show saturation and underpredict the experiment by almost a factor of three. By including the TM′(99) *NNN* interaction, the B(M1) value increases dramatically. The same trend we found in calculations with the chiral *NN* and *NN* + *NNN* interactions, as shown in the right panel of Fig. 21 and in Fig. 2 of Ref. [151].

Table 7 shows the comparison between the theoretical and experimental neutrino scattering cross section for the same selections of Hamiltonians and basis spaces. These results show a similar trend to the electron scattering results above. In this case, the neutrino spectrum for electron neutrinos from decay-at-rest (DAR) of the pion peaks around 30 MeV and the average momentum transfer is about 40 MeV/c. The CD-Bonn interaction (without the *NNN*) results indicate an approach to convergence by $6\hbar\Omega$, but experiment is under-predicted by about a factor of 2.4. When the *NNN* is included with the AV8′ interaction the predicted cross section is only 30% lower than experiment. Based on the similarity of trends with the electron scattering results, we anticipate that when the model space is eventually expanded to $6\hbar\Omega$ theory would be within 15% of experiment.

Muon capture involves a higher momentum transfer than the (ν_e, e^-) reaction and the average momentum transfer is $q \sim 100$ MeV/c. By $6\hbar\Omega$ the CD-Bonn calculations show signs of converging, yet experiment is underestimated by a factor of 2.6. The inclusion of the *NNN* shows a significant improvement and, for $4\hbar\Omega$, theory is 34% lower than experiment. Again extrapolating using the trends of the inelastic electron-scattering results suggests that a $6\hbar\Omega$ calculation that included a realistic *NNN* would come within 20% of experiment.

Table 7
Predicted weak interaction rates for the $^{12}C \rightarrow T = 11^+$ transitions. The units are 10^{-42}cm^2 for the (ν_e, e^-) DAR cross section, 10^{-40}cm^2 for (ν_μ, μ^-) DIF cross section and 10^3 sec^{-1} for muon capture. The abbreviation CDB refers to the CD-Bonn *NN* potential.

Interaction	CDB $2\hbar\Omega$	CDB $4\hbar\Omega$	CDB $6\hbar\Omega$	AV8′ + TM′(99)$4\hbar\Omega$	Experiment
(ν_e, e^-)	2.27	3.2	3.69	6.8	8.9±0.3±0.9 [179]
(ν_μ, μ^-)	0.218	0.337	0.374	0.65	0.56±0.08±0.1 [180]
μ-capture	1.46	2.07	2.38	4.43	6.0±0.4 [181]

The (ν_μ, μ^-) neutrino cross section to $^{12}N_{g.s.}$ corresponds to the LSND muon neutrinos from decay-in-flight (DIF) of the pion. This spectrum involves neutrinos up to about 250 MeV, with a average neutrino energy of about 150 MeV and an average momentum transfer of about 200 MeV/c. In this case the $6\hbar\Omega$ CD-Bonn calculation is off by a factor of 1.5 compared with experiment. The $4\hbar\Omega$ calculation that includes the 3-body TM′(99) interaction is, in fact, in agreement with experiment. However, based on the trends established above, this suggests that a larger model space may over-predict experiment. Examining the elastic-scattering form factor suggests that the problem lies in the fact that at 200 MeV/c the predicted form factor is too large [182]. Of course, as the model space is increased, we expect the form factor to be shifted down in momentum.

4.9. Beta decay of ^{14}C

The measured lifetime of ^{14}C, 5730 ± 30 years, is a valuable chronometer for many practical applications ranging from archeology [185] to physiology [186]. The ^{14}C lifetime is anomalously long compared to lifetimes of other light nuclei undergoing the same decay process, allowed Gamow–Teller (GT) beta-decay. This lifetime poses a major challenge to theory since traditional realistic *NN* interactions alone appear insufficient to produce the effect[187], though it may be fit by a phenomenological *NN* tensor force [188].

Using Fermi's Golden rule for the transition rate, the half life $T_{1/2}$ for ^{14}C is given by

$$T_{1/2} = \frac{1}{f(Z, E_0)} \frac{2\pi^3 \hbar^7 \ln 2}{m_e^5 c^4 G_V^2} \frac{1}{{g_A}^2 |M_{\rm GT}|^2}, \tag{40}$$

where $M_{\rm GT}$ is the reduced GT matrix element; $f(Z, E_0)$ is the Fermi phase-space integral; $E_0 = 156$ keV is the β endpoint; $G_V = 1.136\ 10^{-11}$MeV^{-2} is the weak vector coupling constant; $g_A = 1.27$ is the axial vector coupling constant; and m_e is the electron mass. $M_{\rm GT}$ for the transition from the initial $^{14}C(J^\pi, T) = (0^+, 1)$ ground state (Ψ_i) to the $^{14}N(1^+, 0)$ ground state (Ψ_f) is defined by the spin–isospin operator $\sigma(k)\tau_+(k)$ acting on all nucleons, k:

$$M_{\rm GT} = \sum_k \left\langle \Psi_f \| \sigma(k)\tau_+(k) \| \Psi_i \right\rangle. \tag{41}$$

Since the initial state has total spin zero, $M_{\rm GT}$ is equal to the M-dependent GT matrix element $M_{\rm GT}^M$,

$$M_{\rm GT}^M = \sum_{\alpha,\beta} \langle \alpha | \sigma\tau_+ | \beta \rangle\ \rho_{\alpha\beta}, \tag{42}$$

where $\langle \alpha | \sigma\tau_+ | \beta \rangle$ is the one-body matrix element between HO single-particle states α and β, which is non-vanishing only when both single-particle states are in the same shell, and the one-body density matrix $\rho_{\alpha\beta} \equiv \left\langle \Psi_f | a_\alpha^\dagger a_\beta | \Psi_i \right\rangle$.

In order to reproduce the measured half life of $T_{1/2} \simeq 5730$ years, the GT matrix element must be anomalously small, $|M_{\rm GT}^M| \simeq 2 \times 10^{-3}$, in contrast with a conventional strong GT transition in a light nucleus with $|M_{\rm GT}| \simeq 1$. A recent calculation has determined the GT matrix element for the beta decay of ^{14}C, using chiral *NN* + *NNN* interactions [189]. These investigations show that the very long lifetime for ^{14}C arises from a cancellation between 0p-shell *NN*- and *NNN*-interaction contributions to the GT matrix element, as shown in Fig. 23. These ^{14}C results were obtained in the largest basis space achieved to date with *NNN* interactions, $N_{\rm max} = 8$ ($8\hbar\Omega$) or approximately one billion configurations.

Looking into the detailed changes within the p-shell, one finds that the *NNN* interaction introduces a systematic shift of strength away from 1-body density matrix terms involving transitions between the $0p_{3/2}$ and the $0p_{1/2}$ orbits to 1-body density matrix elements involving transitions within the $0p_{1/2}$ orbits. The shift is about 30% of the magnitudes of these 1-body density matrix terms and supports a recurring theme of three-nucleon forces in p-shell nuclei — they play a significant role in the spin-sensitive properties of spin–orbit pairs. One should note that the observed shifts within the p-shell due to the *NNN* interaction are similar to what Ref. [190] accomplished with a density-dependent effective *NN* interaction obtained by modeling leading contributions from the chiral *NNN* interaction. However, our net contributions from other shells, which are absent in Ref. [190], overwhelm the net p-shell contribution, as seen in Fig. 23. That is, while the s-shell and sd-shell contributions nearly cancel, all the shells above the sd-shell contribute about a factor 2 greater than the now-suppressed p-shell contribution.

In order to further test the *ab initio* wavefunctions and the effects of the *NNN* interaction, we present in Table 8 the contributions to selected electromagnetic properties of ^{14}N adopted from Ref. [189]. We see that the *NNN* interaction has

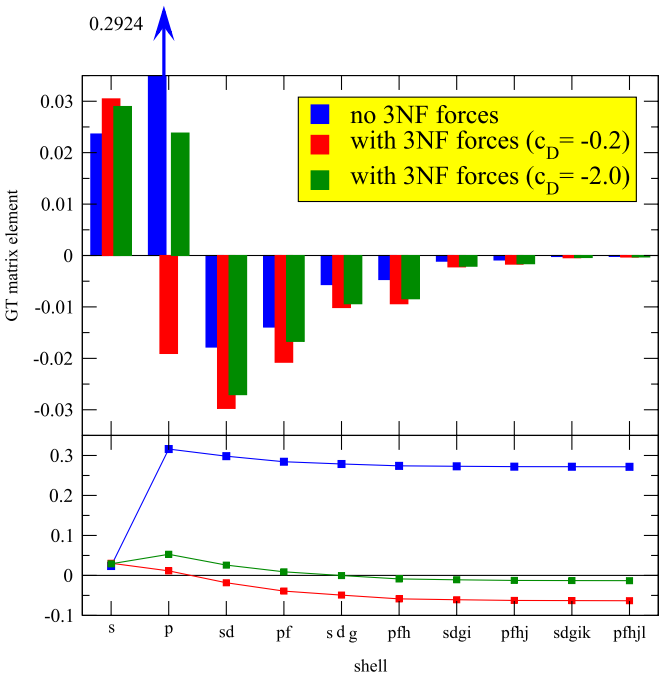

Fig. 23. Contributions to the ^{14}C beta decay matrix element as a function of HO shell when the nuclear structure is described by the χEFT interaction. Top panel displays the contributions with (two right bars of each triplet) and without (leftmost bar of each triplet) the *NNN* force at $N_{\max} = 8$. Contributions are summed within each shell to yield a total for that shell. The bottom panel displays the running sum of the GT contributions over the shells. Note the order-of-magnitude suppression of the 0p-shell contributions arising from the *NNN* force.
Source: Adopted from Ref. [189].

Table 8
Properties of ^{14}N without and with *NNN* interaction in the $N_{\max} = 8$ basis space with $\hbar\Omega = 14$ MeV. The magnetic moments, which tend to converge rapidly, are obtained at $N_{\max} = 6$. The point proton root-mean-square radius (RMS) is quoted in fm. We corrected the measured charge radius (2.56(1) fm) for the finite proton charge contribution. The magnetic moment μ is in nuclear magnetons $e\hbar/2mc$, and the quadrupole moment is in $e^2\,fm^4$ (all for the g.s.). The B(M1) is the transition from the g.s. to the $(0^+, 1)$ state (the isobaric analog of the ^{14}C g.s.)

Observable	Experiment [191]	*NN* only	*NN*+ *NNN* $c_D = -0.2$	*NN*+ *NNN* $c_D = -2.0$
RMS	2.42(1)	2.28	2.25	2.24
Q	1.93(8)	1.87	1.03	1.19
μ	0.404	0.379	0.347	0.347
B(M1)	0.047(2)	1.002	0.037	0.098

substantial influence on the magnetic-dipole transition in ^{14}N from the g.s. to the $(0^+, 1)$ analog state of the ^{14}C g.s. though the mechanism for this suppression is quite different from the GT transition. In this M1 transition, we find significant cancellation between the nucleon spin and proton angular momentum contributions. Without the *NNN* interaction, spin and angular momentum contributions add constructively. The g.s. electric-quadrupole moment (Q), the g.s. magnetic moment (μ) and the B(M1) from the g.s. to the (0+, 1) state are all reduced, when we include the *NNN* interaction. We expect *RMS* and Q to increase with basis-space size, while the g.s. energy, μ and the B(M1) will be less effected. The role of the *NNN* interaction on the electroweak properties of these nuclei is indeed multi-faceted.

There are additional challenges to understanding GT transition rates in $A = 14$ nuclei, beyond the half life of ^{14}C, which is now resolved, as discussed above. For example, working in collaboration with experimentalists, we uncovered a puzzle in the GT-excited state strengths in $A = 14$ nuclei [192]. Its resolution may lie in the role of intruder-state admixtures, but this will require further investigation with larger basis spaces.

4.10. Binding energies of p-shell nuclei with INOY NN interaction

A new type of interaction, which respects the local behavior of traditional *NN* interactions at longer ranges but exhibits a non-locality at shorter distances, was recently proposed by Doleschall et al. [101,193]. The authors explore the extent to

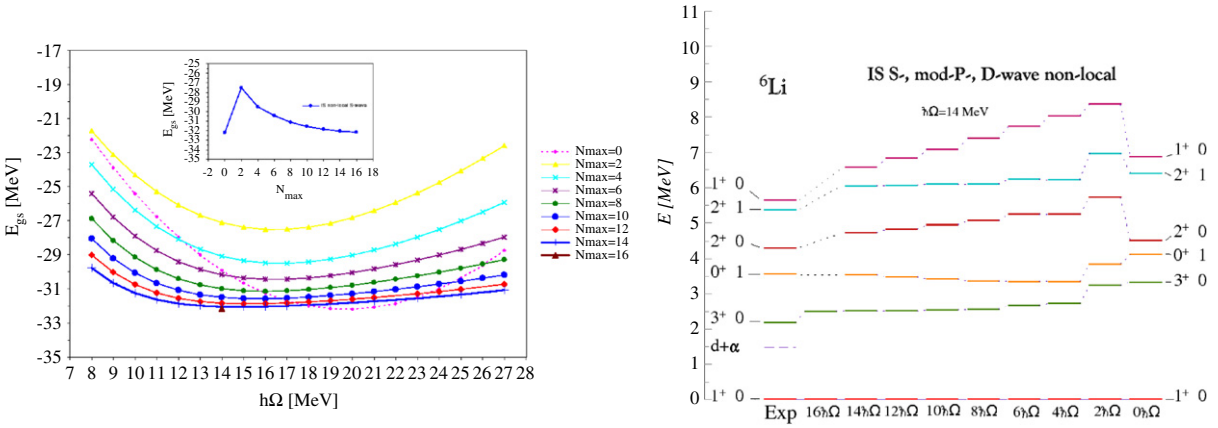

Fig. 24. Convergence of the ^{6}Li ground-state energy (left panel) and excitation energies (right panel) with the INOY *NN* potential. The NCSM calculations were performed in a wide range of basis sizes and HO frequencies using the two-body OLS renormalizations.

Table 9
Binding energies of selected p-shell nuclei from NCSM calculations with the INOY *NN* interaction.

	^{3}H	^{3}He	^{4}He	^{6}He	^{6}Li	^{7}Li	^{7}Be	^{8}He
INOY [MeV]	8.47(1)	7.71(1)	29.10(5)	29.38(10)	32.3(2)	39.6(4)	37.9(4)	30.30(30)
Expt. [MeV]	8.48	7.72	28.30	29.27	31.99	39.24	37.60	31.41
	^{8}Li	^{8}B	^{9}Li	^{9}Be	^{10}B	^{12}C	^{14}C	^{16}O
INOY [MeV]	41.3(5)	36.1(1.0)	45.9(7)	59.1(1.2)	62.5(2.0)	93.5(2.5)	107.0(2.5)	138.0(4.0)
Expt. [MeV]	41.28	37.74	45.34	58.16	64.75	92.16	105.28	127.62

which effects of multi-nucleon forces can be absorbed by non-local terms in the *NN* interaction. They investigated if it is possible to introduce non-locality in the *NN* interaction, so that it correctly describes the three-nucleon bound states, while still reproducing *NN* scattering data with high precision. The so-called IS version of this interaction, introduced in Ref. [193], contains short-range non-local potentials in $^1S_0$ and $^3S_1 - ^3D_1$ partial waves while higher partial waves are taken from Argonne V18. In the NCSM calculations, we were mostly using the IS-M version, which includes non-local potentials also in the *P* and *D* waves [193]. For this version, the on-shell properties of the triplet *P*-wave interactions have been modified in order to improve the description of *NNN* analyzing powers. The $^3P_0$ interaction was adjusted to become less attractive, the $^3P_1$ became more repulsive, and the $^3P_2$ more attractive. Unfortunately, this gives a slightly worse fit to the Nijmegen ^3P phase shifts.

The eigenenergy convergence of NCSM calculations with the INOY *NN* potential is very good as demonstrated in the left panel of Fig. 24. Using the OLS two-body effective interaction, we obtain a smooth convergence with $N_{\max}$ and a weak dependence on the HO frequency unlike with different OLS renormalized *NN* potentials. As the convergence is very uniform with respect to the HO frequency with systematic changes with $N_{\max}$, we can extrapolate, *e.g.*, assuming an exponential dependence on $N_{\max}$ as $E(N_{\max}) = E_\infty + a\ \exp(-bN_{\max})$. The INOY *NN* potential has the attractive feature of being just two-body, which makes calculations much easier, but at the same time including at least a part of the *NNN* effects. Indeed, as seen in Fig. 24, not only the binding energy is larger than with other *NN* potentials, such as the chiral N^{3}LO *NN*, but also, e.g., the 3^+ excited state of ^{6}Li is pushed lower, closer to experiment, due to enhancement of the spin–orbit interaction strength. Compare the right panel of Figs. 5 and 24.

We applied the INOY *NN* potential in many NCSM studies, including the investigation of He radii [138], the ^{7}Be$(p,\gamma)^8$B capture [163], the study of ^{9}Be and ^{11}Be isotopes [194], the study of electromagnetic moments of Li and Be isotopes [136] or *E*2 transitions in Carbon isotopes [169]. In Table 9 we summarize the binding energies of a wide range of p-shell nuclei calculated with the INOY *NN* interaction in the NCSM. The results correspond to extrapolated values with error estimates in parenthesis. We find a remarkably good agreement with experiment. Even nuclei with extreme isospin, such as ^{8}He, are bound (with respect to ^{6}He). There is, however, some evidence for overbinding in $N = Z$ nuclei, i.e., ^{4}He and ^{16}O. Linked to the overbinding is the underestimation of radii and E2 transitions. In ^{4}He we find the point proton radius of 1.37(1) fm compared to the experimental 1.46 fm. Similarly, we find the ^{6}He and ^{8}He charge radii underestimated with this potential [138].

4.11. Ab initio description of ^{12}C and ^{16}O with SRG-transformed chiral NN + NNN interactions

Through a recent combination of conceptual and computational developments, it became possible to extend the range of previous NCSM studies, using full *NNN* interactions, to significantly larger model spaces and particle numbers. As discussed in Section 3.4, the SRG approach has been recently adapted for the NCSM calculations with *NN* plus *NNN* interactions

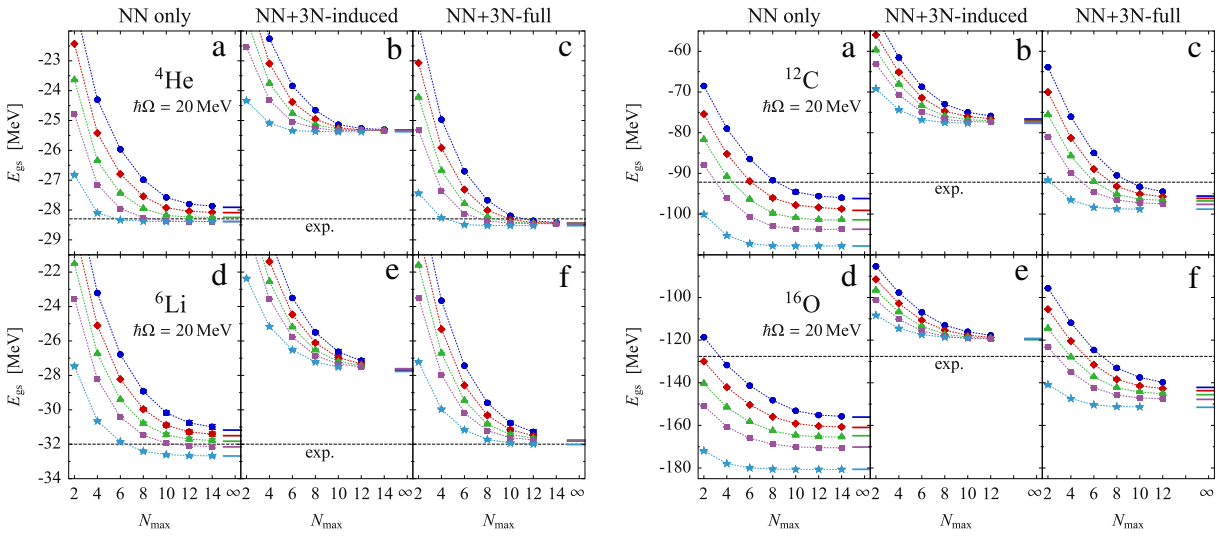

Fig. 25. IT-NCSM g.s. energies for ^{4}He, ^{6}Li, ^{12}C and ^{16}O as a function of N_{max} for the three types of Hamiltonians (see column headings) for a range of flow parameters: $\alpha = 0.04\,\mathrm{fm}^4$ (●), $0.05\,\mathrm{fm}^4$ (◆), $0.0625\,\mathrm{fm}^4$ (▲), $0.08\,\mathrm{fm}^4$ (■), and $0.16\,\mathrm{fm}^4$ (★). Error bars indicate the uncertainties of the threshold extrapolations. The bars at the right-hand-side of each panel indicate the results of exponential extrapolations of the individual N_{max}-sequences. For further details see Ref. [130].

[128,129]. Its advantage compared to the OLS approach is, first, the variational character of calculations, as the SRG is applied on free-nucleon forces in the momentum space (although using the HO expansion, in particular, for *NNN* interactions) without any connection to the many-body HO basis truncation. A smooth extrapolation of eigenenergies then becomes much more straightforward. Second, the SRG dependence on the evolution parameter λ (or α) can be utilized as a gauge of the unitarity or a violation of the unitarity by the transformation. In another important development, a transformation from *NNN* Jacobi matrix elements to a *JT*-coupled representation with a highly efficient storage scheme was proposed and implemented [130], which allows us to handle *NNN* matrix-element sets of unprecedented size in the Slater-determinant basis calculations. While the previous scheme [116,117] was limited to the maximum of $N_{max} = 8$ basis size, the new scheme, based on the expressions derived in Ref. [117], but with a new, more clever factorization, is applicable to $N_{max} = 14$ spaces and beyond. Finally, the importance-truncated NCSM approach has been introduced [195,196]. This approach, further discussed in Section 5.2, uses many-body PT to select a subset of basis states of the $N_{max}\hbar\Omega$ space prior to the Hamiltonian diagonalization. While the full-space calculations with the *NNN* interactions for heavy p-shell nuclei are limited to $N_{max} = 8$, the importance-truncated NCSM approach allows us to reach, *e.g.*, $N_{max} = 12$ for ^{16}O [130].

IT-NCSM calculations of g.s. energies for ^{4}He, ^{6}Li, ^{12}C and ^{16}O are presented in Fig. 25. The SRG transformed chiral *NN* + *NNN* interactions were used. In particular, the chiral *NN* at N^{3}LO [27,28] and the chiral *NNN* at N^{2}LO in the local form [146] with low-energy constants determined from the triton binding energy and β-decay half-life [145], as described in Section 4.1. In order to disentangle the effects of the initial and the SRG-induced *NNN* contributions, three different Hamiltonians were considered. (1) *NN only*: starting from the chiral *NN* interaction only, the SRG-evolved *NN* contributions are kept. (2) *NN*+*NNN-induced*: starting from the chiral *NN* interaction the SRG-evolved *NN* and the induced *NNN* terms are kept. (3) *NN*+*NNN-full*: starting from the chiral *NN*+*NNN* interaction all SRG-evolved *NN* and *NNN* terms are kept. For each Hamiltonian the dependence of the g.s. energies was assessed on the flow-parameter α. Five values were used, $\alpha = 0.04\,\mathrm{fm}^4$, $0.05\,\mathrm{fm}^4$, $0.0625\,\mathrm{fm}^4$, $0.08\,\mathrm{fm}^4$, and $0.16\,\mathrm{fm}^4$, which correspond to momentum scales $\lambda = \alpha^{-1/4} = 2.24\,\mathrm{fm}^{-1}$, $2.11\,\mathrm{fm}^{-1}$, $2\,\mathrm{fm}^{-1}$, $1.88\,\mathrm{fm}^{-1}$, and $1.58\,\mathrm{fm}^{-1}$, respectively. For extrapolations to infinite model space, $N_{max} \to \infty$, simple exponential fits based on the last 3 or 4 data points were employed. The ^{4}He and ^{6}Li results reproduced here from the original Ref. [130] agree completely with the previously published full space NCSM calculations with the same SRG evolved chiral Hamiltonians [128,129]. The general pattern can be observed: The *NN*-only Hamiltonian exhibits a severe α-dependence indicating sizable induced *NNN* contributions. Their inclusion in the *NN* + *NNN*-induced Hamiltonian leads to g.s. energies that are practically independent of α, confirming that induced *NNNN* contributions are irrelevant when starting from the *NN* interaction only. Therefore, the *NN* + *NNN*-induced results can be considered equivalent to a solution for the initial *NN* interaction. The ^{16}O binding energy per nucleon of 7.48(4) MeV [130] is in good agreement with a recent coupled-cluster Λ-CCSD(T) result of 7.56 MeV for the 'bare' chiral *NN* interaction [6]. In contrast to light nuclei the ground-state energies of ^{12}C and ^{16}O obtained with the *NN* + *NNN*-full Hamiltonian do show a significant α-dependence, as evident from the right panel of Fig. 25(c) and (f). The inclusion of the initial chiral *NNN* interaction leads to induced *NNNN* contributions, whose omission causes the α-dependence. Detailed analysis showed that the c_3 part of the two-pion exchange term of the chiral *NNN* interaction is dominantly responsible for this effect [197].

In Fig. 26, we show the excitation spectrum of ^{12}C. Unlike for the absolute energies, the α-dependence of the excitation energies is quite weak. Overall, the spectrum agrees well with the calculation presented in Ref. [151] for $N_{max} = 6$, discussed

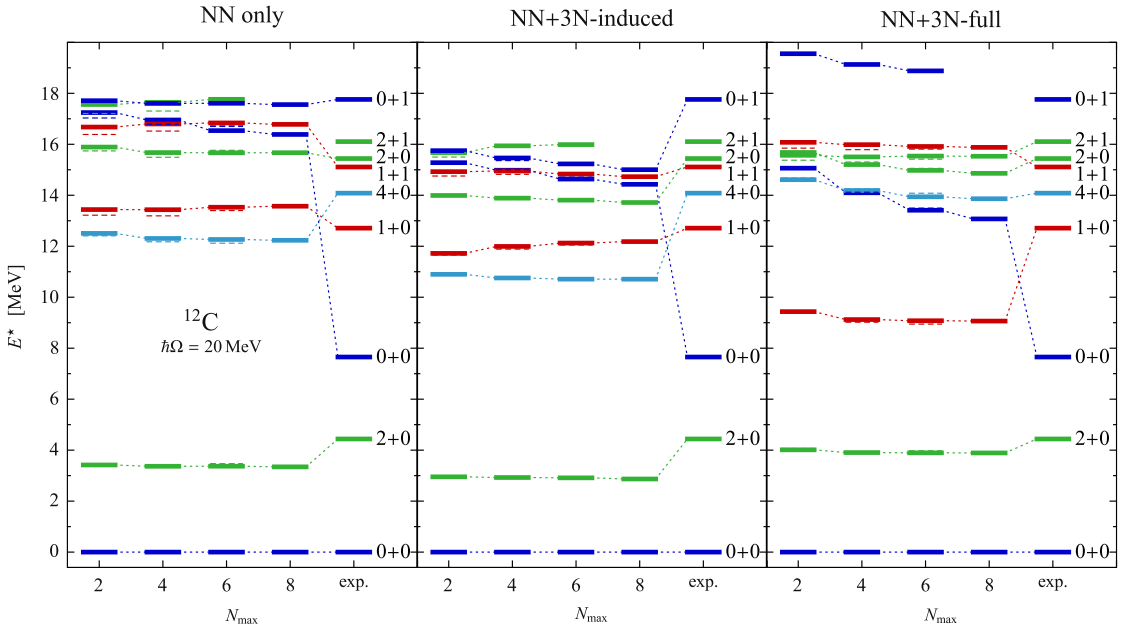

Fig. 26. Excitation spectrum for the lowest positive-parity states (labeled $J\pi T$) in ^{12}C for the *NN*-only, the *NN* + *NNN*-induced, and the *NN* + *NNN*-full Hamiltonian with $\alpha = 0.08$ fm^4. The thin dashed bars (mostly hidden) show results for $\alpha = 0.0625$ fm^4. For further details see Ref. [130].

in Section 4.5, where a different OLS-transformed chiral *NNN* interaction was used ($c_D = -1$ instead of the present $c_D = -0.2$ with the c_E constrained by $A = 3$ binding-energy fit in both cases). Considering the changes in the spectrum caused by the inclusion of the induced *NNN* interaction and the initial *NNN* interaction, it is evident that the induced *NNN* terms only lead to an over-all compression of the spectrum, whereas the initial *NNN* interaction affects the individual levels in very different ways, thus changing the level ordering. In comparison to the experimental spectrum, the first 2^+ and 4^+ states are significantly improved by the inclusion of the initial *NNN* interaction. The first 1^+ state, however, is pushed too low by the initial *NNN* interaction, ending up in clear disagreement with experiment. The only other state, which is not well-described is the first-excited 0^+ state, the famous Hoyle state. Though the *NNN* interaction improves the situation, the NCSM basis is not well-suited for the description of strong α-clustering in this state, which gives rise to the very slow convergence (for a complementary approach based on chiral EFT see [7]). For further details see the original article, Ref. [130].

4.12. NCSM calculations for light sd-shell nuclei

While the majority of NCSM applications so far has been for *s*- and p-shell nuclei, calculations for light sd-shell nuclei are becoming feasible. Recently, the first NCSM calculations for neutron rich Carbon isotopes, ^{16}C, ^{18}C and ^{20}C, have been performed using both the OLS and the SRG transformed interactions [169]. In Fig. 27, we present the NCSM calculated excitation spectrum of ^{18}F obtained with the OLS transformed chiral N^{3}LO *NN* potential. We find a similar pattern of rapid convergence of the excitation energies as for p-shell nuclei. All the low-lying displayed levels are sd-shell dominated. Their association with the experimental levels is only tentative as some of the experimental levels may be of intruder character.

4.13. NCSM calculations for unnatural parity states

Unnatural-parity states in light nuclei provide additional challenges for the NCSM, since they are typically less bound than the natural-parity states that have been the primary focus of most *ab initio* approaches to date. Therefore, the unnatural-parity states expected to show slower convergence in a HO basis than the more deeply bound natural-parity states. For example, in ^{12}C the lowest unnatural-parity state, the 3^- state, lies at 9.641 MeV of excitation, which is 2.368 MeV into the continuum, *i.e.*, above the threshold for breakup into three alphas.

The unnatural-parity states present an additional computational challenge — they require a larger basis space (N_{max} is greater by unity) than the corresponding natural-parity states. For example, we note that the m-scheme dimensions of the (natural, unnatural) pair of parity basis spaces in ^{12}C at $N_{max} = (4, 5)$ are (1,118,926 and 6,208,522), respectively. For the pair $N_{max} = (6, 7)$ the m-scheme dimensions are (32,598,920 and 140,881,044), respectively. When we also note that the computational size grows as the matrix dimension to the power 1.5 [140], we find an order of magnitude increase in computational resources for the unnatural-parity states compared with the natural-parity states to which they are paired.

In our first *ab initio* NCSM papers [8,9] we presented the natural and unnatural parity states for ^{12}C obtained with the CD-Bonn and AV8′ interactions using the OLS renormalization procedure. We found that the excitation energy of the lowest

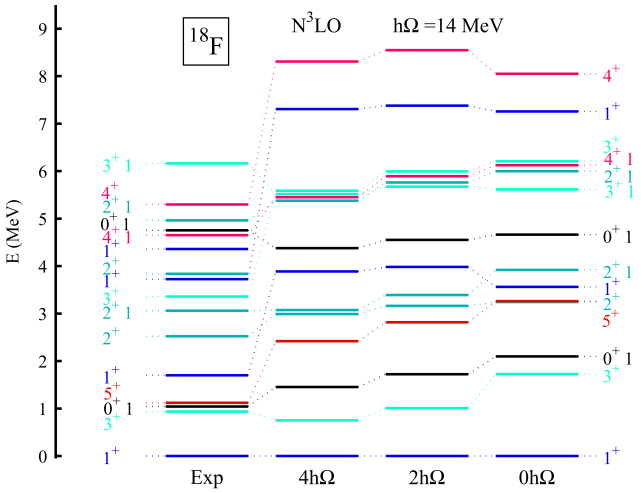

Fig. 27. Excitation spectrum for the lowest positive-parity states in ^{18}F calculated with the OLS transformed N^{3}LO *NN* potential.

3^- came down to (15.566, 15.375) MeV at $N_{\max} = 5$ (when compared with the corresponding $N_{\max} = 4$ g.s. energies) but these excitation energies had decreased by 1.5 MeV from their values at $N_{\max} = 3$ (when compared with the corresponding $N_{\max} = 2$ g.s. energies). With such a sharp drop and with few increments in $N_{\max}$ it was not possible to estimate a converged excitation energy. The other feature evident from the spectra is that the unnatural-parity spectra tended to be spread out compared with the experimental spread, a feature also seen in the natural-parity spectra. These two features of a positive shift and a spectral spread are common characteristics of the subsequent *ab initio* NCSM examples we now mention.

It is worth noting that our investigations of $A = 6$ spectra [137] with the CD-Bonn interaction showed an encouraging relative convergence trend. In particular, the unnatural-parity states had their positive shift relative to the natural-parity states decrease significantly in the highest $N_{\max}$ increment (7–9 for unnatural parity vs. 6–8 for natural parity).

In the examples of ^{10}B and ^{10}Be, we found [164] with AV8' and CD-Bonn that the excitation energies of the lowest unnatural-parity states were only about 1–2 MeV too high compared with experiment. These results were obtained using the pair of basis spaces $N_{\max} = (8, 9)$ for the (natural, unnatural) parity states, respectively. In these nuclei, the convergence of the gap between the lowest natural and unnatural parity states may be more favorable since the experimental gap is only 4.39 MeV for ^{10}B and 5.96 MeV for ^{10}Be. As we already discussed in Section 4.5, the *ab initio* NCSM produces the incorrect g.s. spin for ^{10}B with either AV8' or CD-Bonn Ref. [164]. One obtains the correct g.s. spin for ^{10}B when realistic 3NFs are included [116,151].

Further evidence that the higher-than-needed gap between natural and unnatural parity states in the NCSM is due to different rates of convergence is seen in the spectra of ^{9}Be calculated with CD-Bonn [139]. In this case, the convergence is studied by introducing alternative converging sequences for the NCSM with the OLS renormalization method. For example, by allowing the renormalized interaction to be defined for a single basis that includes both the natural and unnatural values of $N_{\max}$ (i.e. by adopting the OLS result for the larger of the two $N_{\max}$ values), the gap between natural and unnatural parities is more rapidly convergent and closer to the experimental gap at each pair of $N_{\max}$ values. This procedure results in the improved convergence of the unnatural-parity excitation energies for ^{9}Be shown in the right panel of Fig. 28 compared with the conventional procedure (spectra for each parity obtained with OLS procedure using the $N_{\max}$ of that basis) shown in the left panel. In addition the gap between unnatural and natural parity states is lowered closer to the experimental gap with the alternative converging sequence.

Concerning the ^{9}Be unnatural-parity states, and even more apparent for ^{11}Be, the position of the S-wave dominated $1/2^+$ state as well as other unnatural-parity states is also strongly affected by the continuum. These effects are not included in the NCSM, which results, *e.g.*, in an incorrect NCSM prediction of the ground state of ^{11}Be [194]. However, as we discuss later in this review, an extension of the NCSM by the Resonating Group Method is capable to describe these kinds of states successfully as demonstrated for ^{11}Be in Ref. [216].

Finally, it is worth noting that calculations with the nonlocal JISP16 NN interaction have produced unnatural-parity spectra in the Be isotopes with only about a 1 MeV shift upwards relative to the experimental excitation energies [198]. The residual differences between theory and experiment are close to the assessed uncertainties in these calculations. These results are encouraging since JISP16 both simulates the role of 3NFs and is sufficiently soft that nearly convergent results are accessible.

Thus, while most of the cases investigated to date show there is an overall shift relative to the natural-parity states (compared with experiment), it may largely be a case where the $1\hbar\Omega$ states converge more slowly than the $0\hbar\Omega$ states. Of course, we cannot rule out the possibility that the 3NFs introduce a different shift into the unnatural-parity states compared to the shift they introduce into the natural-parity states. In any case, the apparent discrepancy of a larger-than-needed gap

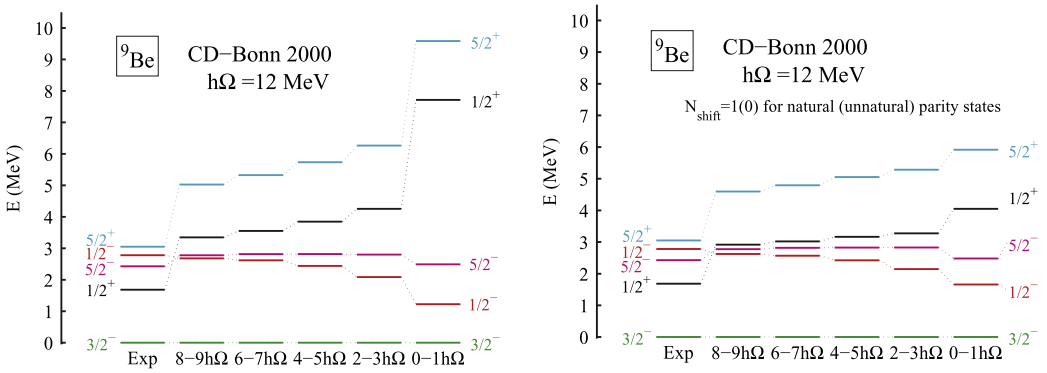

Fig. 28. Spectrum of natural- and unnatural-parity states of ^{9}Be calculated with CD-Bonn-2000 NN interaction using the OLS method. The spectra on the left use the N_{max} value for each basis space for which the spectra are evaluated. The spectra on the right use the same N_{max} value for the natural- and unnatural-parity states, i.e. the value determined by the N_{max} of the unnatural-parity states. See Ref. [139] for details.

between the natural and unnatural parity states in most calculations may not be so large, when more completely converged calculations including 3NFs are obtained. Thus, it remains for future work to fully determine if there is or is not an issue with the unnatural-parity states.

5. Extensions of the NCSM for treating heavier mass nuclei

To extend the NCSM approach to heavier nuclei, for which the A-nucleon model spaces become unmanageable with existing computers, new techniques will be necessary. For the last few years we have been investigating three techniques for extending the NCSM to heavier-mass nuclei, particularly to those in the *sd*- and *pf*-shells. These are: (1) the *ab initio* Shell Model with a Core method [152,199], (2) an improved Importance Truncation approach [196,200], and (3) the NCSM within an Effective Field Theory (EFT) framework [201–203]. Approaches (1) and (3) are also discussed in the review article on *Effective interactions and operators in no core shell model* by Stetcu and Rotureau [82] in this volume. In particular, the NCSM-in-an-EFT-framework formalism is described in considerable detail in the Stetcu–Rotureau review. Consequently, we will not duplicate that effort, but simply refer the interested reader to their review [82].

5.1. The ab initio shell model with a core method

The basic idea of the *ab initio* Shell Model with a Core [199] is to reintroduce a core into the NCSM approach, by performing a second unitary transformation, so as to include the effects of *all A* nucleons into a single major shell, as proposed by Navrátil, et al. [204]. This procedure adds additional steps to the standard NCSM approach, but continues to preserve all the symmetries of the underlying interactions. The *ab initio* Shell Model with a Core approach [199] uses the well-established *ab initio* NCSM to solve for the core and one- and two-body (and perhaps three-body) terms that are needed for performing Standard Shell Model (SSM) calculations for nuclei in the *sd*- and *pf*-shells. Such SSM calculations can be performed in vastly smaller model spaces than those required for converged NCSM calculations.

Let us outline these additional steps. First, we use the converged A-nucleon eigensolutions, obtained from a standard NCSM calculation, to construct a second unitary transformation matrix, so as to project the *converged* A-nucleon model-space results into a smaller space. This is exactly the same mathematical procedure used in the standard NCSM to obtain the two-body cluster from exact solutions of the two-nucleon problem in a converged model space, except that it is now done for the *exact, i.e.,* converged, solutions of the A-nucleon system, thereby yielding the A-body cluster. In practice, we truncate into the model space, in which all A nucleons occupy the lowest HO configuration allowed by the Pauli exclusion principle, *i.e.,* the $N_{max} = 0$ NCSM space.

Our first calculations have been for 0p-shell nuclei, because exact NCSM calculations can be performed for these nuclei. This will allow us to benchmark our new NCSM-with-a-core results with those for full NCSM calculations. The first step is to perform a standard NCSM calculation to obtain *converged* eigenenergies and eigenfunctions for the $A = 6$ system, *e.g.,* ^{6}Li. The next step is to carry out a second unitary transformation of the results of the full NCSM calculations for ^{6}Li into a smaller model space, *i.e.,* the space of $0\hbar\Omega$ excitations, which is equivalent to a neutron and a proton in the 0p-shell and the other four nucleons *energetically frozen* into the 0*s*-shell. Thus, we obtain *only* two-body matrix elements of the two-nucleons in the 0p-shell, although we started with a full solution of the $A = 6$ system in the NCSM approach. However, these two-body matrix elements contain *all* the correlations of the six-nucleon system. This is equivalent to solving the six-body-cluster problem in the 0p-shell, in this case for ^{6}Li. When diagonalized in the 0p-shell, this six-body-cluster result yields *exactly* the same eigenenergies as the full NCSM calculations for states with parentage predominately within the 0p-shell. Because it is possible to calculate the six-body cluster for one nucleus, *i.e.,* ^{6}Li, it is also possible to determine the six-body cluster for any

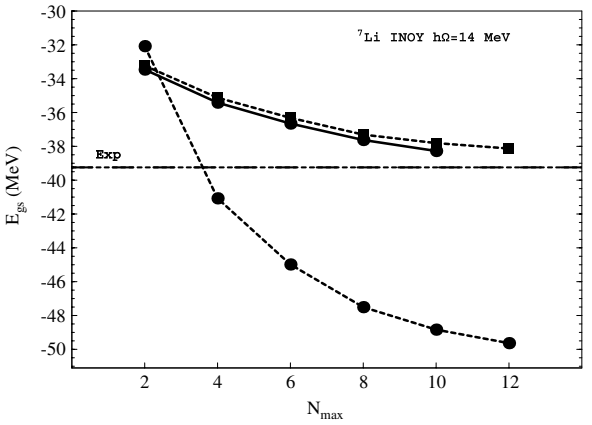

Fig. 29. The g.s. energy of ^{7}Li as a function of N_{max}. The dots connected with a solid line are the full NCSM results. The squares connected with a dashed line are the SSM results without the three-body component. The dots connected with a dashed line are SSM results using a constant, bare ^{4}He g.s. energy. See the text and Ref. [199] for more details.

nucleus with $A \geq 6$, so long as the original NCSM calculations are performed with the two-body-cluster matrix elements for that A-nucleon system. Consequently, all results in this approach are A-dependent.

In a similar manner, we can calculate the seven-body cluster in the 0p-shell by performing a NCSM calculation for ^{7}Li (or for any nucleus with $A \geq 7$) and then carrying out an unitarity transformation of this result into the 0p-shell. Similar to the procedure described for the six-body-cluster calculations, we now obtain three-body matrix elements in the 0p-shell, which contain all the correlations of the seven-nucleon system. This is equivalent to having determined the seven-body cluster for this nucleus.

5.1.1. Applications of the NCSM-with-a-core approach to 0p-shell nuclei

For our test and benchmarking investigations in the 0p-shell [199], we have performed full NCSM calculations for the $A = 6$ and $A = 7$ nuclear systems (with both the INOY [101] and CD-Bonn [10,11] *NN* potentials, as the model-space size, $N_{max}\hbar\Omega$, is varied from $N_{max} = 2$ to 12 with $\hbar\Omega = 14$ MeV). See Fig. 5 (left) for the results for ^{6}Li with the INOY *NN* potential. We then determined the core, one-body and two-body (and three-body for $A = 7$) components, as outlined below. These components, determined as a function of A, can then be used to perform SSM calculations for all nuclei in the 0p-shell, in much smaller model spaces. Effects of neglected four-body interactions, so far, appear to be small. We refer to the two-body and three-body components as the two-body valence (2BVC) and three-body valence (3BVC) components, respectively.

To be specific, let us consider the $A = 6$ system ^{6}Li. After performing the converged NCSM calculations for ^{6}Li (see Fig. 5), we project these converged results, by means of an unitary transformation, into the $N_{max} = 0$ model space. This projection yields two-body matrix elements in the 0p-shell, due to the other four nucleons being *energetically frozen* into the 0*s*-shell, which contain all the correlations of the $A = 6$ system, *i.e.,* they are equivalent to the six-body cluster. We then calculate the energy of the ^{4}He core inside the ^{6}Li nucleus, *i.e.,* the four-body cluster, using the ^{6}Li NCSM two-body-cluster matrix elements. If we use the INOY *NN* potential [101], we compute the ^{4}He g.s. energy to be -54.830 MeV, which is significantly larger than that for a *bare* ^{4}He nucleus, being -28.296 MeV experimentally. This should not be a surprising result, because the two protons and the two neutrons of the ^{4}He core are in lower-lying $0s_{1/2}$ levels inside the ^{6}Li mean field (*e.g.,* a phenomenological Woods–Saxon potential), than in the mean field for a *bare* ^{4}He nucleus. The single-particle energies are then obtained by calculating the five-body clusters inside the ^{6}Li nucleus, *i.e.,* ^{5}He and ^{5}Li, and subtracting the above ^{4}He core energy. The two-body matrix elements are found by subtracting the previous five-body-cluster results from the earlier six-body-cluster results, *e.g.,* ^{6}He, ^{6}Li and ^{6}Be.

Because full NCSM calculations can also be performed for $A = 7$ systems, we can calculate the seven-body cluster for nuclei with $A \geq 7$, in a similar manner, as described above. We, thus, obtain three-body matrix elements in the 0p-shell, which can be separated into a core, one-body, two-body and three-body components for nuclei with $A \geq 7$.

Fig. 29 compares the result of the full NCSM calculation for the g.s. energy of ^{7}Li (solid dots connected with a solid line) with the result of the SSM calculation (solid squares connected with a dashed line), performed using only the core, one-body and two-body components, determined as described above. The third result shown in Fig. 29, *i.e.,* the solid dots connected by a dashed line, is calculated using a *constant, bare* ^{4}He g.s. energy, namely -30.500 MeV for the INOY *NN* potential [101]. This curve clearly illustrates the importance of using the correct ^{4}He core energy, calculated with the ^{7}Li two-body matrix elements, *i.e.,* the ^{4}He core is within the ^{7}Li mean field. If the constant value is used for the ^{4}He core energy, we obtain two-body matrix elements, which become overly attractive and, hence, produce overbinding, with increasing size of the model space, *i.e.,* increasing N_{max}. These results clearly show the importance of calculating the core and one- and two-body terms as functions of A and N_{max}.

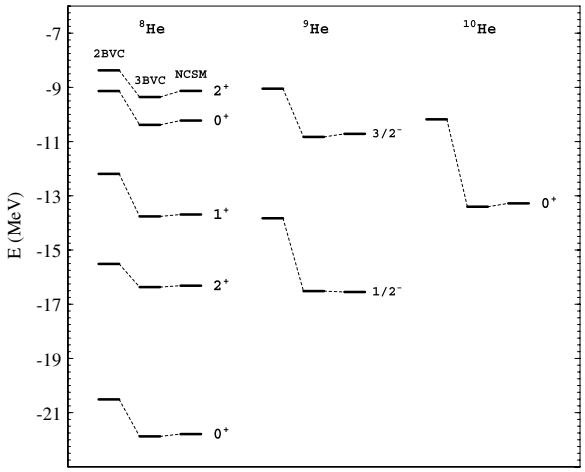

Fig. 30. Comparison of spectra for ^{8}He, ^{9}He and ^{10}He from SSM calculations using up to two-body valence components (2BVC) and up to three-body valence components (3BVC) with exact NCSM results, all calculated for $N_{\max} = 6$ and $\hbar\Omega = 20$ MeV, using the CD-Bonn *NN* potential [10,11].

These core, one-body and two-body components (recalculated as a function of A) can also be used for performing SSM calculations in the 0p-shell for nuclear systems with $A > 7$. For example, Fig. 30 shows results for ^{8}He, ^{9}He and ^{10}He calculated with the CD Bonn *NN* potential [10,11] for $N_{\max} = 6$ and $\hbar\Omega = 20$ MeV. At least for these maximal isospin cases, including the *effective* three-body contribution (3BVC) improves agreement with the exact NCSM results and *appears* to leave very limited room for *effective* four- and/or higher-body contributions for this *NN* potential. For the INOY *NN* potential including the 3BVC causes the results to become worse as A increases (see Ref.[199] for more details on these results).

The *same* approach, outlined previously for obtaining the effective components of the shell-model Hamiltonian in a single major shell, *e.g.,* the 0p-shell, can also be utilized for computing the effective components of any physical operator in the same major shell. See Ref. [152] for details. The results of such calculations for the electric quadrupole moment (Q) of ^{6}Li were shown earlier in Fig. 15. Clearly, the very small Q-moment for ^{6}Li arises from complex many-body correlations among all six nucleons (because Q is a long-range operator), leading to a large cancellation between the one- and two-body contributions.

The above 0p-shell results encourage us to extend this approach to nuclei in the sd-shell, which will require converged results for nuclei with $A = 16$, 17, 18 and 19. To obtain such results we will need a procedure for truncating the size of the basis space necessary to obtain converged NCSM results, such as the Importance Truncation approach discussed in the following subsection.

5.2. Importance truncation

The basic idea of the Importance Truncation (IT) approach is to decrease the size of the model space required in a given NCSM calculation by eliminating configurations based on an *importance criterium*. This approach was pioneered in the NCSM by Roth and Navrátil [195] and is referred to as the IT-NCSM. This initial formulation used a multiparticle–multihole (*e.g.,* $2p$–$2h$, *etc.,*) approach to generate the basis states coming from the next larger $N_{\max}$ space. However, this approach was criticized for possibly having size-extensive issues [205,206]. Thus, an improved version of the IT-NCSM approach was developed [196,200], which includes all basis states in the truncation space, but in a sequential manner, as discussed below. The most complete description of this IT-NCSM method is given in [196].

The IT-NCSM procedure is based on multi-configuration perturbation theory (PT), as originally conceived in quantum chemistry [207–209]. The basic idea centers around a size parameter κ that determines which many-body basis states are kept in a certain $N_{\max}$ model space. One wants to calculate the first-order PT contributions to the total wave function, coming from components in the next larger model space, *i.e.,* $N_{\max} \Rightarrow N_{\max} + 2 \Rightarrow N_{\max} + 4 \Rightarrow$ *etc.*, namely,

$$|\psi^{(1)}_{N_{\max}+2,\mathrm{IT}}\rangle = \sum_{\nu \in N_{\max}+2} \frac{\langle \phi_\nu | W | \Psi_{\mathrm{ref},N_{\max}} \rangle}{\epsilon_\nu - \epsilon_{\mathrm{ref,sp}}} |\phi_\nu\rangle. \tag{43}$$

In Eq. (43) $|\psi^{(1)}_{N_{\max}+2,\mathrm{IT}}\rangle$ denotes the approximate wave function of the full space $N_{\max}+2$ wave function; $|\phi_\nu\rangle$, the $N_{\max}+2$ many-body basis states; $|\Psi_{\mathrm{ref},N_{\max}}\rangle$, the previously calculated reference state in the $N_{\max}$ space; and W, the perturbation operator. The two terms in the denominator refer to the energies of the states ϕ_ν and $\Psi_{\mathrm{ref},N_{\max}}$, respectively. The energy $\epsilon_{\mathrm{ref,sp}}$ is always taken to be the lowest unperturbed energy configuration of the nucleus. For example, in the case of ^{6}Li, this would correspond to taking $\epsilon_{\mathrm{ref,sp}} = 2\hbar\Omega$, because there are two valence nucleons in the $N = 1$ shell. We neglect the zero-point motion of the HO, *i.e.,* $(3/2)\hbar\Omega$, since we only require the difference in energy of the s.p. energies. Furthermore, for ^{6}Li $\epsilon_\nu = (6+2)\hbar\Omega$ for the basis states in $N_{\max} = 4$. It is convenient to define the W as $W = H - H_0$, where H is the initial Hamiltonian and H_0 is that part of H, which connects only many-body basis states that lie in the initial basis space,

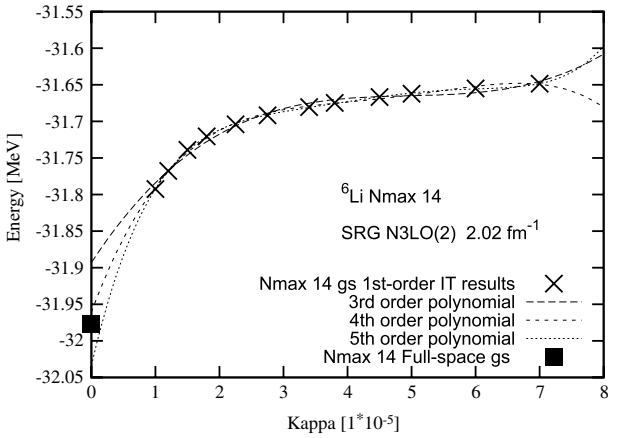

Fig. 31. The IT calculated g.s. energies of ^{6}Li, in an $N_{\max} = 14$ space, using the SRG-N3LO potential with a momentum-cutoff $\lambda = 2.02$ fm^{-1} [128]. The oscillator energy is $\hbar\Omega = 16$ MeV. The fit shows three different polynomial extrapolations to $E_{0,\kappa=0}$. Note that the extrapolated values are different and are spread across a range of about 150 keV. For comparison, we have included the g.s. energy of a complete $N_{\max} = 14$ space.

i.e., from 0 up to $N_{\max}$. Thus, H_0 does not connect basis states from the reference space to the $N_{\max} + 2$ space. Consequently, we can rewrite Eq. (43) in the form

$$|\psi^{(1)}_{N_{\max}+2,\mathrm{IT}}\rangle = \sum_{\nu\in N_{\max}+2} \frac{\langle\phi_\nu|H|\Psi_{\mathrm{ref},N_{\max}}\rangle}{\epsilon_\nu - \epsilon_{\mathrm{ref,sp}}}|\phi_\nu\rangle, \tag{44}$$

so that the *importance measure*, κ_ν, of a basis state (ϕ_ν) can be defined as

$$\kappa_\nu = \frac{|\langle\phi_\nu|H|\Psi_{\mathrm{ref},N_{\max}}\rangle|}{\epsilon_\nu - \epsilon_{\mathrm{ref,sp}}}. \tag{45}$$

The importance measure κ_ν can now be used to set a threshold limit, on which basis states are included in the truncated $N_{\max} + 2$ space. If the threshold value for κ_ν is taken to be a few 10^{-5}, say $2 * 10^{-5}$, then only basis states (ϕ_ν) in the $N_{\max} + 2$ space with $\kappa_\nu \geq 2 * 10^{-5}$ are kept. Basis states (ϕ_ν) with κ_ν lower than this threshold will be discarded, starting the truncation of the $N_{\max} + 2$ space. Once the truncated $N_{\max} + 2$ basis has been formed, it can be used to diagonalize the Hamiltonian H in this truncated space. This yields a new g.s. wave function, $|\Psi^{(N_{\max}+2)}_{\mathrm{ref}}\rangle$, which is then used as the reference state for evaluating all the basis states in the $N_{\max} + 4$ basis space, using the same method as described above, and so on.

This sequential method has the advantage that it automatically generates all basis states in the evaluated $N_{\max}$ space, so it only needs to be done once per basis space. Furthermore, one can generate a sequence of g.s. energies for each truncated $N_{\max}$ basis space, which can be easily extrapolated to obtain the g.s. energy at $N_{\max} = \infty$.

In practice, the calculations must be done for several values of κ_ν, because it is not possible, by definition, to do the calculations for $\kappa_\nu = 0$. This would be equivalent to performing the NCSM calculation in the full $N_{\max} + 2$ space. If we could do this, then there would be no need to truncate the $N_{\max} + 2$ space. Thus, we need results for several values of κ_ν, which will guide us in constructing extrapolation procedures for going to the limit $\kappa_\nu \to 0$. One can also determine excited states in a similar manner, but Eq. (43) would contain a $\Psi_{\mathrm{ref},N_{\max}}$ for the excited state, leading to a new value of κ_ν.

Our research group is currently investigating refinements of this method, for which preliminary results in the 0p-shell are yielding encouraging results [200]. Fig. 31 shows IT-NCSM results for the g.s. energy of ^{6}Li by Kruse [200]. One starts with the results of a NCSM calculation in the full $N_{\max} = 4$ space. The *new* configurations that come from adding the $N_{\max} = 6$ space, that is, states above the $N_{\max} = 4$ space, are truncated according to whether their first-order PT contribution is larger (kept) or smaller (rejected) than κ. After completing the calculation for the configurations coming from going to $N_{\max} = 6$, one repeats this same procedure for the $N_{\max} = 8$ space, *etc.* The results from adding configurations from the $N_{\max} = 6$ up to the $N_{\max} = 14$ spaces are shown in Fig. 31 as a function of decreasing κ. Note that in these calculations *all* of the configurations up to the $N_{\max} = 4$ space are kept and are *never* truncated. As a test we do not let κ go to zero, because this would include the entire model space, which, in general, would not be possible, due to its extremely large dimension. In this way we can investigate different extrapolation methods for approaching $\kappa = 0$. In Fig. 31 we show extrapolations to $\kappa = 0$ by making a polynomial fit, for polynomials of order 3, 4 and 5. The spread in the results for these different polynomial fits, roughly 150 keV, provides an estimate of the error in the extrapolated results. More detailed extrapolations, as given in Ref. [200], typically yield a calculated spread that is smaller than 100 keV.

One can also improve the estimates for the g.s. energy by including the second-order PT correction to the energy. Physically, both the first- and second-order curves for the g.s. energy should meet in the limit $\kappa \to 0$. Thus, doing a constrained fit on the two curves could: (1) lower the spread between various fitting functions and (2) bring one closer

to the true NCSM result. Various extrapolation techniques as well as two different implementations of the IT-NCSM are currently under investigation with the goal of providing much greater uncertainty quantification [210].

It should be noted that this IT-NCSM approach is also beneficial for obtaining wave functions for use in nuclear-reaction calculations using the NCSM and the Resonating Group Method [211].

6. Applications to nuclear reactions

Nuclei are quantum systems with bound states, unbound resonances, and scattering states. A realistic *ab initio* description of light nuclei with predictive power must have the capability to describe all bound and unbound states within a unified framework. Over the past decade, significant progress has been made in our understanding of the properties of the bound states of light nuclei starting from realistic *NN* and *NNN* interactions. This progress was also in part due to the development of the *ab initio* NCSM, as described in the previous sections of this article. Although techniques, such as the *ab initio* NCSM, have greatly advanced our understanding of nuclear structure, the solution of the nuclear many-body problem is even more complex, when scattering or nuclear reactions are considered. *Ab initio* calculations for scattering processes involving more than four nucleons overall are challenging and still a rare exception [212]. Even calculations of resonant states are quite complicated [213].

The development of an *ab initio* theory of low-energy nuclear reactions on light nuclei is key to further refining our understanding of the fundamental nuclear interactions among the constituent nucleons. Also, it would greatly help our understanding of nuclear reactions important for astrophysics. Some of the outstanding light-nucleus uncertainty sources in astrophysics applications include: reactions leading to the nucleosynthesis of ^{8}B (and the production of the solar neutrinos measured in terrestrial experiments); the thermonuclear reaction rates of α capture on ^{8}Be and ^{12}C nuclei during the stellar helium burning; and fusion reactions that affect the predictions of Big Bang nucleosynthesis for the abundances of light elements.

Furthermore, nuclear reactions are one of the best tools for studying exotic nuclei, which have become the focus of the next generation experiments with rare-isotope beams. These are nuclei, for which most low-lying states are unbound, so that a rigorous analysis requires scattering boundary conditions. In addition, much of the information we have on the structure of these short-lived systems is inferred from reactions with other nuclei.

Finally, low-energy fusion reactions represent the primary energy-generation mechanism in stars, and could potentially be used for future energy generation on earth. Examples of these latter reactions include the $d+{}^3\mathrm{H} \rightarrow n+{}^4\mathrm{He}$ fusion used at ITER [214] and at the National Ignition Facility (NIF) [215]. Even though there have been many experimental investigations of the cross sections of this reaction, there are still open issues. At the same time, large uncertainties in reactions such as the ${}^3\mathrm{H} + d \rightarrow {}^4\mathrm{He} + n + \gamma$ bremsstrahlung process or the ${}^3\mathrm{H}({}^3\mathrm{H}, 2n){}^4\mathrm{He}$ fusion are limiting factors in the understanding of how the fuel is assembled in deuterium–tritium based fusion experiments.

6.1. Coupling of the no core shell model with the resonating group method

A fully *ab initio* approach to nuclear reactions based on the NCSM requires a more precise treatment of the wave-function asymptotics and the coupling to the continuum. Therefore, we have developed a new approach, the *ab initio* NCSM/RGM [216–218], capable of simultaneously describing both bound and scattering states in light nuclei, by combining the resonating-group method (RGM) [219] with the *ab initio* NCSM. The RGM is a microscopic cluster technique based on the use of A-nucleon Hamiltonians, with fully anti-symmetric many-body wave functions built assuming that the nucleons are grouped into clusters. By combining the NCSM with the RGM, we complement the ability of the RGM to deal with scattering and reactions with the utilization of realistic interactions and a consistent microscopic description of the nucleonic clusters achieved via *ab initio* NCSM, while preserving important symmetries, including the Pauli exclusion principle and translational invariance.

The innovation, which allows us to go beyond bound states and treat reactions, is the use of cluster basis states in the spirit of the resonating-group method,

$$|\Phi^{J^\pi T}_{\nu r}\rangle = \left[\left(\left|A-a\,\alpha_1 I_1^{\pi_1} T_1\right\rangle \left|a\,\alpha_2 I_2^{\pi_2} T_2\right|\right)^{(sT)} Y_\ell\left(\hat{r}_{A-a,a}\right)\right]^{(J^\pi T)} \frac{\delta(r-r_{A-a,a})}{r r_{A-a,a}}, \tag{46}$$

in which each nucleon cluster is described within the NCSM. The above translational invariant cluster basis states describe two nuclei (a target and a projectile composed of $A-a$ and a nucleons, respectively) whose centers of mass are separated by the relative coordinate $\vec{r}_{A-a,a}$ and that are traveling in a ${}^{2s}\ell_J$ wave or relative motion (with s the channel spin, ℓ the relative momentum, and J the total angular momentum of the system). Additional quantum numbers characterizing the basis states are parity $\pi = \pi_1\pi_2(-1)^\ell$ and total isospin T. For the intrinsic (antisymmetric) wave functions of the two nuclei we employ the eigenstates $\left|A-a\,\alpha_1 I_1^{\pi_1} T_1\right\rangle$ and $\left|a\,\alpha_2 I_2^{\pi_2} T_2\right\rangle$ of the $(A-a)$- and a-nucleon intrinsic Hamiltonians, respectively, as obtained within the NCSM approach. These are characterized by the spin-parity, isospin and energy labels $I_i^{\pi_i}$, T_i, and α_i, respectively, where $i = 1, 2$. In our notation, all these quantum numbers are grouped into a cumulative index $\nu = \{A-a\,\alpha_1 I_1^{\pi_1} T_1;\ a\,\alpha_2 I_2^{\pi_2} T_2;\ s\ell\}$. Finally, we note that the channel states (46) are not antisymmetric with respect to exchanges of nucleons pertaining to different clusters. Therefore, to preserve the Pauli principle one has to introduce the appropriate inter-cluster antisymmetrizer, schematically

$$\hat{\mathcal{A}}_\nu = \sqrt{\frac{(A-a)!a!}{A!}}\left(1+\sum_{P\neq id}(-)^p P\right), \tag{47}$$

where the sum runs over all possible permutations of nucleons P different from the identical one that can be carried out between two different clusters (of $A-a$ and a nucleons, respectively), and p is the number of interchanges characterizing them. The operator (47) is labeled by the channel index ν to signify that its form depends on the mass partition, $(A-a, a)$, of the channel state to which is applied.

The channel states (46), fully antisymmetrized by the action of the antisymmetrization operator $\hat{A}_\nu$, are used as a continuous basis set to expand the many-body wave function,

$$|\Psi^{J^\pi T}\rangle = \sum_\nu \int dr r^2\, \hat{\mathcal{A}}_\nu |\Phi^{J^\pi T}_{\nu r}\rangle \frac{[\mathcal{N}^{-1/2}\chi]^{J^\pi T}_\nu(r)}{r}, \tag{48}$$

where $\chi^{J^\pi T}_\nu(r)$ represent continuous linear variational amplitudes that are determined by solving the orthogonalized RGM equations:

$$\sum_{\nu'}\int dr' r'^2 [\mathcal{N}^{-\frac{1}{2}}\mathcal{H}\,\mathcal{N}^{-\frac{1}{2}}]^{J^\pi T}_{\nu\nu'}(r,r')\frac{\chi^{J^\pi T}_{\nu'}(r')}{r'} = E\,\frac{\chi^{J^\pi T}_\nu(r)}{r}. \tag{49}$$

Here $\mathcal{N}^{J^\pi T}_{\nu\nu'}(r,r')$ and $\mathcal{H}^{J^\pi T}_{\nu\nu'}(r,r')$, commonly referred to as integration kernels, are, respectively, the overlap (or norm) and Hamiltonian matrix elements over the antisymmetrized basis (46), *i.e.*:

$$\mathcal{N}^{J^\pi T}_{\nu'\nu}(r',r) = \left\langle \Phi^{J^\pi T}_{\nu' r'}\middle|\, \hat{\mathcal{A}}_{\nu'}\hat{\mathcal{A}}_\nu \,\middle|\Phi^{J^\pi T}_{\nu r}\right\rangle, \qquad \mathcal{H}^{J^\pi T}_{\nu'\nu}(r',r) = \left\langle \Phi^{J^\pi T}_{\nu' r'}\middle|\, \hat{\mathcal{A}}_{\nu'} H \hat{\mathcal{A}}_\nu \,\middle|\Phi^{J^\pi T}_{\nu r}\right\rangle, \tag{50}$$

where H is the microscopic $A-$nucleon Hamiltonian and E is the total energy in the center-of-mass (c.m.) frame. The calculation of the above many-body matrix elements, which contain all the nuclear structure and antisymmetrization properties of the system under consideration, represents the main task in performing RGM calculations.

Input into these calculations is the microscopic Hamiltonian given in Eq. (1) typically transformed by the SRG technique, described in Section 3.4. For the purpose of the RGM approach, it is convenient to separate Eq. (1) into the intrinsic Hamiltonians for the $(A-a)$- and a-nucleon systems, respectively, $H_{(A-a)}$ and $H_{(a)}$, plus the relative-motion Hamiltonian, according to:

$$H = T_{\rm rel}(r) + \bar{V}_{\rm C}(r) + \mathcal{V}_{\rm rel} + H_{(A-a)} + H_{(a)}. \tag{51}$$

Here, $T_{\rm rel}(r)$ is the relative kinetic energy, $\bar{V}_{\rm C}(r) = Z_{1\nu}Z_{2\nu}e^2/r$ ($Z_{1\nu}$ and $Z_{2\nu}$ being the charge numbers of the clusters in channel ν) is the average Coulomb interaction between pairs of clusters, and $\mathcal{V}_{\rm rel}$ is the localized relative (inter-cluster) potential, given by:

$$\mathcal{V}_{\rm rel} = \sum_{i=1}^{A-a}\sum_{j=A-a+1}^{A} V^{NN}_{ij} + \sum_{i<j=1}^{A-a}\sum_{k=A-a+1}^{A} V^{NNN}_{ijk} + \sum_{i=1}^{A-a}\sum_{j<k=A-a+1}^{A} V^{NNN}_{ijk} - \bar{V}_{\rm C}(r). \tag{52}$$

Besides the nuclear components of the interactions between nucleons belonging to different clusters, it is important to notice that the overall contribution to the relative potential (52) coming from the Coulomb interaction,

$$\sum_{i=1}^{A-a}\sum_{j=A-a+1}^{A}\left(\frac{e^2(1+\tau_i^z)(1+\tau_j^z)}{4|\vec{r}_i-\vec{r}_j|} - \frac{1}{(A-a)a}\bar{V}_{\rm C}(r)\right), \tag{53}$$

is also localized, presenting an r^{-2} behavior, as the distance r between the two clusters increases.

The other main input required for calculating the RGM integration kernels of Eq. (50) are the eigenstates of the projectile and target wave functions. In the NCSM/RGM approach, these are obtained by diagonalizing $H_{(A-a)}$ and $H_{(a)}$ in the model spaces spanned by the $(A-a)$- and a-nucleon NCSM bases, respectively. We adopt complete HO bases, the size of which is defined by the maximum number, $N_{\rm max}$, of HO quanta above the lowest configuration shared by the nucleons (the definition of the model-space size coincides for eigenstates of the same parity, differs by one unity for eigenstates of opposite parity). The same $N_{\rm max}$ value and HO frequency Ω are used for both clusters.

To calculate the integration kernels, we make use of their factorization into "full-space" and "model-space" components according to:

$$\mathcal{N}^{J^\pi T}_{\nu'\nu}(r',r) = \delta_{\nu'\nu}\frac{\delta(r'-r)}{r'r} + \mathcal{N}^{\rm ex}_{\nu'\nu}(r',r) \tag{54}$$

and

$$\mathcal{H}^{J^\pi T}_{\nu'\nu}(r',r) = \left[T_{\rm rel}(r') + \bar{V}_C(r') + E^{I'_1T'_1}_{\alpha'_1} + E^{I'_2T'_2}_{\alpha'_2}\right]\mathcal{N}^{J^\pi T}_{\nu'\nu}(r',r) + \mathcal{V}^{J^\pi T}_{\nu'\nu}(r',r), \tag{55}$$

where the exchange part of the norm, $\mathcal{N}^{\rm ex}_{\nu'\nu}(r',r)$, and the potential kernel, $\mathcal{V}^{J^\pi T}_{\nu'\nu}(r',r)$, are obtained in the truncated model space by expanding the Dirac delta function of Eq. (46) on a set of HO radial wave functions with identical frequency Ω and model-space size $N_{\rm max}$ as those used for the two clusters.

Being translationally-invariant quantities, the norm and Hamiltonian kernels can be "naturally" derived, working within the NCSM Jacobi-coordinate basis. However, by introducing Slater-determinant channel states of the type

$$|\Phi^{J^\pi T}_{\nu n}\rangle_{\rm SD} = \left[\left(|A-a\,\alpha_1 I_1 T_1\rangle_{\rm SD}\,|a\,\alpha_2 I_2 T_2\rangle\right)^{(sT)} Y_\ell(\hat{R}^{(a)}_{\rm c.m.})\right]^{(J^\pi T)} R_{n\ell}(R^{(a)}_{\rm c.m.}), \tag{56}$$

in which the eigenstates of the $(A-a)$-nucleon fragment are obtained in the SD basis (while the second cluster is still a NCSM Jacobi-coordinate eigenstate), it can be easily demonstrated that translationally invariant matrix elements can be extracted from those calculated in the SD basis of Eq. (56) by inverting the following expression:

$$\begin{aligned}{}_{\rm SD}\left\langle \Phi^{J^\pi T}_{\nu' n'}\right|\hat{\mathcal{O}}_{\rm t.i.}\left|\Phi^{J^\pi T}_{\nu n}\right\rangle_{\rm SD} = \sum_{n'_r\ell'_r,n_r\ell_r,J_r}\left\langle \Phi^{J^{\pi_r}_r T}_{\nu'_r n'_r}\right|\hat{\mathcal{O}}_{\rm t.i.}\left|\Phi^{J^{\pi_r}_r T}_{\nu_r n_r}\right\rangle \sum_{NL}\hat{\ell}\hat{\ell}'\hat{J}_r^2(-1)^{(s+\ell-s'-\ell')}\begin{Bmatrix} s & \ell_r & J_r\\ L & J & \ell\end{Bmatrix}\begin{Bmatrix} s' & \ell'_r & J_r\\ L & J & \ell'\end{Bmatrix}\\ \times\langle n_r\ell_r NL\ell|00n\ell\ell\rangle_{\frac{a}{A-a}}\;\langle n'_r\ell'_r NL\ell|00n'\ell'\ell'\rangle_{\frac{a}{A-a}}.\end{aligned} \tag{57}$$

Here $\hat{\mathcal{O}}_{\rm t.i.}$ represents any scalar and parity-conserving translational-invariant operator ($\hat{\mathcal{O}}_{\rm t.i.} = \hat{\mathcal{A}}$, $\hat{\mathcal{A}}H\hat{\mathcal{A}}$, *etc.*). For further details, see Ref. [217]. We exploited both Jacobi-coordinate and SD channel states to verify our results. The use of the SD basis is computationally advantageous and allows us to explore reactions involving p-shell nuclei and beyond.

The output of the NCSM/RGM calculations are the eigenstates and eigenenergies for bound states and scattering matrix and eigenstates for unbound states. Due to the Pauli exclusion principle, the integration kernels are surfaces in three dimensions, and give rise to channel-dependent non-local couplings $W^{J^\pi T}_{\nu\nu'}(r,r')$ between the unknown projectile–target relative wave functions. Indeed, by separating local diagonal and non-local terms, Eq. (49) can be cast in the form:

$$[\hat{T}_{\rm rel}(r)+\bar{V}_{\rm C}(r)-(E-E^{I^{\pi_1}_1 T_1}_{\alpha_1}-E^{I^{\pi_2}_2 T_2}_{\alpha_2})]\frac{\chi^{J^\pi T}_\nu(r)}{r}+\sum_{\nu'}\int dr'\,r'^2\,W^{J^\pi T}_{\nu\nu'}(r,r')\,\frac{\chi^{J^\pi T}_{\nu'}(r')}{r'}=0. \tag{58}$$

The solution of such a set of integral–differential coupled channel equations represents a fairly standard problem in scattering theory, only slightly complicated by the presence of non-local coupling potentials. A particularly efficient technique for the solution of Eq. (58) is the *R*-matrix method on Lagrange mesh [220,221]. This is a method based on the microscopic *R*-matrix theory [222,223] in which one assumes that $\bar{V}_{\rm C}(r)$ is the only interaction experienced by the clusters beyond a sufficiently large separation r_0, thus dividing the configuration space into an internal and an external region. In the internal region, the wave function can be written as an expansion over a set of square integrable basis functions, while in the external region it can be approximated by its asymptotic form for large r,

$$\chi^{J^\pi T}_\nu(r)=\frac{\rm i}{2}v_\nu^{-1/2}[\delta_{\nu i}H^-_\ell(\eta_\nu,\kappa_\nu r)-S^{J^\pi T}_{\nu i}H^+_\ell(\eta_\nu,\kappa_\nu r)], \tag{59}$$

for scattering states, or

$$\chi^{J^\pi T}_\nu(r)=C^{J^\pi T}_\nu\,W_\ell(\eta_\nu,\kappa_\nu r), \tag{60}$$

for bound states. Here, $H^\mp_\ell(\eta_\nu,\kappa_\nu r)=G_\ell(\eta_\nu,\kappa_\nu r)\mp {\rm i}F_\ell(\eta_\nu,\kappa_\nu r)$ are incoming and outgoing Coulomb functions, whereas $W_\ell(\eta_\nu,\kappa_\nu r)$ are Whittaker functions. They depend on the channel-state relative angular momentum ℓ, wave number κ_ν, and Sommerfeld parameter η_ν. The corresponding velocity is denoted as v_ν. The scattering matrix $S^{J^\pi T}_{\nu i}$ (i being the initial channel) in Eq. (59) is obtained by requiring the continuity of the wave function $\chi^{J^\pi T}_\nu(r)$ and of its first derivative at the matching radius r_0. The matrix elements of the scattering matrix can then be used to calculate cross sections and other reaction observables. For bound-state calculations κ_ν depends on the studied binding energy. Therefore, the determination of the bound-state energy and asymptotic normalization constant $C^{J^\pi T}_\nu$ in Eq. (60) is achieved iteratively starting from an initial guess for the value of the logarithmic derivative of the wave function at the matching radius r_0.

In the *R*-matrix method on Lagrange mesh, the square-integrable functions chosen to expand the wave function in the internal region are Lagrange functions [221]. This choice greatly simplifies the calculation, particularly in the presence of non-local potentials. The accuracy of the *R*-matrix method on a Lagrange mesh is such that for a matching radius of $r_0 = 15$ fm, $N = 25$ mesh points are usually enough to determine a phase shift within the sixth significant digit. The typical matching radius and number of mesh points adopted for the calculations presented in the following section are $r_0 = 18$ fm and $N = 40$.

6.1.1. *Nucleon-*^{4}He *scattering*

The simplest system to be described in terms of binary-cluster basis states of the type described in Eq. (46) is the scattering of nucleons on ^{4}He targets. Here, energy arguments suggest that channel states already formed by a nucleon in relative motion with respect to an ^{4}He nucleus in its g.s. should provide a very good description of this process up to fairly high energies. Indeed, the ^{4}He nucleus is tightly bound and its first excited state is more than 20 MeV above its ground state. At the same time, well-determined scattering amplitudes from R-matrix fits make *n*- and *p*-^{4}He scattering calculations ideal benchmarks for our *ab initio* reaction approach.

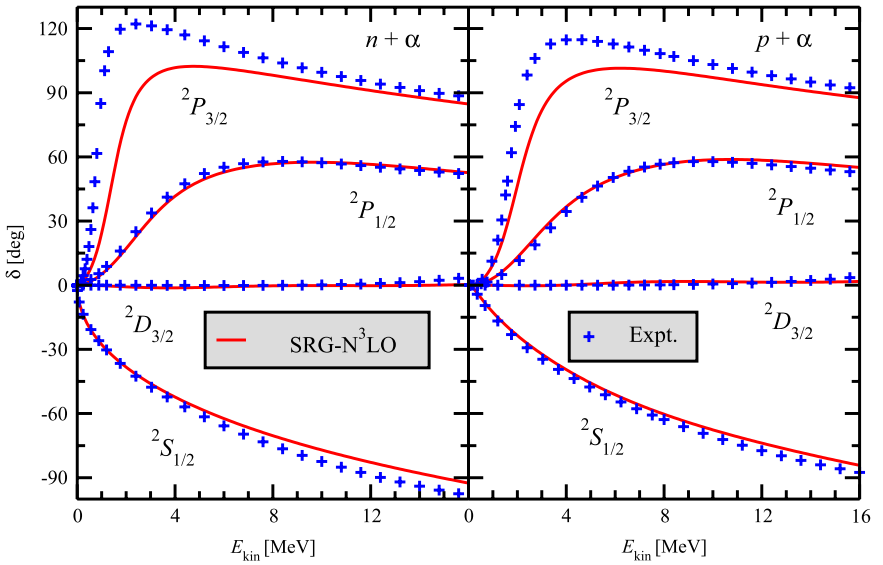

Fig. 32. Calculated $n-^4$He (left panels) and $p-^4$He (right panels) compared to the R-matrix analysis of experimental data [224]. The NCSM/RGM calculations that included the ^{4}He g.s. and the 0^+0 excited state were done using the SRG-N^{3}LO *NN* potential of Ref. [225] with a cutoff of 2.02 fm^{-1}. The HO frequency $\hbar\Omega = 20$ MeV and $N_{max} = 17$ basis space were employed.

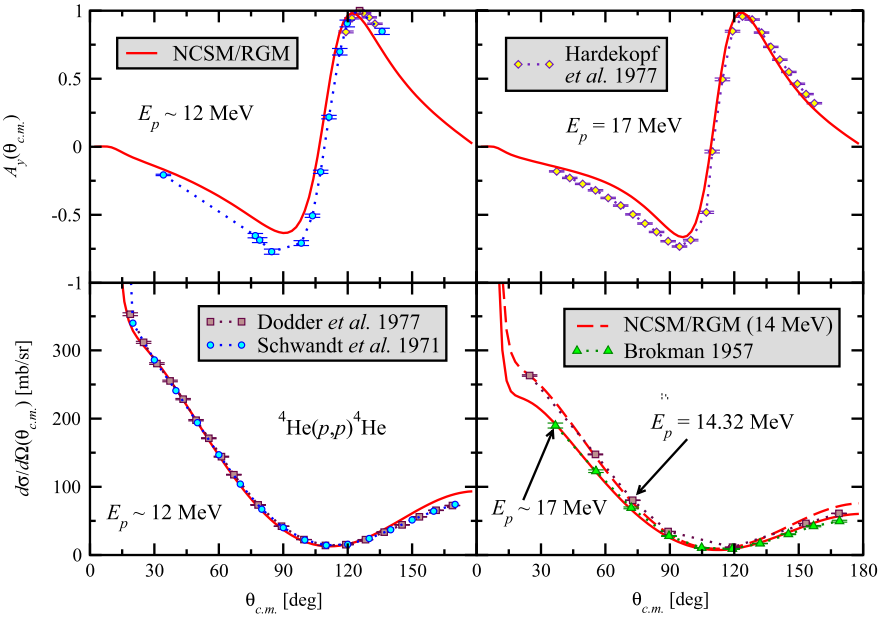

Fig. 33. Calculated p-^{4}He differential cross section (bottom panels) and analyzing power (top panels) for proton laboratory energies $E_p = 12$, 14.32 and 17 MeV compared to experimental data from Refs. [226–229]. The SRG-N^{3}LO NN potential with $\lambda = 2.02$ fm^{-1} was used.

We performed nucleon-^{4}He calculations with the SRG-N^{3}LO *NN* potential with $\lambda = 2.02$ fm^{-1} in a $N_{max} = 17$ NCSM/RGM model space, spanned by N-^{4}He (g.s.) and N-^{4}He$^*(0_2^+)$ channel states. At $N_{max} = 17$ (16, for the positive parity states) convergence of the HO expansion for the localized parts of the NCSM/RGM integration kernels and for the ^{4}He ground- and the first-excited 0^+0 states has been fully reached with this soft *NN* interaction.

As expected, the agreement (shown in Fig. 32) of our calculated n-^{4}He and p-^{4}He phase shifts with those obtained from an accurate *R*-matrix analysis of the data is quite reasonable, particularly for c.m. energies above ~8 MeV. Correspondingly, in that energy range we can reproduce fairly well also cross-section and polarization data. As an example, Fig. 33 compares NCSM/RGM $p-^4$He results to the experimental data sets [226–229] at $E_p = 17$ and $E_p = 12$ MeV nucleon laboratory energies, respectively. The discrepancies observed in the $^2P_{3/2}$ channel, where the calculated resonance is positioned at higher energy and the phase shifts are underestimated with respect to experiment, are largely due to a reduction in spin–orbit strength

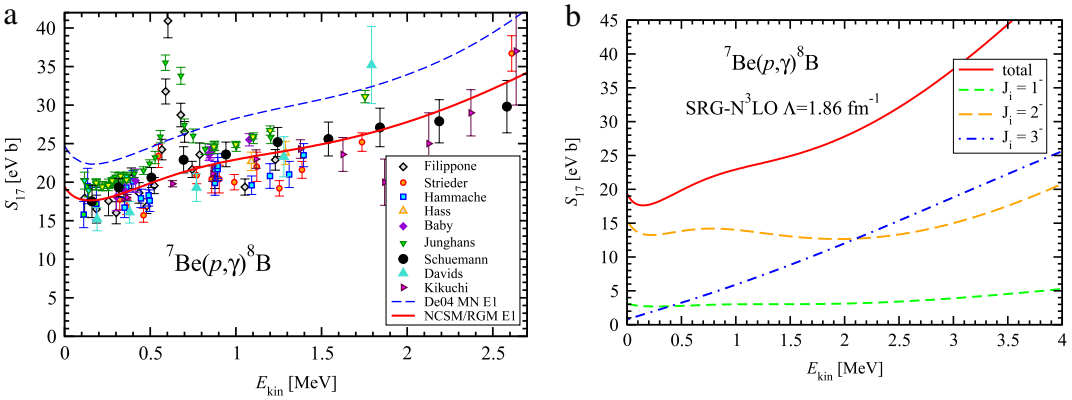

Fig. 34. Calculated ^{7}Be$(p,\gamma)^8$B S-factor as a function of the energy in the c.m. compared to data and the microscopic cluster-model calculations of Ref. [232] with the Minnesota (MN) interaction (*a*). Only $E1$ transitions were considered. Initial-state partial wave contributions are shown in panel (*b*). Calculation is as described in the text.

caused by the omission in our calculation of the *NNN* interaction (chiral and SRG-induced). Efforts to include the *NNN* force into the NCSM/RGM formalism are currently under way with first preliminary results confirming an increase of the splitting of the $^2P_{3/2}$ and $^2P_{1/2}$ phase shifts, when the *NNN* is included in the Hamiltonian. More details on these calculations can be found in Ref. [211].

6.1.2. *The* ^{7}Be$(p,\gamma)^8$B *radiative capture*

The ^{7}Be$(p,\gamma)^8$B capture reaction plays a very important role in nuclear astrophysics, as it serves as an input for understanding the solar neutrino flux [230]. The extrapolation of the S-factor (*i.e.*, the cross section divided by the Gamow factor) to astrophysically relevant energies relies on nuclear theory. Recently, we have performed the first *ab initio* many-body calculation [231], of this reaction starting from the SRG-N^{3}LO *NN* interaction with $\lambda = 1.86$ fm^{-1}. Using p-^{7}Be channel states, including the five lowest $N_{\max} = 10$ eigenstates of ^{7}Be (the $\frac{3}{2}^-$ ground and the $\frac{1}{2}^-$, $\frac{7}{2}^-$, and first and second $\frac{5}{2}^-$ excited states), we solved Eq. (49) first with bound-state boundary conditions to find the bound state of ^{8}B, and then with scattering boundary conditions to find the p-^{7}Be scattering wave functions. Former and latter wave functions were later used to calculate the capture cross section, which, at solar energies, is dominated by non-resonant $E1$ transitions from p-^{7}Be S- and D-waves into the weakly-bound ground state of ^{8}B. All stages of the calculation were based on the same HO frequency of $\hbar\Omega = 18$ MeV, which minimizes the g.s. energy of ^{7}Be. The largest model space achievable for the present calculation within the full NCSM basis is $N_{\max} = 10$. At this basis size, the ^{7}Be g.s. energy is very close to convergence, as indicated by a fairly flat frequency dependence in the range $16 \leq \hbar\Omega \leq 20$ MeV, and the vicinity to the $N_{\max} = 12$ result, obtained within the importance-truncated NCSM [195,196]. The choice of $\lambda = 1.86$ fm^{-1} in the SRG evolution of the N^{3}LO *NN* interaction leads to a single 2^+ bound state for ^{8}B with a separation energy of 136 keV quite close to the observed one (137 keV [160]). This is very important for the description of the low-energy behavior of the ^{7}Be$(p,\gamma)^8$B astrophysical S-factor, known as S_{17}. We note that the *NNN* interaction induced by the SRG evolution of the *NN* potential is repulsive in the λ-range $\sim 1.8 - 2.1$fm^{-1}, and, in very light nuclei, its contributions are canceled to a good extent by those of the initial attractive chiral *NNN* force (which is also SRG evolved) [128,129].

The resulting S_{17} astrophysical factor is compared to several experimental data sets in Fig. 34. Energy dependence and absolute magnitude follow closely the trend of the indirect Coulomb breakup measurements of Shümann et al. [233,234], while somewhat underestimating the direct data of Junghans et al. [235]. The resonance, particularly evident in these and Filippone's data, is due to the $M1$ capture, which does not contribute to a theoretical calculation outside of the narrow ^{8}B 1^+ resonance and is negligible at astrophysical energies [230,236]. The $M1$ operator, for which any dependence upon two-body currents needs to be included explicitly, poses more uncertainties than Siegert's $E1$ operator. We plan to calculate its contribution in the future. The shape is also quite similar to that obtained within the microscopic three-cluster model [232] (see the dashed line in Fig. 34(a)) used, after scaling to the data, in the most recent S_{17} evaluation [236]. The contributions from the initial 1^-, 2^- and 3^- partial waves are shown in panel (b) of Fig. 34.

The convergence of our results with respect to the size of the HO model space was assessed by means of calculations up to $N_{\max} = 12$ within the importance-truncation NCSM scheme [195,196] with (due to computational limitations) only the first three eigenstates of ^{7}Be. The $N_{\max} = 10$ and 12 S-factors are very close. As for the convergence in the number of ^{7}Be states, we explored it by means of calculations including up to 8 ^{7}Be eigenstates in a $N_{\max} = 8$ basis (larger $N_{\max}$ values are currently out of reach with more then five ^{7}Be states). Based on this analysis, we conclude that the use of an $N_{\max} = 10$ HO model space is justified and the limitation to five ^{7}Be eigenstates is quite reasonable. Finally, our calculated $S_{17}(0) = 19.4(7)$ MeV b is on the lower side, but consistent with the latest evaluation 20.8 ± 0.7(expt)± 1.4(theory) [236].

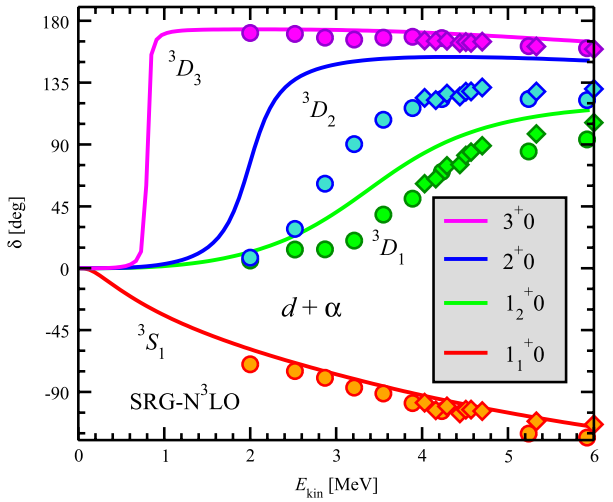

Fig. 35. Calculated d-^{4}He S- and D-wave phase shifts compared to experimental data from Refs. [237] (circles) and [238] (diamonds). Up to 7 deuteron pseudo-states were included in each of the $^3S_1$-$^3D_1$ and $^3D_3$-$^3G_3$ channels and 5 pseudo-states in the $^3D_2$ channel. Calculation as described in the text and in Ref. [218].

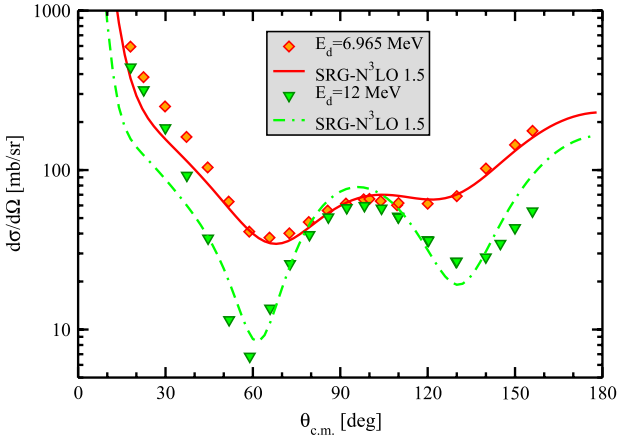

Fig. 36. The d-^{4}He differential cross section at the deuteron laboratory energies of 6.965 and 12 MeV. The experimental data (symbols) are from Refs. [239,240]. The calculations (lines) are as described in Fig. 35. Partial waves up to $J = 6$ were included. Additional details are given in Ref. [218].

6.1.3. *Deuteron-*^{4}He *scattering*

In Ref. [218], we generalized the NCSM/RGM formalism from a single-nucleon projectile to the simplest composite projectile, the deuteron. The NCSM/RGM equations were solved for both bound and scattering states. A soft SRG-N^{3}LO *NN* potential with $\lambda = 1.5$ fm^{-1} was used. The calculations demonstrated the importance of including the polarization and virtual breakup of the weakly bound deuteron in both the bound state and the scattering state calculations. These effects were taken into account by excited deuteron pseudo states in several channels. In particular, the pseudostates in $^3S_1$-$^3D_1$ and $^3D_2$ and $^3D_3$-$^3G_3$ channels proved to be essential. The calculations were performed in the basis up to $N_{\max} = 12$, sufficient for convergence with the used soft *NN* potential.

Our calculated diagonal S- and D-wave phase shifts are compared to the phase shifts extracted from experimental data in Refs. [237,238] in Fig. 35. The calculation corresponds to the largest basis space ($N_{\text{amx}} = 12$) and the highest number of deuteron pseudo-states that we employed in this work (up to seven). Our S-wave and $^3D_3$-wave results compare well with the experimental data. However, the $^3D_1$ and, in particular, the $^3D_2$ phase shifts overestimate the experimental ones. The position of our calculated 2^+0 resonance is below the experimental one by almost 1 MeV. The splitting between the D-waves is underestimated. Clearly, the strength of the spin–orbit interaction in the calculation is smaller than it should be. This is most likely due to the neglect of the *NNN* forces in our calculations, those induced by the SRG transformation and, more importantly, the initial chiral EFT *NNN* interaction.

In Fig. 36 and in Fig. 11 of Ref. [218], we compare our calculated differential cross section to the experimental data of Refs. [239,240] for four deuteron laboratory energies in the range $E_d \approx 3$–12 MeV. Our calculation over-predicts the measured cross section at $E_d = 2.94$ MeV, most likely a consequence of the incorrect position of the calculated

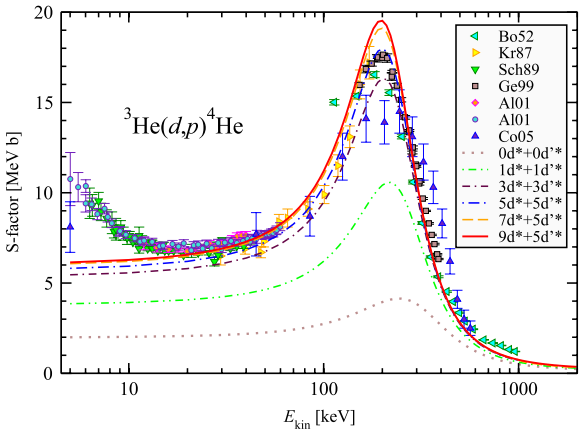

Fig. 37. Calculated S-factor of the ^{3}He(d, p) ^{4}He reaction compared to experimental data. Convergence with the number of deuterium pseudostates in the $^3S_1$-$^3D_1$ (d^*) and $^3D_2$ (d'^*) channels.

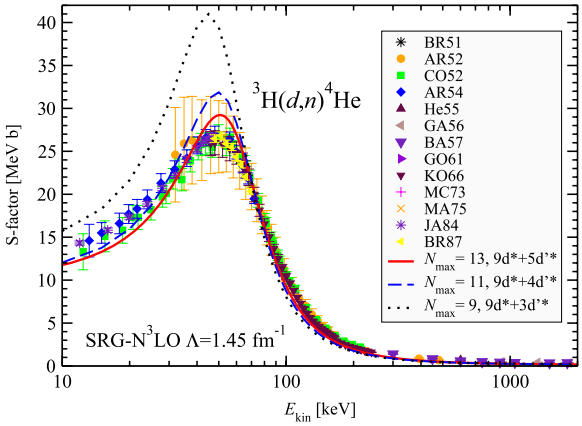

Fig. 38. Calculated ^{3}H(d, n) ^{4}He S-factor compared to experimental data. Convergence with N_{max} obtained for the SRG-N^{3}LO *NN* potential with $\lambda = 1.45$ fm^{-1} at $\hbar\Omega = 14$ MeV.

2^+0 resonance, see Fig. 35. However, for the intermediate energies, $E_d = 6.97$ and 8.97 MeV, the agreement with the measured data is reasonable. At $E_d = 12$ MeV the differences become larger. We also note that our calculated cross section underestimates the data in the range of $\theta_{c.m.} \approx 20 - 45$ deg. This is mostly due to our underestimation of positions of the $^3D_2$ and $^3D_1$ resonances.

6.1.4. *The* ^{3}H(d, n)^{4}He *and* ^{3}He(d, p)^{4}He *fusion reactions*

The ^{3}H(d, n) ^{4}He and ^{3}He(d, p) ^{4}He fusion reactions have important implications first and foremost for fusion energy generation, but also for nuclear astrophysics, and atomic physics. Indeed, the deuterium–tritium fusion is the easiest reaction to achieve on earth and is pursued by research facilities directed at reaching fusion power by either inertial (*e.g.*, NIF) or magnetic (*e.g.*, ITER) confinement. Both ^{3}H(d, n) ^{4}He and ^{3}He(d, p) ^{4}He affect the predictions of Big Bang nucleosynthesis for light-nucleus abundances. In addition, the deuterium-^{3}He fusion is also an object of interest for atomic physics, due to the substantial electron-screening effects presented by this reaction.

In the following we present the first *ab initio* many-body calculations [241] of these reactions starting from the SRG-N^{3}LO *NN* interaction with $\lambda = 1.5$ fm^{-1}, for which we reproduce the experimental Q-value of both reactions within 1%. We adopted HO model spaces up to $N_{max} = 13$ with a frequency of $\hbar\Omega = 14$ MeV. The channel basis includes n-^{4}He (p-^{4}He), d-^{3}H (d-^{3}He), d^*-^{3}H (d^*-^{3}He) and d'^*-^{3}H (d'^*-^{3}He) binary cluster states, where d^* and d'^* denote $^3S_1$-$^3D_1$ and $^3D_2$ deuterium excited pseudostates, respectively, and the ^{3}H (^{3}He) and ^{4}He nuclei are in their ground state.

Fig. 37 presents the results obtained for the ^{3}He(d, p) ^{4}He S-factor. The deuteron deformation and its virtual breakup, approximated by means of d pseudostates, play a crucial role. The S-factor increases dramatically with the number of pseudostates until convergence is reached for $9d^*+5d'^*$. The dependence upon the HO basis size is illustrated by the ^{3}H(d, n) ^{4}He results of Fig. 38. The convergence is satisfactory and we expect that an $N_{max} = 15$ calculation, which is currently out of reach, would not yield significantly different results. The experimental position of the ^{3}He(d, p) ^{4}He S-factor is reproduced within few tens of keV. Correspondingly, we find an overall fair agreement with experiment for this reaction, except a slightly

different shape of the peak than that suggested by the "Trojan-horse" data from Ref. [242], and if we exclude the region at very low energy, where the accelerator data of Ref. [243] are enhanced by laboratory electron screening.

The ^{3}H(d, n) ^{4}He S-factor is not described as well with $\lambda = 1.5$ fm^{-1}. Due to the very low activation energy of this reaction, the S-factor (particularly peak position and height) is extremely sensitive to higher-order effects in the nuclear interaction, such as *NNN* force (not yet included in the calculation) and missing isospin-breaking effects in the integration kernels (which are obtained in the isospin formalism). To compensate for these missing higher-order effects in the interaction and reproduce the position of the ^{3}H(d, n) ^{4}He S-factor, we performed additional calculations using lower λ values. This led to the theoretical S-factor of Fig. 38 (obtained for $\lambda = 1.45$ fm^{-1}), that is in overall better agreement with data, although it presents a slightly narrower and somewhat overestimated peak. This calculation would suggest that some electron-screening enhancement could also be present in the ^{3}H(d, n) ^{4}He measured S factor below 10 keV c.m. energy. However, these results cannot be considered conclusive until more accurate calculations, using a complete nuclear interaction (that includes the *NNN* force) are performed. Work in this direction is under way.

6.2. Ab initio no core shell model with continuum

It is possible and desirable to extend the binary-cluster $(A - a, a)$ NCSM/RGM basis by the standard A-nucleon NCSM basis to unify the original *ab initio* NCSM and NCSM/RGM approaches. This will lead to a much faster convergence of the many-body calculations compared to the original approaches as more correlations will be included and to an optimal and balanced unified description of both bound and unbound states.

In particular, we can generalize the expansion of the many-body wave function, given in Eq. (48), by explicitly including a set of A-nucleon NCSM eigenstates:

$$|\Psi^{J^\pi T}\rangle = \sum_\lambda c_\lambda^{J^\pi T} |A\lambda J^\pi T\rangle + \sum_\nu \int dr r^2\, \hat{\mathcal{A}}_\nu |\Phi_{\nu r}^{J^\pi T}\rangle \frac{[\mathcal{N}^{-1/2}\chi]_\nu^{J^\pi T}(r)}{r}, \tag{61}$$

where $H_A^{\rm NCSM}|A\lambda J^\pi T\rangle = E_\lambda |A\lambda J^\pi T\rangle$ with $H_A^{\rm NCSM}$, given by, *e.g.*, H of Eq. (1) (typically transformed by the SRG technique described in Section 3.4) projected on the $N_{\max}\hbar\Omega$ space. By projecting the many-body Schrödinger equation on the binary-cluster channel states (46) and the NCSM eigenstates, we arrive at a system of coupled equations that can be schematically written as

$$\begin{pmatrix} H^{\rm NCSM} & \mathfrak{h} \\ \mathfrak{h} & \mathcal{N}^{-\frac{1}{2}}\mathcal{H}\,\mathcal{N}^{-\frac{1}{2}} \end{pmatrix} \begin{pmatrix} c \\ \chi \end{pmatrix} = E \begin{pmatrix} 1 & \mathfrak{g} \\ \mathfrak{g} & 1 \end{pmatrix} \begin{pmatrix} c \\ \chi \end{pmatrix}. \tag{62}$$

Here, $\mathcal{H}$ and $\mathcal{N}$ are the Hamiltonian and norm integration kernels defined in Eq. (50). The $\mathfrak{g}$ are the overlap functions given by products of matrix elements $\langle A\lambda J^\pi T|\hat{\mathcal{A}}_\nu|\Phi_{\nu r}^{J^\pi T}\rangle$ [244] and the normalization factors $\mathcal{N}^{-\frac{1}{2}}$. Similarly, the $\mathfrak{h}$ are "vertex" functions defined by products of matrix elements $\langle A\lambda J^\pi T|H\hat{\mathcal{A}}_\nu|\Phi_{\nu r}^{J^\pi T}\rangle$, with H the intrinsic Hamiltonian that can be expressed, *e.g.*, as in Eq. (51), and the normalization factors $\mathcal{N}^{-\frac{1}{2}}$.

This formalism that we call no core shell model with continuum (NCSMC) was already discussed in the review article [29] in a non-orthonormalized form. The NCSMC has now been implemented and first results demonstrating usefulness of this approach are available for ^{7}He, described by a combination of ^{7}He NCSM eigenstates and ^{6}He+n NCSM/RGM clusters [245].

7. Summary and outlook

The *ab initio* NCSM treats all A nucleons equally with modern *NN*+*NNN* interactions and successfully describes properties of nuclei throughout the 0p-shell. In combination with the RGM, it provides a truly microscopic approach for nuclear reactions. Several investigations are underway to extend the *ab initio* NCSM to nuclei with $A > 16$ and to more completely unify the original *ab initio* NCSM with the NCSM/RGM approach. The outlook includes, but is not limited to:

1. Development of effective *NN*, *NNN* and even *NNNN* interactions for more detailed investigations of 0p- and sd-shell nuclei.
2. Development of symmetry-adapted basis spaces, such as, SU(3) [246].
3. Implementation of alternative single-particle basis spaces, such as, those originating from Hartree–Fock [247], purely phenomenological Woods–Saxon [248] or Coulomb–Sturmian [249].
4. Extension of the NCSM calculations to *sd*- and *pf*-shell nuclei, *i.e., ab initio* SM with a core.
5. Extension of the NCSM/RGM approach to nuclear reactions with more massive projectiles and three-cluster final states.
6. Further development of the NCSMC approach, i.e., the coupling of the binary-cluster $(A-a, a)$ NCSM/RGM basis and the standard A-nucleon NCSM basis to unify the original *ab initio* NCSM and NCSM/RGM approaches. This approach results in an optimal and balanced description of both bound and unbound states.
7. Improved extrapolation techniques for estimating converged results [250–252].
8. The development of new techniques for quantifying theoretical uncertainties [136,200,250].
9. Use of Importance Truncation in the form of the IT-NCSM and the IT-NCSM/RGM in nuclear structure and reaction calculations, respectively.
10. Use of Monte Carlo techniques to sample large no-core basis spaces, in conjunction with mean-field methods, to optimize the single-particle basis [253].

Acknowledgments

BRB acknowledges helpful discussions with I. Stetcu and M.K.G. Kruse and partial support of this work by the NSF under grants PHY-0555396 and PHY-0854912, PN acknowledges past support from the LLNL LDRD Grant No. PLS-09-ERD-020, the U.S. DOE/SC/NP (Work Proposal No. SCW0498) and the current support from the NSERC Grant No. 401945-2011, and JPV acknowledges partial support from DE-FG02-87ER40371, DE-FC02-09ER41582 (SciDAC/UNEDF), DESC0008485 and by the US NSF grant 0904782. TRIUMF receives funding via a contribution through the National Research Council Canada. Computational resources were provided by the National Energy Research Supercomputer Center (NERSC), which is supported by the Office of Science of the U.S. Department of Energy. Computational resources were also provided by Livermore Computing at LLNL, the LLNL Institutional Computing Grand Challenge program, by a "Petascale Early Science Award" and an INCITE Award on the Jaguar supercomputer at the Oak Ridge Leadership Computing Facility at ORNL which is supported by the DOE Office of Science under Contract DE-AC05-00OR22725.

Appendix. Overview of computational algorithm advances

Recent advances in solving the nuclear sparse matrix eigenvalue problem on leadership class facilities with greater efficiency include, among others:

1. Ref. [140] outlines the initial algorithms for parallel computation developed and implemented in Many-Fermion Dynamics nuclear ("MFDn"). This work features the matrix and vector distribution schemes, load balancing algorithms and the related communication topologies.
2. Ref. [254] describes approaches to integrate large scale structure calculations within search algorithms. One goal, for example, would be to optimize the low-energy constants of the chiral *NNN* interaction to fit selected states in a set of nuclei. Another application would be to optimize the basis space parameters for single-particle basis choices that are more general than the harmonic oscillator.
3. Ref. [255] presents advances in the computational scheme that achieve improved scalable performance by maintaining a good load balance among different processors and minimizing interprocessor communications. In addition, the paper contains several heuristics that reduce the number of integer and floating-point operations in the Hamiltonian calculation. These heuristics are developed by exploiting the unique combinatoric properties of the many-body configurations. Among other developments, this paper presents an advanced set of methods for efficiently determining the locations of the non-vanishing matrix elements of the many-body Hamiltonian.
4. Ref. [256] develops interfaces and parallel input/output procedures to use a well-known parallel I/O library (HDF5) in MFDn. The goal is to dramatically reduce the time to input and distribute large input Hamiltonian matrix element files such as those needed for *NNN* interactions in large basis spaces. In addition, large files generated for checkpointing require efficient output procedures. These procedures introduced here produce efficient input/output of large data sets along with their portability and ease of use in downstream processing.
5. Ref. [257] addresses the challenges raised by the increasing core counts of modern processors and the reduced amount of memory/core. The paper compares the performance of the pure MPI version with the hybrid MPI/OpenMP code on Cray XT4 and XT5 platforms and outlines conditions under which the hybrid version is preferred. For large nuclear structure calculations involving large core counts (typically 5,000 and above), the hybrid version is more efficient than pure MPI.
6. Ref. [258] begins to address the issues of "Big Data" and data accessibility raised by the expanding applications of MFDn to solve for properties of nuclei. The proposed solution is a data-base management system (DBMS) that is now operational and publicly available. (http://nuclear.physics.iastate.edu.) The system may be viewed as an enhanced logbook of production runs cataloged by the nuclear system, chosen Hamiltonian, basis space parameters, etc. It provides information on the observables calculated, stored wavefunction files and stored 1-body static and transition density matrices among other files of stored information. The DBMS may be viewed as a first step toward an eventual system providing full data provenance.
7. Ref. [259] presents a solution to the challenges posed, when the computational resource availability changes during the course of execution of an application due to the activities of other users. This is especially relevant for modern multi-user cluster environments, where users can run many high-performance applications simultaneously. In such a scenario, it is advantageous to target a computationally intensive part of the application and invoking appropriate adaptations during run-time to adjust to the dynamically changing system conditions, to prevent drastic performance loss. In this paper, the multi-threaded Lanczos diagonalization procedure in MFDn is targeted to observe the effect on performance of dynamically changing the number of threads during the iterative process using a middleware tool, such as (NICAN). These adaptive strategies produced performance gains between two to seven times in the presence of competing applications.
8. Ref. [260] addressed the goal of computing a number of lowest eigenvalues and eigenvectors of the Hamiltonian $\hat{H}$ with a fixed total angular momentum J. To achieve that goal, the paper introduced methods to compute the invariant subspace of the total angular momentum square operator $\hat{J}^2$ corresponding to a fixed and known eigenvalue $\lambda = J(J+1)$, and then to project $\hat{H}$ into this subspace in order to extract desired spectral information from the resulting lower dimensional Hamiltonian. The paper discussed how to compute the desired invariant subspace of $\hat{J}^2$ or equivalently, the null space

of $(\hat{J}^2 - \lambda I)$ efficiently on a large-scale distributed-memory high performance computer. The paper also demonstrated the performance of an optimized implementation by numerical experiments with light nuclei.

9. Ref. [261] exploits the inherent localities in the CI problem with a fixed-J basis and makes use of MPI one-sided communication routines backed by RDMA operations available in the new parallel architectures, to show that it is possible to reduce the input/output overheads drastically for large problems. This is demonstrated in the subspace projection phase of J-scheme calculations on the ^{6}Li nucleus, where a new implementation based on one-sided MPI communications outperforms the previous input/output implementation by almost a factor of 10.
10. Ref. [262] addresses a problem that arises with increasing processing core counts on modern computing platforms - i.e. the main memory accesses present a considerable execution bottleneck, leading to poor scalability in multithreaded applications. Even when the memory is physically divided into separate banks, each associated with a set of cores, i.e., exhibiting the so called nonuniform memory access (NUMA) architecture, the access time to the shared data structures may be detrimental to the scalability. Hence, it is imperative to carefully map large shared arrays to specific memory banks based on the nature of the computation and the multithreaded parallelism characteristics. This paper describes memory-pinning strategies pertinent to sparse matrix–vector multiplication and vector orthogonalization phases of MFDn. Several nuclei and nuclear interactions were considered in the large-scale test cases with the matrix dimensions ranging from 32 million to 320 million. Performance gains of up to 25% were observed with the proposed strategies as compared to the default memory placement policy.
11. Ref. [263] investigates the issue of significant communication overhead associated with the distributed sparse-matrix vector multiplication (SpMV) and orthogonalization of Lanczos vectors. The problem is most severe in large applications on modern multi-core architectures where network bandwidth is a scarce resource. This paper introduces an implementation of the parallel Lanczos algorithm with minimal communication overhead. Communication is minimized by a combination of three ideas: (i) processes are mapped to physical processors in a topology-aware manner, (ii) a hybrid MPI/OpenMP implementation that reduces the required communication volume significantly, and (iii) overlapping expensive communication operations with computations in SpMV. The paper presents performance gains achieved by applying a novel implementation of the parallel Lanczos algorithm to the sparse symmetric matrix eigenvalue problem and discusses how the new techniques can be extended to parallel sparse solvers, in general.
12. Ref. [264] demonstrates how the advent of high performance computing (HPC) platforms equipped with solid state drives (SSD) presents an opportunity to dramatically increase the efficiency of out-of-core numerical linear algebra computations. This paper details the advantages and challenges associated with performing sparse matrix–vector multiplications (SpMV) on a small SSD testbed. Such an endeavor requires programming abstractions that ease implementation, while enabling an efficient usage of the resources in the testbed. For this purpose, this paper adopts a task-based out-of-core programming model on top of a dataflow middleware based on the filter stream programming model. The paper compares the performance of the resulting out-of-core Lanczos algorithm running on the SSD testbed to the performance of an in-core implementation on a multi-core cluster for solving large-scale eigenvalue problems. Preliminary experiments indicate that the out-of-core implementation on the SSD testbed can compete with an in-core implementation in terms of total CPU-hours and energy efficiency. The researchers conclude with some architectural design suggestions that can enable numerical linear algebra computations in general to be carried out with high efficiency on SSD-equipped platforms.

References

[1] S.C. Pieper, V.R. Pandharipande, R.B. Wiringa, J. Carlson, Phys. Rev. C 64 (2001) 014001.
[2] S.C. Pieper, R.B. Wiringa, J. Carlson, Phys. Rev. C 70 (2004) 054325.
[3] M. Pervin, S.C. Pieper, R.B. Wiringa, Phys. Rev. C 76 (2007) 064319.
[4] L.E. Marcucci, M. Pervin, S.C. Pieper, R. Schiavilla, R.B. Wiringa, Phys. Rev. C 78 (2008) 065501.
[5] G. Hagen, T. Papenbrock, D.J. Dean, Phys. Rev. Lett. 103 (2009) 062503.
[6] G. Hagen, T. Papenbrock, D.J. Dean, M. Hjorth-Jensen, Phys. Rev. C 82 (2010) 034330. arXiv:1005.2627 [nucl-th].
[7] E. Epelbaum, H. Krebs, D. Lee, U.-G. Meissner, Phys. Rev. Lett. 106 (2011) 192501. arXiv:1101.2547 [nucl-th].
[8] P. Navrátil, J.P. Vary, B.R. Barrett, Phys. Rev. Lett. 84 (2000) 5728. arXiv:nucl-th/0004058.
[9] P. Navrátil, J.P. Vary, B.R. Barrett, Phys. Rev. C 62 (2000) 054311.
[10] R. Machleidt, F. Sammarruca, Y. Song, Phys. Rev. C 53 (1996) 1483. arXiv:nucl-th/9510023.
[11] R. Machleidt, Phys. Rev. C 63 (2001) 024001. nucl-th/0006014.
[12] R.B. Wiringa, V.G.J. Stoks, R. Schiavilla, Phys. Rev. C 51 (1995) 38. nucl-th/9408016.
[13] S.A. Coon, M.D. Scadron, P.C. McNamee, B.R. Barrett, D.W.E. Blatt, B.H.J. McKellar, Nucl. Phys. A 317 (1979) 242.
[14] S.A. Coon, H.K. Han, Few Body Syst. 30 (2001) 131. nucl-th/0101003.
[15] B.S. Pudliner, V.R. Pandharipande, J. Carlson, R.B. Wiringa, Phys. Rev. Lett. 74 (1995) 4396.
[16] S. Weinberg, Physica A 96 (1979) 327.
[17] S. Weinberg, Phys. Lett. B 251 (1990) 288.
[18] S. Weinberg, Nucl. Phys. B 363 (1991) 3.
[19] V. Bernard, N. Kaiser, U.-G. Meissner, Int. J. Mod. Phys. E 4 (1995) 193. hep-ph/9501384.
[20] C. Ordonez, L. Ray, U. van Kolck, Phys. Rev. Lett. 72 (1994) 1982.
[21] C. Ordonez, L. Ray, U. van Kolck, Phys. Rev. C 53 (1996) 2086. hep-ph/9511380.
[22] U. van Kolck, Prog. Part. Nucl. Phys. 43 (1999) 337. nucl-th/9902015.
[23] P.F. Bedaque, U. van Kolck, Ann. Rev. Nucl. Part. Sci. 52 (2002) 339. nucl-th/0203055.
[24] E. Epelbaum, Prog. Part. Nucl. Phys. 57 (2006) 654. nucl-th/0509032.
[25] E. Epelbaum, W. Gloeckle, U.-G. Meissner, Nucl. Phys. A 637 (1998) 107. nucl-th/9801064.
[26] E. Epelbaum, W. Gloeckle, U.-G. Meissner, Nucl. Phys. A 671 (2000) 295. nucl-th/9910064.

[27] D.R. Entem, R. Machleidt, Phys. Rev. C 68 (2003) 041001. nucl-th/0304018.
[28] R. Machleidt, D.R. Entem, Phys. Rep. 503 (2011) 1. arXiv:1105.2919 [nucl-th].
[29] P. Navrátil, S. Quaglioni, I. Stetcu, B.R. Barrett, J. Phys. G 36 (2009) 083101. arXiv:0904.0463 [nucl-th].
[30] M.G. Mayer, Phys. Rev. 75 (1949) 1969.
[31] M.G. Mayer, Phys. Rev. 78 (1950) 22.
[32] O. Haxel, J.H.D. Jensen, H.E. Suess, Phys. Rev. 75 (1949) 1766.
[33] J.P. Elliott, B.H. Flowers, Proc. Roy. Soc. A229 (1955) 561.
[34] J.P. Elliott, A.M. Lane, The Nuclear Shell Model, in: S. Flügge (Ed.), Encyclopedia of Physics, vol. XXXIX, Springer-Verlag, Berlin, 1957.
[35] B.A. Brown, B.H. Wildenthal, Status of the Nuclear Shell Model, Ann. Rev. Nucl. Part. Sci. 38 (1988) 29.
[36] I. Talmi, Simple Models of Complex Nuclei: The Shell Model and Interacting Boson Model, Harwood Academic Publishers, Chur, 1993.
[37] J.F. Dawson, I. Talmi, J.D. Walecka, Ann. Phys. (N.Y.) 18 (1962) 339.
[38] T.T.S. Kuo, G.E. Brown, Nucl. Phys. 85 (1966) 40.
[39] G.E. Brown, T.T.S. Kuo, J.W. Holt, S. Lee (Eds.), The Nucleon–Nucleon Interaction and the Nuclear Many-Body Problem, World Scientific Publishers, Singapore, 2010.
[40] C. Bloch, J. Horowitz, Nucl. Phys. 8 (1958) 91.
[41] B.H. Brandow, Mod. Phys. 39 (1967) 771.
[42] A.de. Shalit, H. Feshbach, Theoretical Nuclear Physics Volume 1: Nuclear Structure, John Wiley, New York, 1974, p. 177.
[43] B.R. Barrett, R.G.L. Hewitt, R.J. McCarthy, Phys. Rev. C 3 (1971) 1137.
[44] J.P. Vary, P.U. Sauer, C.W. Wong, Phys. Rev. C 7 (1973) 1776.
[45] B.R. Barrett, M.W. Kirson, Nucl. Phys. A148 (1970) 145.
[46] B.R. Barrett, M.W. Kirson, The Microscopic Theory of Nuclear Effective Interactions and Operators, in: M. Baranger, E. Vogt (Eds.), Advances in Nuclear Physics, vol. 6, Plenum Press, New York, 1973, p. 219.
[47] T.H. Schucan, H.A. Weidenmüller, Ann. Phys. (N.Y.) 73 (1972) 108.
[48] T.H. Schucan, H.A. Weidenmüller, Ann. Phys. (N.Y.) 76 (1973) 483.
[49] B.R. Barrett (Ed.), Effective Interactions and Operators in Nuclei, in: Lecture Notes in Physics, vol. 40, Springer-Verlag, Berlin, 1975.
[50] H. Kümmel, K.H. Lürhmann, J.G. Zabolitsky, Phys. Rep. C 36 (1978) 1.
[51] J.P. Vary, R.H. Belehrad, B.J. Dalton, Nucl. Phys. A 328 (1979) 526.
[52] J.P. Vary, in: B.J. Dalton, S.M. Grimes, J.P. Vary, S.A. Williams (Eds.), Theory and Applications of Moment Methods in Many-Fermion Systems, Plenum Press, New York, 1980, p. 423.
[53] F.J. Margetan, J.P. Vary, Phys. Rev. C 28 (1983) 907.
[54] R.V. Reid Jr., Ann. Physics 50 (1968) 411.
[55] L. Jaqua, M.A. Hasan, J.P. Vary, B.R. Barrett, Phys. Rev. C 46 (1992) 2333.
[56] L. Jaqua, P. Halse, B.R. Barrett, J.P. Vary, Nucl. Phys. A571 (1994) 242.
[57] D.C. Zheng, B.R. Barrett, L. Jaqua, J.P. Vary, R.J. McCarthy, Phys. Rev. C 48 (1993) 1083. nucl-th/9304025.
[58] B.R. Barrett, P. Halse, L.M. Jaqua, J.P. Vary, Phys. Rep. 242 (1994) 85.
[59] D.C. Zheng, B.R. Barrett, Phys. Rev. C 49 (1994) 3342. nucl-th/9311007.
[60] D.C. Zheng, J.P. Vary, B.R. Barrett, Phys. Rev. C 50 (1994) 2841. nucl-th/9405018.
[61] S. Okubo, Progr. Theor. Phys. 12 (1954) 603.
[62] K. Suzuki, S.Y. Lee, Progr. Theor. Phys. 64 (1980) 2091.
[63] K. Suzuki, Progr. Theor. Phys. 68 (1982) 246.
[64] K. Suzuki, R. Okamoto, Progr. Theor. Phys. 70 (1983) 439.
[65] K. Suzuki, Progr. Theor. Phys. 68 (1982) 1999.
[66] K. Suzuki, R. Okamoto, Progr. Theor. Phys. 92 (1994) 1045.
[67] D.C. Zheng, J.P. Vary, B.R. Barrett, Nucl. Phys. A 560 (1993) 211. nucl-th/9301013.
[68] D.C. Zheng, B.R. Barrett, J.P. Vary, R.J. McCarthy, Phys. Rev. C 49 (1994) 1999.
[69] D.C. Zheng, B.R. Barrett, J.P. Vary, W.C. Haxton, C.L. Song, Phys. Rev. C 52 (1995) 2488.
[70] P. Navrátil, B.R. Barrett, Phys. Rev. C 54 (1996) 2986. nucl-th/9609046.
[71] P. Navrátil, B.R. Barrett, Phys. Rev. C 57 (1998) 562. arXiv:nucl-th/9711027.
[72] P. Navrátil, B.R. Barrett, Phys. Rev. C 59 (1999) 1906. nucl-th/9812062.
[73] P. Navrátil, G.P. Kamuntavicius, B.R. Barrett, Phys. Rev. C 61 (2000) 044001. nucl-th/9907054.
[74] B.S. Pudliner, V.R. Pandharipande, J. Carlson, S.C. Pieper, R.B. Wiringa, Phys. Rev. C 56 (1997) 1720. nucl-th/9705009.
[75] R.B. Wiringa, Nucl. Phys. A 631 (1998) 70c.
[76] R.B. Wiringa, S.C. Pieper, J. Carlson, V.R. Pandharipande, Phys. Rev. C 62 (2000) 014001. nucl-th/0002022.
[77] D.C.J. Marsden, P. Navrátil, S.A. Coon, B.R. Barrett, Phys. Rev. C 66 (2002) 044007.
[78] I. Stetcu, B.R. Barrett, P. Navrátil, J.P. Vary, Phys. Rev. C 71 (2005) 044325. nucl-th/0412004.
[79] I. Stetcu, B.R. Barrett, P. Navrátil, C.W. Johnson, Int. J. Mod. Phys. E 14 (2005) 95. nucl-th/0409072.
[80] I. Stetcu, B.R. Barrett, P. Navrátil, J.P. Vary, Eur. Phys. J. A 25 (2005) 489. s01.
[81] I. Stetcu, B.R. Barrett, P. Navrátil, J.P. Vary, Phys. Rev. C 73 (2006) 037307. nucl-th/0601076.
[82] I. Stetcu, J. Rotureau, Progr. Part. Nucl. Phys. 69 (2013) 182.
[83] M.A. Hasan, S. Koehler, J.P. Vary, Phys. Rev. C 36 (1987) 2180.
[84] M.A. Hasan, S. Koehler, J.P. Vary, Phys. Rev. C 36 (1987) 2649.
[85] M.A. Hasan, J.P. Vary, Phys. Rev. C 50 (1994) 202.
[86] J.P. Vary, M.A. Hasan, Nucl. Phys. A 570 (1994) 355c.
[87] M.A. Hasan, J.P. Vary, Phys. Rev. C 54 (1996) 3035.
[88] M.A. Hasan, J.P. Vary, T.S.H. Lee, Phys. Rev. C 56 (1997) 3063.
[89] M.A. Hasan, J.P. Vary, T.-S.H. Lee, Phys. Rev. C 61 (2000) 014301.
[90] M.A. Hasan, J.P. Vary, T.-S.H. Lee, Phys. Rev. C 64 (2001) 024306.
[91] G. Bozzolo, J.P. Vary, Phys. Rev. C 31 (1985) 1909.
[92] G. Bozzolo, O. Civitarese, J.P. Vary, Phys. Rev. C 37 (1988) 1240.
[93] M. Saraceno, J.P. Vary, G. Bozzolo, H.G. Miller, Phys. Rev. C 37 (1988) 1267.
[94] M.A. Hasan, J.P. Vary, Phys. Rev. C 58 (1998) 2754.
[95] B.R. Barrett, D.C. Zheng, R.J. McCarthy, J.P. Vary, Phys. Lett. B316 (1993) 219.
[96] L. Jaqua, D.C. Zheng, B.R. Barrett, J.P. Vary, Phys. Rev. C 48 (1993) 1765.
[97] D.C. Zheng, B.R. Barrett, J.P. Vary, H. Muther, Phys. Rev. C 51 (1995) 2471. nucl-th/9410048.
[98] P. Navrátil, B.R. Barrett, Phys. Lett. B 369 (1996) 193.
[99] M. Thoresen, D.C. Zheng, B.R. Barrett, Phys. Rev. C 53 (1996) 1997.
[100] M. Thoresen, P. Navrátil, B.R. Barrett, Phys. Rev. C 57 (1998) 3108. nucl-th/9804016.
[101] P. Doleschall, Phys. Rev. C 69 (2004) 054001.
[102] S.K. Bogner, R.J. Furnstahl, R.J. Perry, Phys. Rev. C 75 (2007) 061001. nucl-th/0611045.
[103] S. Bogner, T.T.S. Kuo, L. Coraggio, A. Covello, N. Itaco, Phys. Rev. C 65 (2002) 051301.
[104] S.K. Bogner, T.T.S. Kuo, A. Schwenk, Phys. Rep. 386 (2003) 1. nucl-th/0305035.

[105] R. Roth, H. Hergert, P. Papakonstantinou, T. Neff, H. Feldmeier, Phys. Rev. C 72 (2005) 034002. nucl-th/0505080.
[106] R. Roth, T. Neff, H. Feldmeier, Prog. Part. Nucl. Phys. 65 (2010) 50. arXiv:1003.3624 [nucl-th].
[107] A.M. Shirokov, A.I. Mazur, S.A. Zaytsev, J.P. Vary, T.A. Weber, Phys. Rev. C 70 (2004) 044005.
[108] A.M. Shirokov, J.P. Vary, A.I. Mazur, S.A. Zaytsev, T.A. Weber, Phys. Lett. B 621 (2005) 96.
[109] A.M. Shirokov, J.P. Vary, A.I. Mazur, T.A. Weber, Phys. Lett. B 644 (2007) 33. arXiv:nucl-th/0512105. A Fortran code for JISP16 is available at the web site: nuclear.physics.iastate.edu.
[110] D.H. Gloekner, D.R. Lawson, Phys. Lett. B 53 (1974) 313.
[111] M. Moshinsky, Nucl. Phys. 13 (1959) 104.
[112] P. Navrátil, B.R. Barrett, W. Gloeckle, Phys. Rev. C 59 (1999) 611. nucl-th/9811074.
[113] L. Trlifaj, Phys. Rev. C 5 (1972) 1534.
[114] P. Navrátil, H.B. Geyer, T.T.S. Kuo, Phys. Lett. B 315 (1993) 1;
P. Navrátil, H.B. Geyer, Nucl. Phys. A 556 (1993) 165.
[115] C.P. Viazminsky, J.P. Vary, J. Math. Phys. 42 (2001) 2055.
[116] P. Navrátil, W.E. Ormand, Phys. Rev. C 68 (2003) 034305. arXiv:nucl-th/0305090.
[117] A. Nogga, P. Navrátil, B.R. Barrett, J.P. Vary, Phys. Rev. C 73 (2006) 064002. arXiv:nucl-th/0511082.
[118] S.D. Glazek, K.G. Wilson, Phys. Rev. D 48 (1993) 5863.
[119] F. Wegner, Ann. Phys. (Leipzig) 3 (1994) 77.
[120] S.K. Bogner, R.J. Furnstahl, R.J. Perry, A. Schwenk, Phys. Lett. B 649 (2007) 488. nucl-th/0701013.
[121] F.J. Wegner, Phys. Rep. 348 (2001) 77.
[122] S. Kehrein, Springer Tracts Mod. Phys. 217 (2006) 137.
[123] E.D. Jurgenson, S.K. Bogner, R.J. Furnstahl, R.J. Perry, et al., Phys. Rev. C 78 (2008) 014003.
[124] S.D. Glazek, R.J. Perry, Phys. Rev. D 78 (2008) 045011.
[125] E. Anderson, S.K. Bogner, R.J. Furnstahl, E.D. Jurgenson, R.J. Perry, A. Schwenk, Phys. Rev. C 77 (2008) 037001.
[126] S.K. Bogner, R.J. Furnstahl, R.J. Perry, Ann. Physics 323 (2008) 1478.
[127] E.D. Jurgenson, R.J. Furnstahl, Nucl. Phys. A 818 (2009) 152.
[128] E.D. Jurgenson, P. Navrátil, R.J. Furnstahl, Phys. Rev. Lett. 103 (2009) 082501. arXiv:0905.1873 [nucl-th].
[129] E.D. Jurgenson, P. Navrátil, R.J. Furnstahl, Phys. Rev. C 83 (2011) 034301. arXiv:1011.4085 [nucl-th].
[130] R. Roth, J. Langhammer, A. Calci, S. Binder, P. Navratil, Phys. Rev. Lett. 107 (2011) 072501. arXiv:1105.3173 [nucl-th].
[131] K. Hebeler, Phys. Rev. C 85 (2012) 021002. arXiv:1201.0169 [nucl-th].
[132] P. Navrátil, W.E. Ormand, Phys. Rev. Lett. 88 (2002) 152502.
[133] P. Navrátil, E. Caurier, Phys. Rev. C 69 (2004) 014311. nucl-th/0311036.
[134] M. Viviani, L.E. Marcucci, S. Rosati, A. Kievsky, L. Girlanda, Few Body Syst. 39 (2006) 159. nucl-th/0512077.
[135] E. Caurier, G. Martinez-Pinedo, F. Nowacki, A. Poves, J. Retamosa, A.P. Zuker, Phys. Rev. C 59 (1999) 2033;
E. Caurier, F. Nowacki, Acta Phys. Pol. B 30 (1999) 705.
[136] C. Forssén, E. Caurier, P. Navratil, Phys. Rev. C 79 (2009) 021303. arXiv:0901.0453 [nucl-th].
[137] P. Navrátil, J.P. Vary, W.E. Ormand, B.R. Barrett, Phys. Rev. Lett. 87 (2001) 172502.
[138] E. Caurier, P. Navrátil, Phys. Rev. C 73 (2006) 021302. nucl-th/0512015.
[139] C. Forssén, J.P. Vary, E. Caurier, P. Navrátil, Phys. Rev. C 77 (2008) 024301. arXiv:0802.1611 [nucl-th].
[140] J.P. Vary, P. Maris, E. Ng, C. Yang, M. Sosonkina, J. Phys. Conf. Ser. 180 (2009) 012083. arXiv:0907.0209 [nucl-th].
[141] U. van Kolck, Phys. Rev. C 49 (1994) 2932.
[142] E. Epelbaum, A. Nogga, W. Gloeckle, H. Kamada, U.G. Meissner, H. Witala, Phys. Rev. C 66 (2002) 064001. nucl-th/0208023.
[143] E. Epelbaum, Phys. Lett. B 639 (2006) 456. nucl-th/0511025.
[144] T.S. Park, L.E. Marcucci, R. Schiavilla, M. Viviani, A. Kievsky, S. Rosati, K. Kubodera, D.P. Min, et al., Phys. Rev. C 67 (2003) 055206. nucl-th/0208055.
[145] D. Gazit, S. Quaglioni, P. Navrátil, Phys. Rev. Lett. 103 (2009) 102502. arXiv:0812.4444 [nucl-th].
[146] P. Navrátil, Few Body Syst. 41 (2007) 117. arXiv:0707.4680 [nucl-th].
[147] E. Borie, G.A. Rinker, Phys. Rev. A 18 (1978) 324;
S. Kopecky, et al., Phys. Rev. Lett. 74 (1995) 2447;
P. Mohr, B. Taylor, Rev. Mod. Phys. 596 (1996) 367;
I. Sick, Phys. Lett. B 576 (2003) 62.
[148] A. Nogga, H. Kamada, W. Gloeckle, B.R. Barrett, Phys. Rev. C 65 (2002) 054003. nucl-th/0112026.
[149] A. Kievsky, S. Rosati, M. Viviani, L.E. Marcucci, L. Girlanda, J. Phys. G 35 (2008) 063101. arXiv:0805.4688 [nucl-th].
[150] D.R. Tilley, et al., Nucl. Phys. A 708 (2002) 3.
[151] P. Navrátil, V.G. Gueorguiev, J.P. Vary, W.E. Ormand, A. Nogga, Phys. Rev. Lett. 99 (2007) 042501. nucl-th/0701038.
[152] A.F. Lisetskiy, M.K.G. Kruse, B.R. Barrett, P. Navrátil, I. Stetcu, J.P. Vary, Phys. Rev. C 80 (2009) 024315. arXiv:0906.2829 [nucl-th].
[153] P. Maris, J.P. Vary, P. Navrátil, arXiv:1205.5686 [nucl-th].
[154] www.nndc.bnl.gov/amdc/masstables/Ame2003/mass.mas03round.
[155] W. Nortershauser, T. Neff, R. Sanchez, I. Sick, Phys. Rev. C 84 (2011) 024307.
[156] F. Ajzenberg-Selove, Nucl. Phys. A 490 (1988) 1.
[157] D.R. Tilley, C.M. Cheves, J.L. Godwin, G.M. Hale, H.M. Hofmann, J.H. Kelley, C.G. Sheu, H.R. Weller, Nucl. Phys. A 708 (2002) 3.
[158] R. Roth, et al. Private communication (in preparation).
[159] C. Cockrell, J.P. Vary, P. Maris, Phys. Rev. C 86 (2012) 034325. arXiv:1201.0724.
[160] D.R. Tilley, J.H. Kelley, J.L. Godwin, D.J. Millener, J.E. Purcell, C.G. Sheu, H.R. Weller, Nucl. Phys. A 745 (2004) 155.
[161] G. Audi, O. Bersillon, J. Blachot, A.H. Wapstra, Nucl. Phys. A 729 (2003) 3.
[162] S. Cohen, D. Kurath, Nucl. Phys. 73 (1965) 1.
[163] P. Navrátil, C.A. Bertulani, E. Caurier, Phys. Rev. C 73 (2006) 065801. arXiv:nucl-th/0601019.
[164] E. Caurier, P. Navrátil, W.E. Ormand, J.P. Vary, Phys. Rev. C 66 (2002) 024314.
[165] S.C. Pieper, K. Varga, R.B. Wiringa, Phys. Rev. C 66 (2002) 044310. arXiv:nucl-th/0206061.
[166] E.A. McCutchan, et al., Phys. Rev. Lett. 103 (2009) 192501. arXiv:0907.3688 [nucl-ex].
[167] E.A. McCutchan, C.J. Lister, S.C. Pieper, R.B. Wiringa, D. Seweryniak, J.P. Greene, P.F. Bertone, M.P. Carpenter, et al., Phys. Rev. C 86 (2012) 014312. arXiv:1201.2960 [nucl-ex].
[168] J.N. Orce, et al., Phys. Rev. C 86 (2012) 041303(R).
[169] C. Forssén, R. Roth, P. Navrátil, arXiv:1110.0634 [nucl-th].
[170] I.S. Towner, J.C. Hardy, M. Harvey, Nucl. Phys. A284 (1977) 269.
[171] W.E. Ormand, B.A. Brown, Phys. Rev. Lett. 62 (1989) 866.
[172] J.C. Hardy, I.S. Towner, V.T. Koslowsky, E. Hagberg, H. Schmeing, Nucl. Phys. A509 (1990) 429.
[173] N. Cabibbo, Phys. Rev. Lett. 10 (1963) 531;
M. Kobayashi, T. Maskawa, Prog. Theor. Phys. 49 (1973) 652.
[174] W. Jaus, G. Rasche, Phys. Rev. D41 (1990) 166;
I.S. Towner, Nucl. Phys. A540 (1992) 478.
[175] F.C. Barker, B.A. Brown, W. Jaus, G. Rasche, Nucl. phys. A540 (1992) 501;
J.F. Donoghue, B.R. Holstein, S.W. Klimt, Phys. Rev. D 35 (1987) 934.

[176] W.E. Ormand, B.A. Brown, Phys. Rev. C 52 (1995) 2455.
[177] J.C. Hardy, I.S. Towner, Phys. Rev. C 79 (2009) 055502. arXiv:0812.1202 [nucl-ex].
[178] P. Navrátil, B.R. Barrett, W.E. Ormand, Phys. Rev. C 56 (1997) 2542. arXiv:nucl-th/9708032.
[179] LSND collaboration, L.B. Auerbach, et al., Phys. Rev. C 64 (2001) 065501.
[180] LSND collaboration, L.B. Auerbach, et al., Phys. Rev. C 66 (2002) 015501.
[181] G.H. Miller, et al., Phys. Lett. 41B (1972) 50;
M. Giffon, et al., Phys. Rev. C 24 (1981) 241.
[182] A.C. Hayes, P. Navrátil, J.P. Vary, Phys. Rev. Lett. 91 (2003) 012502. nucl-th/0305072.
[183] E. Kolbe, K. Langanke, P. Vogel, Nucl. Phys. A 652 (1999) 91. arXiv:nucl-th/9903022.
[184] A.C. Hayes, I.S. Towner, Phys. Rev. C 61 (2000) 044603. arXiv:nucl-th/9907049.
[185] S. Bowman, Interpreting the Past: Radiocarbon Dating, University of California Press, Berkeley, ISBN: 0520070372, 1990.
[186] O. Bergmann, et al., Science 324 (2009) 98.
[187] S. Aroua, P. Navrátil, L. Zamick, M.S. Fayache, B.R. Barrett, J.P. Vary, K. Heyde, Nucl. Phys. A 720 (2003) 71.
[188] B. Jancovici, I. Talmi, Phys. Rev. 95 (1954) 289.
[189] P. Maris, J.P. Vary, P. Navrátil, W.E. Ormand, H. Nam, D.J. Dean, Phys. Rev. Lett. 106 (2011) 202502. arXiv:1101.5124 [nucl-th].
[190] J.W. Holt, N. Kaiser, W. Weise, Phys. Rev. C 81 (2010) 024002. arXiv:0910.1249 [nucl-th].
[191] F. Ajzenberg-Selove, Nucl. Phys. A 523 (1991) 1. TUNL Nuclear Data Evaluation Group. www.tunl.duke.edu.
[192] A. Negret, T. Adachi, B.R. Barrett, C. Baumer, A.M. Van den berg, G.P.A. Berg, P. Von brentano, D. Frekers, et al., Phys. Rev. Lett. 97 (2006) 062502.
[193] P. Doleschall, I. Borbély, Z. Papp, W. Plessas, Phys. Rev. C 67 (2003) 0064005.
[194] C. Forssén, P. Navrátil, W.E. Ormand, E. Caurier, Phys. Rev. C 71 (2005) 044312. nucl-th/0412049.
[195] R. Roth, P. Navrátil, Phys. Rev. Lett. 99 (2007) 092501. arXiv:0705.4069 [nucl-th].
[196] R. Roth, Phys. Rev. C 79 (2009) 064324. arXiv:0903.4605 [nucl-th].
[197] R. Roth, private communication.
[198] P. Maris, private communication.
[199] A.F. Lisetskiy, B.R. Barrett, M.K.G. Kruse, P. Navrátil, I. Stetcu, J.P. Vary, Phys. Rev. C 78 (2008) 044302. arXiv:0808.2187 [nucl-th].
[200] M.K.G. Kruse, Ph.D. Dissertation, unpublished, private communication, 2012. URL: gradworks.umi.com/35/05/3505985.html.
[201] I. Stetcu, B.R. Barrett, U. van Kolck, Phys. Lett. B 653 (2007) 358. nucl-th/0609023.
[202] I. Stetcu, J. Rotureau, B.R. Barrett, U. van Kolck, J. Phys. G 37 (2010) 064033. arXiv:0912.3015 [nucl-th].
[203] J. Rotureau, I. Stetcu, B.R. Barrett, U. van Kolck, Phys. Rev. C 85 (2012) 034003. arXiv:1112.0267 [nucl-th].
[204] P. Navrátil, M. Thoresen, B.R. Barrett, Phys. Rev. C 55 (1997) 573. arXiv:nucl-th/9612015.
[205] D.J. Dean, G. Hagen, M. Hjorth-Jensen, T. Papenbrock, A. Schwenk, Phys. Rev. Lett. 101 (2008) 119201. URL http://link.aps.org/doi/10.1103/PhysRevLett.101.119201.
[206] R. Roth, P. Navrátil, Phys. Rev. Lett. 101 (2008) 119202. URL http://link.aps.org/doi/10.1103/PhysRevLett.101.119202.
[207] C.D. Sherrill, H.F. Schaefer III, Adv. Quantum Chem. 34 (1999) 143. URL http://www.sciencedirect.com/science/article/pii/S0065327608605328.
[208] Z. Rolik, Á. Szabados, P.R. Surján, J. Chem. Phys. 119 (2003) 1922. URL http://link.aip.orf/link.?JCP/119/1922/1.
[209] P.R. Surján, Z. Rolik, Á. Szabados, D. Köhalmi, Ann. Phys., Lpz. 13 (2004) 223. ISSN 1521-3889. URL http://dx.doi.org/10.1002/andp.200310074.
[210] M.K.G. Kruse, et al. Private communication, 2012 (in preparation).
[211] P. Navrátil, R. Roth, S. Quaglioni, Phys. Rev. C 82 (2010) 034609. arXiv:1007.0525 [nucl-th].
[212] K.M. Nollett, S.C. Pieper, R.B. Wiringa, J. Carlson, G.M. Hale, Phys. Rev. Lett. 99 (2007) 022502. nucl-th/0612035.
[213] G. Hagen, D.J. Dean, M. Hjorth-Jensen, T. Papenbrock, Phys. Lett. B 656 (2007) 169. nucl-th/0610072.
[214] ITER, URL http://www.iter.org/.
[215] NIF URL https://lasers.llnl.gov/.
[216] S. Quaglioni, P. Navrátil, Phys. Rev. Lett. 101 (2008) 092501. arXiv:0804.1560 [nucl-th].
[217] S. Quaglioni, P. Navrátil, Phys. Rev. C 79 (2009) 044606. arXiv:0901.0950 [nucl-th].
[218] P. Navratil, S. Quaglioni, Phys. Rev. C 83 (2011) 044609. arXiv:1102.2042 [nucl-th].
[219] K. Wildermuth, Y.C. Tang, A Unified Theory of The Nucleus, Braunschweig, Vieweg, 1977.
[220] M. Hesse, J.M. Sparenberg, F.V. Raemdonck, D. Baye, Nucl. Phys. A 640 (1998) 37.
[221] M. Hesse, J. Roland, D. Baye, Nucl. Phys. A 709 (2002) 184.
[222] A.M. Lane, R.G. Thomas, Mod. Phys. 30 (1958) 257.
[223] P. Descouvemont, D. Baye, Rep. Progr. Phys. 73 (2010) 036301.
[224] G.M. Hale, Private communication.
[225] R. Roth, S. Reinhardt, H. Hergert, Phys. Rev. C 77 (2008) 064003.
[226] P. Schwandt, T.B. Clegg, W. Haeberli, Nucl. Phys.A 163 (1971) 432.
[227] K.W. Brokman, Phys. Rev. 108 (1957) 1000.
[228] D.C. Dodder, G.M. Hale, N. Jarmie, J.H. Jett, P.W. Keaton, R.A. Nisley, K. Witte, Phys. Rev. C 15 (1977) 518.
[229] R.A. Hardekopf, G.G. Ohlsen, Phys. Rev. C 15 (1977) 514.
[230] E.G. Adelberger, S.M. Austin, J.N. Bahcall, A.B. Balantekin, G. Bogaert, L. Brown, L. Buchmann, F.E. Cecil, et al., Mod. Phys. 70 (1998) 1265. astro-ph/9805121.
[231] P. Navrátil, R. Roth, S. Quaglioni, Phys. Lett. B 704 (2011) 379.
[232] P. Descouvemont, Phys. Rev. C 70 (2004) 065802.
[233] F. Schümann, et al., Phys. Rev. Lett. 73 (2003) 232501.
[234] F. Schümann, et al., Phys. Rev. C 73 (2006) 015806.
[235] A.R. Junghans, et al., Phys. Rev. C 68 (2003) 065803.
[236] E.E. Adelberger, et al., Mod. Phys. 83 (2011) 195.
[237] W. Gruebler, P.A. Schmelzbach, V. Konig, R. Risler, D. Boerma, Nucl. Phys. A 242 (1975) 265.
[238] B. Jenny, W. Gruebler, V. Konig, P.A. Schmelzbach, C. Schweizer, Nucl. Phys. A 397 (1983) 61.
[239] L.S. Senhouse Jr., T.A. Tombrello, Nucl. Phys. 57 (1964) 624.
[240] J.H. Jett, J.L. Detch Jr., N. Jarmie, Phys. Rev. C 3 (1971) 1769.
[241] P. Navrátil, S. Quaglioni, Phys. Rev. Lett. 108 (2012) 042503.
[242] M.La. Cognata, C. Spitaleri, A. Tumino, S. Typel, S. Cherubini, L. Lamia, A. Musumarra, R.G. Pizzone, et al., Phys. Rev. C 72 (2005) 065802.
[243] M.A. Aliotta, et al., Nucl. Phys. A 690 (2001) 790.
[244] P. Navratil, Phys. Rev. C 70 (2004) 054324. nucl-th/0410052.
[245] S. Baroni, P. Navrátil, S. Quaglioni, arXiv:1210.1897 [nucl-th].
[246] T. Dytrych, K.D. Sviratcheva, J.P. Draayer, C. Bahri, J.P. Vary, J. Phys. G. 35 (2008) 123101.
[247] M.A. Hasan, J.P. Vary, P. Navrátil, Phys. Rev. C 69 (2004) 034332. nucl-th/0312008.
[248] Gianina Alina Negoita, Ab initio Nuclear Structure Theory, Doctoral dissertation, Iowa State University, 2010. ProQuest.com, UMI 11359.
[249] M. Caprio, P. Maris, J.P. Vary, Phys. Rev. C 86 (2012) 034312.
[250] P. Maris, J.P. Vary, A.M. Shirokov, Phys. Rev. C 79 (2009) 014308. arXiv:0808.3420 [nucl-th].
[251] S.A. Coon, M.I. Avetian, M.K.G. Kruse, B. van Kolck, P. Maris, J.P. Vary, Phys. Rev. C. 86 (2012) 054002. arXiv:1205.3230 [nucl-th].
[252] R.J. Furnstahl, G. Hagen, T. Papenbrock, Phys. Rev. C 86 (2012) 031301. arXiv:1207.6100 [nucl-th].
[253] T. Abe, P. Maris, T. Otsuka, N. Shimizu, Y. Utsuno, J.P. Vary, Phys. Rev. C. 86 (2012) 054301. arXiv:1204.1755 [nucl-th].

[254] M. Sosonkina, A. Sharda, A. Negoita, J.P. Vary, in: M. Bubak, G.D.v. Albada, J. Dongarra, P.M.A. Sloot (Eds.), Lecture Notes in Computer Science, vol. 5101, 2008, p. 833.
[255] P. Sternberg, E.G. Ng, C. Yang, P. Maris, J.P. Vary, M. Sosonkina, H.V. Le, Proceedings of the 2008 ACM/IEEE Conference on Supercomputing (Austin, Texas, November 15–21, 2008), Conference on High Performance Networking and Computing, IEEE Press, Piscataway, NJ, 2008, pp. 1–12.
[256] N. Laghave, M. Sosonkina, P. Maris, J.P. Vary, et al., in: G. Allen (Ed.), ICCS 2009, Part I, in: LNCS, 5544, Springer Verlag, Berlin, 2009, p. 84.
[257] P. Maris, M. Sosonkina, J.P. Vary, E.G. Ng, C. Yang, International Conference on Computer Science, ICCS 2010, in: Procedia Computer Science, vol. 1, 2010, p. 97.
[258] F. Liu, R. Mundhe, M. Sosonkina, C. Cockrell, M. Aronnax, P. Maris, J.P. Vary, Proceedings of High Performance Computing 2011, HPC-2011 (in press).
[259] A. Srinivasa, M. Sosonkina, P. Maris, J.P. Vary, Proceedings of 12th IEEE International Workshop on Parallel and Distributed Scientific and Engineering Computing, PDSEC-11, ipdpsw, 1332, 2011.
[260] H.M. Aktulga, C. Yang, E.G. Ng, P. Maris, J.P. Vary, High Performance Computing and Simulation (HPCS), 2011 International Conference on, vol., no., pp. 176–185, 4–8 July 2011.
[261] Hasan Metin Aktulga, Chao Yang, Umit V. Catalyurek, Pieter Maris, James P. Vary, Esmond G. Ng, in Proc. of Euro-Par 2011 Workshops (1), Bordeaux, France, August 2011, pp. 305–314.
[262] A. Srinivasa, M. Sosonkina, P. Maris, J.P. Vary, Procedia Computer Science 9, May 2012, ICCS 2012, pp. 256–265.
[263] Hasan Metin Aktulga, Chao Yang, Esmond G. Ng, Pieter Maris, James P. Vary, Lecture Notes in Computer Science, vol. 7484, 2012, pp. 830–842 (Euro-par 2012).
[264] Zheng Zhou, Erik Saule, Hasan Metin Aktulga, Chao Yang, Esmond G. Ng, Pieter Maris, James P. Vary, Umit Catalyurek, Accepted for P2S2-2012 (ICPP), Pittsburgh, PA, September 10–13, 2012 and to appear in the proceedings.